

BACKSCATTERING OF E.M. WAVES FOR ROUGH SURFACE MODELS

by

PATRICK DONALD O'KELLY

B.A.Sc., The University of British Columbia, 1965

A THESIS SUBMITTED IN PARTIAL FULFILMENT OF

THE REQUIREMENTS FOR THE DEGREE OF

DOCTOR OF PHILOSOPHY

in the Department of Electrical Engineering

We accept this thesis as conforming to the
required standard

Research Supervisor.....

Members of the Committee.....

.....

.....

Head of Department.....

Members of the Department

of Electrical Engineering

THE UNIVERSITY OF BRITISH COLUMBIA

November, 1971

In presenting this thesis in partial fulfilment of the requirements for an advanced degree at the University of British Columbia, I agree that the Library shall make it freely available for reference and study. I further agree that permission for extensive copying of this thesis for scholarly purposes may be granted by the Head of my Department or by his representatives. It is understood that copying or publication of this thesis for financial gain shall not be allowed without my written permission.

Department of Electrical Engineering

The University of British Columbia
Vancouver 8, Canada

Date Feb. 4/72

to Kathleen

ABSTRACT

Backscattering from certain models of rough surfaces is studied by application of a Monte-Carlo technique and by experiments on a physical model. The models considered are lossless arrays of hemicylinders and of hemispheres on a lossless ground plane.

For the Monte-Carlo simulation, the incident radiation is considered to be a cylindrical or spherical wave with finite beamwidth. The shape of the beam is chosen to be the same as the far field radiation pattern of an open waveguide. Multiple scattering effects are investigated for a periodic array of hemicylinders and found to be significant for object diameters greater than one wavelength, and densities greater than 30%. It is assumed that these results are also approximately valid for random arrays. The single scatter approximation is used for all studies of the random case with these limitations in mind.

A special surface distribution function is developed and tested which includes the constraint of finite scatterer size in a physical surface model. It is used to generate random coordinates from which a set of physical surfaces are formed out of die-stamped aluminum. These surfaces are scanned with 35 GHz. radiation from a pyramidal horn. Samples of the backscattered field are converted to digital information and numerically analysed to determine the scattered field statistics. These statistics are compared to those obtained from the simulation. The means (coherent intensity) are found to agree to within 2.5% while the variance (incoherent intensity) obtained experimentally is higher by a factor of about 15. This discrepancy is attributed to significant phase measuring errors introduced by the present scanning system.

TABLE OF CONTENTS

	Page
LIST OF ILLUSTRATIONS	viii
LIST OF TABLES	x
LIST OF SYMBOLS	xi
ACKNOWLEDGEMENTS	xv
1. INTRODUCTION	1
1.1 Existing Methods of Solution	1
1.1.1 Continuous Surface Model	2
1.1.2 Discrete Scatterer Model	3
1.1.3 Experimental Studies	4
1.2 Aims of this Study	4
1.2.1 Surface Model	5
1.2.2 Incident Beam Model	5
1.2.3 Monte-Carlo Method	6
1.2.4 Experiment	7
1.3 Restrictions	8
2. THE SCATTERED FIELD FROM AN ARBITRARY CONFIGURATION OF DISCRETE SCATTERERS ON A PERFECTLY CONDUCTING PLANE	9
2.1 Introduction	10
2.2 Scattering from a Configuration of Hemicylinders	10
2.2.1 Cylindrical Incident Beam	10
2.2.2 Scattering Coefficients for Grating	14
2.2.3 Image Method for Transformation to Surface Problem	16
2.2.4 Backscattered Field	17
2.2.5 Normalization of Field Equations	18

	Page
2.3 Scattering from a Configuration of Hemispheres.....	20
2.3.1 Spherical Incident Beam	20
2.3.2 Single Scattered Field	24
2.3.3 Far-Zone Backscatter	25
2.3.4 Normalization of Field Equations.....	28
2.4 Antenna Model	30
2.5 Restriction to Narrow Beamwidth	34
2.5.1 Two Dimensional Case	34
2.5.2 Three Dimensional Case	37
2.6 Importance and Range of Parameters	41
3. PERIODIC ARRAYS OF HEMICYLINDERS	43
3.1 Solutions for Various Orders of Accuracy	43
3.1.1 Exact Solution	43
3.1.2 Nearest Neighbour Approximation	46
3.1.3 First Order Nearest Neighbour Approximation	46
3.1.4 Single Scatter Approximation	47
3.2 Numerical Calculations of the Scattered Field	47
3.2.1 Determination of Active Scattering Area	48
3.2.2 Effect of the Orders Of Scattering Approximations	48
3.3 Scattered Field using Single Scatter Approximation.....	52
4. RANDOM ARRAYS OF HEMICYLINDERS AND HEMISPHERES	54
4.1 Generation of Scatterer Coordinates	55
4.1.1 Uniform Distribution	55
4.1.2 Non-Uniform Distribution	55
4.2 Calculation of Field Statistics	59

	Page
4.3	Determination of Active Scattering Area..... 61
4.4	Comparison of Results..... 64
4.4.1	Coherent Field..... 65
4.4.2	Incoherent Intensity..... 68
4.5	Summary..... 71
5.	CONSTRUCTION OF A LABORATORY SURFACE AND THE MEASUREMENT OF ITS SCATTERED FIELD..... 72
5.1	Design of the Experimental System..... 72
5.1.1	Parameter Values..... 73
5.1.2	Method of Measurement..... 75
5.1.3	Construction of the Surface..... 78
5.2	Simulation Test of the Surface Distribution..... 79
5.2.1	Determination of Minimum Grid Subdivision..... 80
5.2.2	Effect of Minimum Separation..... 80
5.2.3	Probability Density of Coordinates..... 83
5.2.4	Distribution of the Number of Scatterers per Independent Sample..... 92
5.3	Initial Testing of the Experimental Surface..... 92
5.4	Experimental Results Compared with Simulation Results..... 94
5.4.1	Preliminary Processing of Experimental Data..... 94
5.4.2	Correlation Distance for the Scattered Field..... 98
5.4.3	Statistics of the Scattered Field..... 100
5.5	Summary..... 101
6.	CONCLUSIONS..... 102
6.1	Surface Model..... 102
6.2	Simulations..... 103
6.3	Experiment..... 104
6.4	Numerical Results..... 105
6.5	General Recommendations..... 106

	Page
APPENDIX A DETERMINATION OF UNKNOWN SCATTERING COEFFICIENTS	108
APPENDIX B RELATION BETWEEN REAL AND IMAGE FUNCTIONS	111
APPENDIX C FIRST ORDER NEAREST NEIGHBOUR APPROXIMATION	113
APPENDIX D SINGLE OBJECT SINGLE SCATTER STATISTICAL CALCULATIONS	115
APPENDIX E INTERGRATION OF SINGLE SCATTER COHERENT AND INCOHERENT INTENSITY FOR THE CONTINUOUS UNIFORM DISTRIBUTION	118
E.1 Two Dimensional Problem	118
E.1.1 Coherent Field	118
E.1.2 Incoherent Intensity	121
E.2 Three Dimensional Problem	126
E.2.1 Coherent Field.....	126
E.2.2 Incoherent Intensity	129
REFERENCES	130

LIST OF ILLUSTRATIONS

Figure	Page
2.1	Scattering Geometry for Two Dimensional Problems..... 11
2.2	Real and Image Fields Incident on a Cylinder..... 16
2.3	Image Source..... 19
2.4	Geometry of Three Dimensional Scattering Problem..... 20
2.5	Radiation Pattern for Horn Antenna and for Approximate Beam Functions..... 32
2.6	Effective Surface Width..... 34
3.1	Periodic Two Dimensional Surface..... 44
3.2	Magnitude and Phase of Scattered Field as a Function of the Ratio of Surface Width to Beamwidth..... 49
3.3	Error Introduced by the Single Scatter Approximation as a Function of Hemicylinder Density for Various Values of Hemicylinder Radius. 50
3.4	Error Introduced by the First Order Nearest Neighbour Approximation as a Function of Hemicylinder Density for Various Values of Hemicylinder Radius..... 51
4.1	Discrete Distribution of Scatterers..... 57
4.2	Modified Discrete Distribution of Scatterers..... 58
4.3	The Determination of Active Beamwidth - Coherent Field..... 62
4.4	The Determination of Active Beamwidth - Incoherent Field..... 63
4.5	A Comparison of Three Methods for Calculating the Single Scattered Coherent Field for an Array of Hemicylinders with $\rho = 2\%$ and $a = 0.2\lambda$ 66
4.6	A Comparison of Three Methods for Calculating the Single Scattered Coherent Field for an Array of Hemicylinders With $\rho = 2\%$ and $a = 0.05\lambda$ 67
4.7	A Comparison of Three Methods of Calculating the Single Scattered Incoherent Intensity for an Array of Hemicylinders..... 69
5.1	Experimental System..... 76
5.2	Reference Plate for Normalization..... 77
5.3	Forming a Hemispherical Scatterer in Aluminum Sheet..... 78

Figure	Page
5.4 Computer Generated Hemisphere Coordinates.....	79
5.5 Effect of Distribution Parameters.....	79
5.6 Scattered Field Statistics as a Function of N_s for Various Densities of Hemispheres.....	81
5.7 Scattered Field Statistics vs. Density of Hemispheres for Various Separations.....	82
5.8 Probability Density of Hemisphere Coordinates for an Object Density of 5% and 500 Sample Surfaces, $N_s = 1$	84
5.9 Probability Density of Hemisphere Coordinates for an Object Density of 5% and 500 Sample Surfaces, $N_s = 2$	85
5.10 Probability Density of Hemisphere Coordinates for an Object Density of 5% and 500 Sample Surfaces, $N_s = 3$	86
5.11 Probability Density of Hemisphere Coordinates for an Object Density of 10% and 500 Sample Surfaces, $N_s = 1$	87
5.12 Probability Density of Hemisphere Coordinates for an Object Density of 10% and 500 Sample Surfaces, $N_s = 2$	88
5.13 Probability Density of Hemisphere Coordinates for an Object Density of 10% and 500 Sample Surfaces, $N_s = 3$	89
5.14 Variance of Scatterer Coordinates as a Function of N_s	90
5.15 Probability Density of the Number of Spheres in the Illuminated Area for $N_s = 1, 2, 3$ and Densities of 5% and 10%.....	91
5.16 Results from Test Surface.....	93
5.17 Data from a Typical Sheet.....	96
5.18 Statistics of Simulated and Experimental Data.....	99

LIST OF TABLES

Table		Page
2.1	The Parameters of the Scattering Problem.....	42
5.1	Statistics of Simulation and Experimental Data.....	100

LIST OF SYMBOLS

$\langle E \rangle$	= ensemble average of function E
$\text{Re}(E)$	= real part of complex function E
$\text{Im}(E)$	= imaginary part of complex function E
$ E $	= magnitude of complex function E
$\text{Arg}(E)$	= phase of complex function E
E^*	= complex conjugate of E
A	= position of antenna
A_n, A'_n	= scattering coefficient for a single cylinder
a	= scatterer radius
a_n, a'_n	= scattering coefficient for a single sphere
B_{ns}	= multiple scattering coefficient of the s^{th} cylinder
B	= a real constant
b, b_θ, b_ϕ	= real constants
\bar{C}	= column vector of incident wave coefficients
C^2	= coherent intensity
C_a	= antenna beamwidth factor
C_s	= distance from antenna to s^{th} scatterer
$C_n(x)$	= any cylinder function of order n, real argument x
D	= width of antenna aperture
D_s	= amplitude factor of plane wave at s^{th} cylinder
d	= separation of periodic scatterers
d_{min}	= minimum separation of scatterers
E_{scat}	= total field scattered from an array of cylinders or spheres
E_{plane}	= total field scattered from a ground plane
E_{norm}	= field normalization factor

E_{obj}	= total field scattered from an array of hemicylinders
E_{TS}	= total scattered electric field
E_p	= electric field amplitude at some polarization angle
E_{ij}	= polarization components of the electric field
E_T	= Total electric field
E_i	= incident electric field
E_s	= field scattered from the s^{th} cylinder
E_o	= complex constant field amplitude factor
E	= normalized total scattered electric field
f_b, f_p, f_{MC}	= average scattering amplitudes
$f(\theta), f(\theta, \phi)$	= antenna beam functions
$f_{nm}^s, f_{nm}^{st}, h_{nm}$	= series expansion coefficients
$g(u), g(u, v)$	= antenna beam functions
$g_n(u)$	= antenna beam function with variable sidelobe level
H	= matrix of multiple scattering amplitudes
$H_n(x)$	= Hankel function of the first kind of order n , argument x
$h_n(x)$	= spherical Hankel function of the first kind
H_{mn}	= a linear combination of $H_{m-n}(x)$ and $H_{m+n}(x)$
$\bar{i}, \bar{j}, \bar{k}$	= cartesian unit vectors
$\langle I^2 \rangle$	= incoherent intensity
$J_n(x)$	= Bessel function of order n , argument x
$j_n(x)$	= spherical Bessel function of order n , argument x
K	= ratio of effective surface width to width of main antenna beam at the surface
K_r, K_s, K_o	= experimental system overall channel gains
k	= free space wave number
L	= a lower triangular matrix
L	= antenna to surface distance

N_0	= number of scatterers in the active scattering area
N_s	= number of subcells of the modified discrete uniform distribution
P	= point of observation
$P_n^m(x)$	= Legendre function of order n , argument x
P_n^m, Q_n^m	= functions of legendre functions
R, θ	= polar coordinates relative to centre of antenna
R_a, θ_a, ϕ_a	= spherical coordinates relative to centre of antenna
R_s, Φ_s	= polar coordinates of s^{th} scatterer
R_p, S_p, ϕ_p	= reference level, signal level, relative phase level
r_s, θ_s, ϕ_s	= coordinates relative to the location of the s^{th} scatterer
s, t	= indices specifying the s^{th} and t^{th} scatterer
U	= a wave function
U	= an upper triangular matrix
\bar{W}	= column vector of scattering coefficients
W	= active surface width
W_0	= width of antenna main beam at surface
X, Y, Z	= rectangular coordinates relative to the centre of the active scattering area
X_s, Y_s	= rectangular coordinates of the s^{th} scatterer
X_{ns}, Y_{ns}	= scattering coefficients for hemicylinders
x_s, y_s, z_s	= rectangular coordinates relative to the centre of the s^{th} scatterer
x_a, y_a, z_a	= rectangular coordinates relative to the centre of the antenna
α	= angle of incidence
β_s	= angle to antenna from the s^{th} scatterer
δ	= polarization angle
ϵ_m	= Neumann factor

$\bar{\epsilon}_r, \bar{\epsilon}_\theta, \bar{\epsilon}_\phi$	= spherical unit vectors
λ	= free space wavelength
ρ	= area density of objects
ρ	= correlation coefficient
ρ_d	= complex correlation coefficient
ρ_s	= normalized radial coordinate of the s^{th} scatterer
ρ_{x_s}, ρ_{y_s}	= normalized cartesian coordinates of the s^{th} scatterer
σ_x^2	= variance of the random variable x
σ_x	= standard deviation of the random variable x
σ_{xy}	= covariance of the random variables x and y

ACKNOWLEDGEMENTS

I wish to thank my research supervisor Dr. M. Kharadly for his expert guidance throughout this project.

Acknowledgement is given to the National Research Council of Canada for postgraduate scholarships from 1965 to 1969, and for support under grant A-3344.

I wish also to thank Mr. D. Daines of the machine shop staff for his invaluable assistance with the construction of the experimental surface model.

Finally, I thank Miss J. Murie for typing the manuscript, and Mr. K. McRitchie and Dr. D. Corr for their proficient proofreading.

1. INTRODUCTION

The analysis of electromagnetic or acoustic wave scattering by rough surfaces requires the solution of the wave equation $\nabla^2 U = -\frac{\partial^2 u}{\partial t^2}$ subject to the appropriate boundary conditions on the "rough" boundary. By "rough", one should understand that the boundary is solely described by its statistical properties. Examples of this type of problem include radar returns from terrain or sea surface, radar exploration of the surfaces of the moon and planets, sonar returns from the ocean floor, optical reflections used industrially to determine the quality of machined surfaces, and many others.

1.1 Existing Methods of Solution

Basically, one must first solve the wave equation for a general boundary and then integrate the field over all possible configurations of this boundary to obtain the required statistics of the scattered field. Of course, a solution this general may not be obtainable by the methods presently available. Therefore, sufficient restrictions must be placed upon the definition of the problem to allow one to obtain useful results. The following restrictions have been imposed, not necessarily all at once, by previous investigators:

1. Harmonic time dependence.
2. Infinite plane wave incidence.
3. Boundary surface perfectly conducting or pure dielectric interface.
4. Only scalar solution obtained.
5. One dimensional roughness only.
6. Surface is locally plane and/or

7. Scattering elements are much smaller than the wavelength.
8. Active scattering areas are either very dense or very sparse.
9. A particular restricted model is chosen for the surface.

All treatments of the problem have been subjected to limitation 9.

Generally speaking, there are two main methods for representing the scattering boundary which divides the methods for solving the problem into two distinct classes. The first method is to define the boundary as some continuous random variable $z = f(x,y)$ which is ultimately defined by its statistical moments (mean, variance, etc.) and subject to appropriate restrictions. The second method is to represent the surface by a collection of discrete scatterers which are, in general, random in size, shape, and position. However, the only random variable considered so far has been the position of each object.

1.1.1 Continuous Surface Model

Consider first the continuous surface model. This was first investigated by Lord Rayleigh¹ in 1896. He assumed a sinusoidal perfectly conducting surface with normal incidence. His approach required a Fourier series expansion of the incident wave and the surface profile. S.O. Rice² generalized the Rayleigh approach to a slightly rough surface described by its small deviation from a mean plane. Rice's reflection coefficient was verified experimentally with reflections from blacktop roadway⁵. W.C. Hoffman³ used a similar expansion of the surface, but applied it to the Stratton - Chu integral⁴ for the scattered field. Hoffman's results were no more general than Rice's, but his derivation had the merit of being mathematically rigorous. T.B.A. Senior⁶ assumed that the roughness was a perturbation of a mean plane, and by using a Taylor series expansion of the

field at the boundary he developed a surface impedance tensor for the rough surface. Again, this method is restricted to slightly rough surfaces. Beckmann⁷ used a physical optics method to obtain the required reflection coefficient. More recently, Middleton⁸ attacked the problem from the point of view of pure communications theory with little consideration given to the electromagnetic aspect of the problem. Also, Bass et al⁹ applied a perturbation method to sea reflections. It should be noted that all the above methods require surfaces that are only slightly rough. That is, the surfaces have either small deviations in height from a mean plane, or they have a long correlation distance.

1.1.2 Discrete Scatterer Model

The main investigations have been carried out by Ament¹⁰, Biot¹¹, Spetner¹², and Twersky^{13,14,15,16}. Twersky^{17,18} has also considered the statistical problems which are connected with this method when higher order statistical moments of the field are to be considered. Most investigators have only considered the problem of the mean scattered field, or at best, the mean and variance.

Ament modelled his surface as a collection of randomly spaced half-planes. Biot considered a uniform distribution of hemispheres on a perfectly conducting ground plane, but these objects were required to be so small that very little scattering could take place. Spetner assumed a distribution of point scatterers, which yielded relatively simple results. Twersky has contributed the largest amount of information towards the solution of these problems. He considered either hemispheres or hemicylinders on a perfectly conducting ground plane. The main advantage of the Twersky approach is that use is made of our extensive knowledge of the scattering properties of a member of the distribution alone. Here again, the random

variable has been limited to be the position of the objects. Under suitable approximations the results are simple, at least for the mean of the scattered field.

1.1.3 Experimental Studies

Some workers have investigated this problem experimentally. In these studies, restriction #2 is removed by the use of actual receiving and transmitting antennas with their associated finite beamwidth and non-plane wavefront. The remaining restrictions, except for 8, may also be removed. The choice of the surface model divides the experimental studies into two sections corresponding to the choice of specific natural surfaces or of laboratory constructed models. Natural surface data has been analysed by such investigators as W.H. Peake⁵ who considered reflections from blacktop and lawn grass, and M. Katzin¹⁹ who considered radar sea clutter. For the laboratory studies, R.H. Clarke and G.O. Hendry²⁰ worked with a water surface agitated by a controlled air flow; Hiatt, Senior, and Weston²¹ considered a surface produced by rough casting of metal; B.E. Parkins²² constructed two surfaces, one by denting sheet metal with a hammer, and the other by flowing grout over sand. In all the above experiments, a method had to be devised for measuring the statistics of the models as the statistics could only be roughly controlled.

1.2 Aims of this Study

Basically, the aims of this investigation are the following.

1. To choose a feasible and controllable surface model.
2. To include the effect of the finite beamwidth and non-plane character of incident radiation from an antenna.
3. To develop a Monte-Carlo technique²³ for calculating the scattered field statistics; the main problem here is to

devise a suitable numerical method for determining the distribution of scatterers.

4. To carry out a series of experiments upon an artificial surface for which the properties can be accurately controlled.

1.2.1 Surface Model

For this work the Twersky model of a rough surface was chosen. The reason for this is threefold. First, it was felt that a more exact solution should be obtainable for higher degrees of roughness because the scattering characteristics of the individual objects were known exactly. Second, a Monte-Carlo method was proposed for the calculation of the scattered field statistics which requires the generation of thousands of different surface profiles. Third, experimental models could be more exactly constructed, and would have desired repeatability.

The general analysis of the particular surfaces composed of arrays of circular hemicylinders or hemispheres on a lossless ground plane is considered in Chapter 2. It includes the effect of finite non-plane wave incidence. Multiple scattering is considered in Chapter 3.

1.2.2 Incident Beam Model

There are two reasons for the inclusion of finite beamwidth non-plane incident radiation. The main one is to determine the behaviour of the field in a more realistic situation. However, it should also be mentioned that the infinite beamwidth case cannot be treated by the Monte-Carlo approach because this would require the storage of an infinite array of numbers or an infinite amount of calculation time.

The specific model proposed is that of the far-field radiation from an aperture with an appropriate illumination function⁴. This model was chosen for the following reasons:

1. It can be made to resemble very closely the radiation pattern of a laboratory antenna.
2. It is simple enough mathematically to be easily included in the field equations.
3. The beamwidth, sidelobe level, and sphericity of the wavefront can be easily controlled.

This problem of the incident beam is discussed in detail at the beginning of Chapter 2.

1.2.3 Monte-Carlo Method

The Monte-Carlo method is the most direct method for calculating the scattered field statistics and it has known accuracy. Thus it is suitable for obtaining numerical results and for evaluating theoretical approaches. Analytic solutions are usually obtained by the following sequence of operations:

1. Calculate the scattered field due to one object.
2. Use the above to calculate the total field scattered by an array of the above objects.
3. Integrate the field over all possible configurations using some particular distribution function for the locations of the objects to obtain all the desired statistical moments.

The drawback of the analytic method is the inherent connection between the calculation of the field, and the calculation of its statistics.

On the other hand, the Monte-Carlo technique proceeds as follows:

1. As above.
2. As above.
3. Determine a single configuration according to some numerical random or pseudo-random process.
4. Calculate the field due to this configuration by 2.
5. Keep a running mean, variance, etc.

6. Repeat 3,4 and 5 until a sufficient number of surface configurations have been used to approximate the desired statistical moments.

It thus eliminates the drawback in the analytic method as it will work on any sequence of random functions, provided only that the elements of the sequence themselves may be numerically calculated. The implementation of the Monte-Carlo method is therefore divided into three distinct parts:

1. Obtaining an analytic expression for the scattered field from a fixed configuration.
2. Numerical determination of the coordinates of each configuration.
3. Numerical calculation of the field using 2 and the calculation of the statistical moments.

The application of the Monte-Carlo method to the surface models studied in Chapters 2 and 3 is given in Chapter 4, where the problem of suitable methods of determining the distribution of scatterer positions is also discussed.

1.2.4 Experiment

The main purposes for performing an experimental study were to compare actual results with theory and to give another method which could be used where the approximate theory became incorrect. These aims restricted the choice of the experimental surface to be of the controlled laboratory type.

The experimental surface used was, in fact, a duplication of the one used for the theoretical simulation of the problem: perfectly conducting metal hemispheres on a nearly flat metal ground plane. The locations of the hemispheres could be determined by the same method as that used in the simulation. Thus, unlike previous experiments the distribution and density of the experimental surface could be strictly controlled. In prior

experiments these factors had to be estimated after the surface was constructed. The implementation of the experiment is described in Chapter 5.

1.3 Restrictions

In summary the approach taken in this thesis required that the previous list of restrictions on the problem be modified to the following:

1. Harmonic time dependence.
2. Finite beam incidence with non-plane wavefront.
3. Boundary surface same.
4. Vector solution.
5. Surface two or three dimensional.
6. Surface need not be locally plane.
7. Object dimensions up to a wavelength (simulation) or greater (experiments).
8. Object density from sparse to about 50%.
9. Surface model circular hemicylinders or hemispheres on a perfectly conducting ground plane.

2. THE SCATTERED FIELD FROM AN ARBITRARY CONFIGURATION OF DISCRETE SCATTERERS ON A PERFECTLY CONDUCTING PLANE

2.1 Introduction

In this chapter the scattering of a finite non-plane electromagnetic beam by a single configuration of objects is analysed. A simple far-zone radiation pattern is assumed for the incident wave used in the derivation of the field scattered from an array of perfectly conducting hemicylinders on a perfectly conducting ground plane in section 2.2, and from an array of perfectly conducting hemispheres on a perfectly conducting ground plane in section 2.3.

The array of hemicylinders is formulated as a purely two dimensional problem by considering infinitely long cylinders and the plane of incidence perpendicular to the axis of the cylinders as shown in figure 2.1. Hence the results may be derived from the scalar wave equation²⁴. Of course, this model of a rough surface is a very restricted one but the results could be applied to any physical problem which is essentially (or locally) two dimensional such as radar returns from water waves.

The derivation essentially follows Twersky¹³. First, a grating of objects is analysed by the separation of variables method, and then the Rayleigh Image technique¹³ is applied to obtain the solution to the surface problem. Because of the relative simplicity of the calculations and in anticipation of the study in the next chapter of the periodic array, the calculations are given in detail for the two dimensional case. For convenience backscattering only is considered. For the present purpose it is sufficient, to consider only the single scatter approximation for normal incidence in the three dimensional case. The reasons for the

normal incidence restriction is given in section 2.3.4. Beckmann⁷ states that the geometry of the problem is perhaps the most dominant factor in rough surface scatter. Under this assumption then even the approximate solutions considered here should prove useful. The experimental results are given in Chapter 5

The development generally follows the treatment of hemicylinders, but further complications are introduced by the vector nature of the problem. The field scattered from a single sphere cannot in general be derived from the two scalar equations. These vector solutions are discussed fully by Stratton²⁵ and by Morse and Feshbach²⁶, but the form used here is essentially that given by Twersky¹⁴.

In section 2.4 a specific model is proposed for the antenna beam used in all subsequent studies. The model is chosen to be representative of a laboratory horn antenna.

Finally, in section 2.6 the relevant parameters of the problem are discussed and their role in the problem and range of values are decided upon.

2.2 Scattering from a Configuration of Hemicylinders

2.2.1 Cylindrical Incident Beam

Assume harmonic time dependence, $e^{-i\omega t}$. Hence the reduced scalar wave equation $(\nabla^2 + k^2)E_T = 0$ must be solved with the correct boundary conditions on the surfaces of the cylinders. Although the solution may be obtained as easily for dielectric cylinders, only the perfectly conducting case shall be considered in the following problems for computational simplicity. Let

$$E_T = E_i + \sum_{s=1}^{N_0} E_s \quad (2.1)$$

where

E_T is the total electric field

E_i is the incident beam, at angle α

E_s is the complete multiple scattered field from the s^{th} object

N_0 is the total number of objects

At this point, consider the form of E_i . The usual treatment would be to put $E_i = e^{i\vec{k}\cdot\vec{r}} = e^{ikr \cos(\theta - \alpha + \frac{\pi}{2})}$ and refer this to the coordinate of the s^{th} object. That is, one would assume plane wave incidence. However, E_i may be considered to be the far-field radiation from some directional but two dimensional source such as a long narrow slot. The incident wave must be considered in terms of a series of elementary cylindrical waves in order to match boundary conditions. Now, let $E_i = F(R, \theta)$, where R and θ are referred to the centre of the radiator. In particular, since only the far-zone field of the radiator need be considered, let

$$E_i = E_0 \frac{e^{ikr}}{\sqrt{kr}} f(\theta) \quad (2.2)$$

which is the form of a cylindrical wave multiplied by the space factor, $f(\theta)$.

The scattered field is derived using the geometry given in figure

2.1.

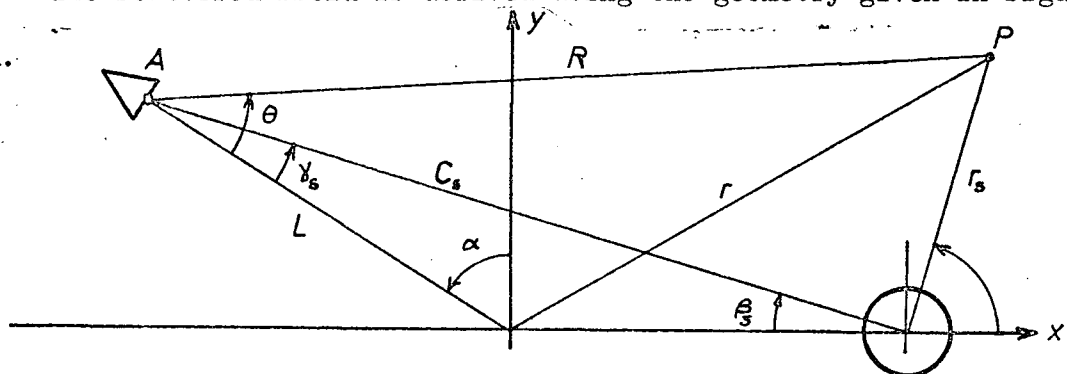


Figure 2.1 Scattering Geometry for Two Dimensional Problem

In the above diagram,

A = position of antenna

P = point of observation

$(X_s, 0)$ = position of the s^{th} cylinder

α = angle of incidence

L = distance from antenna to surface

Assume that L is large, as the far-zone field of the antenna is to be considered. Also, assume that r_s is small, which is possible because r_s will be finally placed at the surface of the s^{th} object to satisfy boundary conditions. Thus, using figure 2.1,

$$R^2 = (L \sin \alpha + X_s + r_s \cos \theta_s)^2 + (L \cos \alpha - r_s \sin \alpha)^2 \quad (2.3)$$

let

$$C_s^2 = (L \cos \alpha)^2 + (X_s + L \sin \alpha)^2 \quad (2.4)$$

$$\tan \beta_s = \frac{L \cos \alpha}{X_s + L \sin \alpha} \quad (2.5)$$

and, since $r_s \ll L$,

$$R^2 \approx C_s^2 + 2r_s C_s \cos(\theta_s + \beta_s) \quad (2.6)$$

As C_s is actually the distance from the centre of the antenna to the s^{th} object (see figure 2.1), and r_s will be limited to the vicinity of the surface of the s^{th} object, it is also true that $r_s \ll C_s$ for any s , provided that the antenna is sufficiently far from the surface and that the illuminated area of the surface is sufficiently limited in extent. Of course, the extent of the surface considered will be limited by the beam

width of the antenna. Therefore,

$$R \approx C_s + r_s \cos(\theta_s + \beta_s) \quad (2.7)$$

A similar approximation is applied to the angular antenna coordinate. From figure 2.1

$$\theta = \frac{\pi}{2} - \alpha - \tan^{-1} \left\{ \frac{L \cos \alpha - r_s \sin \theta_s}{L \sin \alpha + X_s + r_s \cos \theta_s} \right\} \quad (2.8)$$

Now, make the assumption that the amplitude, $f(\theta)$, is constant and equal to the value it attains at the centre across the entire surface of the scattering object. This approximation is reasonable provided that

$$r_s \ll L \cos \alpha$$

$$r_s \ll X_s + L \sin \alpha$$

(2.9)

which implies that the objects are small compared to the distance from the antenna to the surface. Hence, equation (2.8) becomes

$$\theta \approx \frac{\pi}{2} - \alpha - \tan^{-1} \frac{L \cos \alpha}{X_s + L \sin \alpha} \quad (2.10)$$

Therefore the incident wave arriving at the s^{th} object can be assumed to be approximately plane in the vicinity of that object, that is,

$$E_i \approx E_0 \frac{e^{ikC_s}}{\sqrt{kC_s}} e^{ikr_s \cos(\theta_s + \beta_s)} f\left(\frac{\pi}{2} - \alpha - \beta_s\right) \quad (2.11)$$

For simplicity, let

$$D_s = \frac{e^{ikC_s}}{\sqrt{kC_s}} f\left(\frac{\pi}{2} - \alpha - \beta_s\right) \quad (2.12)$$

so that

$$E_i = E_0 D_s e^{ikr_s \cos(\theta_s + \beta_s)} \quad (2.13)$$

Also, note that for convenience $f(0) = 1$ and that E_0 is merely a complex constant amplitude factor which may later be adjusted to give a normalized solution.

2.2.2 Scattering Coefficients for Grating

The plane wave (2.13) may now be expanded in a series of cylindrical waves²⁴ referred to the axis of the s^{th} cylinder.

$$E_i = E_0 D_s \sum_{n=-\infty}^{\infty} J_n(kr_s) (i)^n e^{in(\theta_s + \beta_s)} \quad (2.14)$$

The wave scattered from the s^{th} object may be expanded in a similar series of outgoing cylindrical waves.

$$E_s = \sum_{n=-\infty}^{\infty} B_{ns} H_n(kr_s) e^{in\theta_s} \quad (2.15)$$

where $H_n(Z)$ shall always refer to $H_n^{(1)}(Z)$, the Hankel function of the first kind. Thus, from (2.1), the total field is given by

$$E_T = E_i + \sum_{s=1}^{N_0} \sum_{n=-\infty}^{\infty} B_{ns} H_n(kr_s) e^{in\theta_s} \quad (2.16)$$

for a particular set of positions X_1, X_2, \dots, X_{N_0} , and the unknowns B_{ns} are determined from the boundary conditions. The calculation is outlined in Appendix A and the results are

$$B_{ns} = A_n^{\parallel, \perp} \left[E_0 D_s (i)^n e^{in\beta_s} + \sum_{\substack{t=1 \\ t \neq s}}^{N_0} \sum_{m=-\infty}^{\infty} B_{mt} H_{n-m}(k|X_t - X_s|) r_{nm}^{st} \right] \quad (2.17)$$

where

$$A_n^{\parallel} = - \frac{J_n'(ka)}{H_n'(ka)} \quad (2.18)$$

$$A_n^{\perp} = - \frac{J_n(ka)}{H_n(ka)} \quad (2.19)$$

$$f_{nm}^{st} = \begin{cases} 1, & t > s \\ (-1)^{m+n}, & t < s \end{cases} \quad (2.20)$$

At this point, one is faced with the formidable task of solving the infinite set of simultaneous linear algebraic equations, (2.17), for the infinite number of unknowns, B_{ns} . First, reduce (2.17) to a finite number of equations in a finite number of unknowns by assuming that the A_n become negligible after some $n = N$, say. This is reasonable especially if ka is small (i.e. small scatterers). Second, introduce the change of variables,

$$X_{ns} = \frac{(i)^n}{2E_0} (B_{-ns} + (-1)^n B_{ns}) \quad n = 1, 2, \dots \quad (2.21)$$

$$X_{os} = \frac{B_{os}}{2E_0}$$

$$Y_{ns} = \frac{(i)^n}{2E_0} (B_{-ns} - (-1)^n B_{ns}) \quad (2.22)$$

Substitution of (2.21) and (2.22) into (2.17) yields

$$X_{ns} = A_n \left[D_s \cos n\beta_s + \sum_{t=1, t \neq s}^{N_0} \sum_{m=0}^N (i)^{n-m} X_{mt} H_{mn}^+(k|X_t - X_s|) f_{nm}^{st} \right] \quad (2.23)$$

$$Y_{ns} = A_n \left[-iD_s \sin n\beta_s + \sum_{t=1, t \neq s}^{N_0} \sum_{m=0}^N (i)^{n-m} Y_{mt} H_{mn}^-(k|X_t - X_s|) f_{nm}^{st} \right] \quad (2.24)$$

where

$$H_{mn}^{\pm}(x) = H_{m-n}(x) \pm (-1)^n H_{m+n}(x) \quad (2.25)$$

$$H_{on}(x) = (-1)^n H_n(x) \quad (2.26)$$

Use was made of the fact that $C_{-n}^{\pm}(z) = (-1)^n C_n^{\pm}(z)$ for any cylinder function C_n^{\pm} . Note that the systems of equations to be solved, (2.23) and (2.24), are each half the size of the original system (2.17) but the operation must be performed twice. This is, of course, a great saving of work if an exact numerical solution is required. Before attempting this, however, it is advantageous to apply the Rayleigh image technique^{1,7,13} to obtain the proper form for the solution to the surface problem.

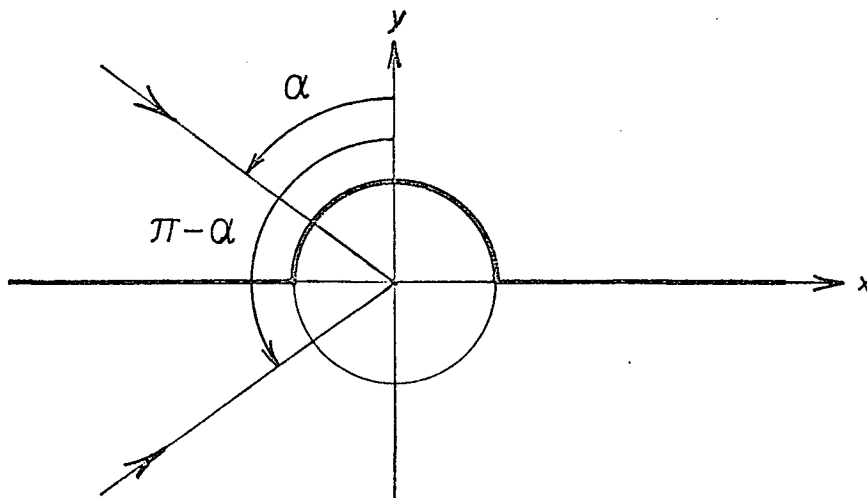


Figure 2.2 Real and Image Fields Incident on a Cylinder

2.2.3 Image Method for Transformation to Surface Problem

The image method is as follows. For a wave incident at angle α as shown in figure 2.2, the scattered field from the half cylinder will be composed of the field produced by a field incident at angle α and its image at angle $\pi - \alpha$ incident upon a whole cylinder. The solution will be correct in the region $Y > 0$ only. The validity of this may be readily checked by testing to see if the boundary conditions are satisfied. If E_T is now defined to be the total field for the surface problem,

$$E_T^{H,L}(\alpha) = E_i(\alpha) \pm E_i(\pi - \alpha) + \left[E_{\text{scat}}(\alpha) \pm E_{\text{scat}}(\pi - \alpha) \right] \quad (2.27)$$

$$= E_{\text{inc}} + E_{\text{plane}} + E_{\text{obj}} \quad (2.28)$$

There is considerable simplification of the problem after application of the above equations due to the symmetry of the real and image functions. Now, the E_{obj} in equation (2.28) is composed of the fields scattered by the individual objects:

$$E_{obj}^{||,\perp} = E_{scat}(\alpha) \pm E_{scat}(\pi - \alpha) \quad (2.29)$$

$$= \sum_s \left[E_s(\alpha) \pm E_s(\pi - \alpha) \right] \quad (2.30)$$

$$= \sum_s E_s^{||,\perp} \quad (2.31)$$

It is interesting to note that only one set of the coefficients X_{ns} or Y_{ns} need to be calculated for each polarization for the surface problem (see Appendix B). The resulting fields scattered by the s^{th} cylinder are:

$$E_s^{||} = 4E_o \sum_{n=0}^N (i)^n X_{ns} \cos n\theta_s H_n(kr_s) \quad (2.32)$$

$$E_s^{\perp} = -4iE_o \sum_{n=1}^N (i)^n Y_{ns} \sin n\theta_s H_n(kr_s) \quad (2.33)$$

2.2.4 Backscattered Field

From this point onward, only the scattered field in the backscatter direction will be considered. The analysis for other directions is no different in principle. Backscatter is a reasonable choice as it represents the monostatic radar problem. From a consideration of the geometry of the problem (see figure 2.1), i. e. putting point P at point A

$$\begin{aligned} r_s &= C_s \\ \theta_s &= \pi - \beta_s \end{aligned} \quad (2.34)$$

(2.34) holds also for forward scatter if $C_s(\alpha)$ and $\beta_s(\alpha)$ are replaced with $C_s(-\alpha)$ and $\beta_s(-\alpha)$.

Since C_s is assumed to be large, $H_n(kC_s)$ may be approximated by the first term of its large argument asymptotic expansion²⁷

$$H_n(kC_s) \sim (-i)^n \frac{(1-i)e^{ikC_s}}{\sqrt{\pi} \sqrt{kC_s}} \quad (2.35)$$

(2.32) and (2.33) when combined with (2.34) and (2.35) give the following approximate expression for the far-zone backscattered field from the array of hemicylinders:

$$E_{\text{obj}}^{\parallel} = 4 \frac{(1-i)}{\sqrt{\pi}} E_0 \sum_{s=1}^{N_0} \frac{e^{ikC_s}}{\sqrt{kC_s}} \sum_{n=0}^N (-1)^n X_{ns} \cos n\beta_s \quad (2.36)$$

$$E_{\text{obj}}^{\perp} = 4i \frac{(1-i)}{\sqrt{\pi}} E_0 \sum_{s=1}^{N_0} \frac{e^{ikC_s}}{\sqrt{kC_s}} \sum_{n=1}^N (-1)^n Y_{ns} \sin n\beta_s \quad (2.37)$$

2.2.5 Normalization of Field Equations

Finally, the constant E_0 must be selected so as to yield a normalized reflected field. This normalization is such that the total reflected field is unity when the the surface is flat. From equation (2.28)

$$E_T = E_{\text{inc}} + E_{\text{plane}} + E_{\text{obj}} \quad (2.38)$$

$$= E_{\text{inc}} + E_{\text{TS}} \quad (2.39)$$

where E_{inc} is the incident field, E_{plane} is the field reflected by the plane and E_{TS} is the total scattered field. The required normalized field is then

$$E = \frac{E_{\text{TS}}}{E_{\text{norm}}} = 1 + \frac{E_{\text{obj}}}{E_{\text{plane}}} \quad (2.40)$$

Now, E_{plane} is simply the image of the incident wave in the plane (see figure 2.3).

Therefore, from equation (2.2), the corresponding image source becomes

$$E_{\text{plane}}^{\parallel, \perp} = \pm E_0 \frac{e^{ikR}}{\sqrt{kR}} f(\theta) \quad (2.41)$$

where R and θ are determined from the configuration shown in figure 2.3.

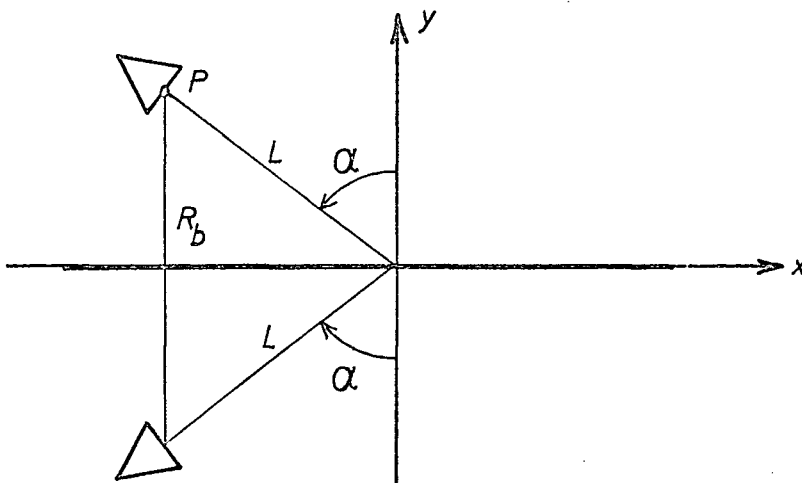


Figure 2.3 Image Source

For backscatter,

$$E_{\text{plane}}^{\parallel, \perp} = \pm E_0 \frac{e^{i2kL \cos \alpha}}{\sqrt{2kL \cos \alpha}} f(\alpha) \quad (2.42)$$

while for scattering in the forward direction

$$E_{\text{plane}}^{\parallel, \perp} = \pm E_0 \frac{e^{i2kL}}{\sqrt{2kL}} \quad (2.43)$$

Equations (2.36), (2.37), (2.40) and (2.42) may now be combined to yield the final form of the normalized backscattered field.

$$E^{\parallel} = 1 + 4 \frac{(1-i) \sqrt{2kL \cos \alpha}}{\sqrt{\pi} f(\alpha)} \sum_{s=1}^{N_0} \frac{e^{ik(C_s - 2L \cos \alpha)}}{\sqrt{C_s}} \sum_{n=0}^N (-1)^n X_{ns} \cos n\beta_s \quad (2.44)$$

$$E^{\perp} = 1 + 4 \frac{(1-i) \sqrt{2kL \cos \alpha}}{\sqrt{\pi} f(\alpha)} \sum_{s=1}^{N_0} \frac{e^{ik(C_s - 2L \cos \alpha)}}{\sqrt{C_s}} \sum_{n=1}^N (-1)^n Y_{ns} \sin n\beta_s \quad (2.45)$$

$$\begin{aligned}
E_i &= E_o \frac{e^{ikR_a}}{kR_a} f(\theta_a, \phi_a) \left[\sin(\phi_a + \delta) \bar{\epsilon}_\theta + \cos(\phi_a + \delta) \bar{\epsilon}_\phi \right] \\
&= E_o \frac{e^{ikR_a}}{kR_a} f(\theta_a, \phi_a) \bar{e}_p
\end{aligned} \tag{2.46}$$

where δ is the polarization angle:

$$\begin{aligned}
\delta &= 0 \text{ for } \parallel \text{ polarization} \\
\delta &= \frac{\pi}{2} \text{ for } \perp \text{ polarization}
\end{aligned} \tag{2.47}$$

and $\bar{\epsilon}_\theta, \bar{\epsilon}_\phi$ are unit vectors in the antenna coordinate system.

Now, by standard vector analysis,

$$\begin{aligned}
\bar{\epsilon}_\theta &= \cos \theta_a \cos \phi_a \bar{i}_a + \cos \theta_a \sin \phi_a \bar{j}_a - \sin \theta_a \bar{k}_a \\
\bar{\epsilon}_\phi &= -\sin \phi_a \bar{i}_a + \cos \phi_a \bar{j}_a
\end{aligned} \tag{2.48}$$

is the relation between the spherical and rectangular unit vectors.

Therefore, at the antenna,

$$\begin{aligned}
\bar{E}_p &= \left(\sin(\phi_a + \delta) \cos \theta_a \cos \phi_a - \cos(\phi_a + \delta) \sin \phi_a \right) \bar{i}_a \\
&+ \left(\sin(\phi_a + \delta) \cos \theta_a \sin \phi_a + \cos(\phi_a + \delta) \cos \phi_a \right) \bar{j}_a \\
&- \sin(\phi_a + \delta) \sin \theta_a \bar{k}_a
\end{aligned} \tag{2.49}$$

Refer the incident field to the x_s, y_s, z_s axes at the s^{th} object instead of to the antenna coordinate axes by the two translations along L and R_s .

$$\begin{aligned}
x_a &= -(x_s + X_s) \\
y_a &= y_s + Y_s \\
z_a &= L - z_s
\end{aligned} \tag{2.50}$$

and the unit vectors become

$$\begin{aligned}\overline{i}_a &= -\overline{i}_s \\ \overline{j}_a &= \overline{j}_s \\ \overline{k}_a &= -\overline{k}_s\end{aligned}\tag{2.51}$$

consequently,

$$R_a^2 = r_s^2 + R_s^2 + L^2 + 2(x_s X_s + y_s Y_s - z_s L)\tag{2.52}$$

where,

$$\begin{aligned}X_s &= R_s \cos \Phi_s \\ Y_s &= R_s \sin \Phi_s\end{aligned}\tag{2.53}$$

are the coordinates of the s^{th} scatterer.

To further simplify the problem, rotate the x_s, y_s, z_s coordinate axes through the angle Φ_s about the z_s axis. That is,

$$\begin{aligned}x_s &= x'_s \cos \Phi_s - y'_s \sin \Phi_s \\ y_s &= x'_s \sin \Phi_s + y'_s \cos \Phi_s \\ z_s &= z'_s\end{aligned}\tag{2.54}$$

Equation (2.52) becomes, upon the substitution of equation (2.54),

$$R_a^2 = r_s'^2 + C_s^2 + 2(R_s x_s - L z_s)\tag{2.55}$$

where

$$C_s^2 = R_s^2 + L^2\tag{2.56}$$

From figure 2.46

$$\begin{aligned}\sin \theta_c &= R_s / C_s \\ \cos \theta_c &= L / C_s\end{aligned}\tag{2.57}$$

Hence,

$$R_a^2 = r_s'^2 + C_s^2 + 2C_s(x_s' \sin \theta_c - z_s' \cos \theta_c) \quad (2.58)$$

And, since $r_s \ll C_s$ in the vicinity of the s^{th} object,

$$R_a \approx C_s + x_s' \sin \theta_c - z_s' \cos \theta_c \quad (2.59)$$

It is reasonable to assume, as in the two dimensional case, that the amplitude functions f and \bar{e}_p may be considered to be constant across the surface of the s^{th} scatterer. This assumption will be valid for small objects. Therefore, from figure 2.4,

$$\begin{aligned} \theta_a &\approx \theta_c \\ \phi_a &\approx \pi - \Phi_s \end{aligned} \quad (2.60)$$

and from equations (2.51) and (2.54),

$$\begin{aligned} \bar{i}_a &= -\cos \Phi_s \bar{i}_s' + \sin \Phi_s \bar{j}_s' \\ \bar{j}_a &= \sin \Phi_s \bar{i}_s' + \cos \Phi_s \bar{j}_s' \\ \bar{k}_a &= -\bar{k}_s' \end{aligned} \quad (2.61)$$

Thus, by equations (2.60) and (2.61), equation (2.49) becomes:

$$\bar{e}_p \approx \sin(\Phi_s - \delta) (\cos \theta_c \bar{i}_s' + \sin \theta_c \bar{k}_s') + \cos(\Phi_s - \delta) \bar{j}_s' \quad (2.62)$$

Finally, then, the incident wave may be approximately represented as

$$\begin{aligned} E_i &\approx E_0 \frac{e^{1kC_s}}{kC_s} e^{ik(x_s' \sin \theta_c - z_s' \cos \theta_c)} f(\theta_c, \pi - \Phi_s) \\ &\quad \left[\sin(\Phi_s - \delta) (\cos \theta_c \bar{i}_s' + \sin \theta_c \bar{k}_s') + \cos(\Phi_s - \delta) \bar{j}_s' \right] \end{aligned} \quad (2.63)$$

in the x_s', y_s', z_s' coordinate system. This corresponds to an incident wave, which is plane across the s^{th} scatterer, with angle of incidence and angle

of polarization

$$\text{and} \quad \begin{aligned} \alpha &= -\theta_c \\ \delta' &= \delta - \Phi_s \end{aligned} \quad (2.64)$$

respectively.

2.3.2 Single Scattered Field

As the derivation of the two dimensional scattered field has been considered in detail, the following expression¹⁴ for the three dimensional field scattered from a single hemisphere on a ground plane with the incident plane wave of equation (2.63) is presented without further comment:

$$\begin{aligned} \overline{E}_{s'} &= \frac{-2iE_0}{kr_s} \sum_{n=1}^{\infty} \frac{(2n+1)}{(i)^n} a'_n h_n(kr_s) \sum_{\substack{m=0 \\ m+n \text{ odd}}}^n \left[P_{n\alpha}^m \cos m\phi_s \sin\delta' - \frac{m P_{n\alpha}^m \sin m\phi_s \cos\delta'}{\sin\alpha} \right] \overline{E}_{r_s} \\ &- 2iE_0' \sum_{n=1}^{\infty} \frac{(2n+1)}{(i)^n n(n+1)} \left\{ a'_n \left[\frac{kr_s h_n(kr_s)}{kr_s'} \right]' \sum_{\substack{m=0 \\ m+n \text{ odd}}}^n \left[P_{n\alpha\theta}^m \cos m\phi_s \sin\delta' - \frac{m P_{n\alpha\theta}^m \sin m\phi_s \cos\delta'}{\sin\alpha} \right] \right. \\ &\quad \left. + ia_n h_n(kr_s') \sum_{\substack{m=0 \\ m+n \text{ even}}}^n \left[\frac{-m^2 P_{n\alpha}^m \cos m\phi_s \sin\delta' + m P_{n\alpha}^m \sin m\phi_s \cos\delta'}{\sin\theta_s \sin\alpha} + \frac{m P_{n\alpha}^m \sin m\phi_s \cos\delta'}{\sin\theta_s'} \right] \right\} \\ &+ 2iE_0' \sum_{n=1}^{\infty} \frac{(2n+1)}{(i)^n n(n+1)} \left\{ a'_n \left[\frac{kr_s h_n(kr_s)}{kr_s'} \right]' \sum_{\substack{m=0 \\ m+n \text{ odd}}}^n \left[\frac{m^2 P_{n\alpha}^m \cos m\phi_s \cos\delta' + m P_{n\alpha}^m \sin m\phi_s \sin\delta'}{\sin\theta_s \sin\alpha} + \frac{m P_{n\alpha}^m \sin m\phi_s \sin\delta'}{\sin\theta_s'} \right] \right. \\ &\quad \left. - ia_n h_n(kr_s') \sum_{\substack{m=0 \\ m+n \text{ even}}}^n \left[P_{n\alpha\theta}^m \cos m\phi_s \cos\delta' + \frac{m P_{n\alpha\theta}^m \sin m\phi_s \sin\delta'}{\sin\alpha} \right] \right\} \quad (2.65) \end{aligned}$$

where,

$$\begin{aligned} a_n &= -\frac{j_n(ka)}{h_n(ka)} \\ a'_n &= -\frac{[ka j_n(ka)]'}{[ka h_n(ka)]'} \end{aligned} \quad (2.66)$$

and

$$P_n^m = \epsilon \frac{(n-m)!}{m(n+m)!} P_n^m(\cos\theta_s') P_n^m(\cos\alpha) \quad (2.67)$$

$$E_0' = E_0 \frac{e^{ikC_s}}{kC_s} f(\theta_c, \pi - \Phi_s) \quad (2.68)$$

The subscripts α and θ of P_n^m denote differentiation with respect to α or θ of the appropriate Legendre function $P_n^m(\cos \alpha)$ or $P_n^m(\cos \theta_s)$ in equation (2.67).

2.3.3 Far-zone Backscatter

As in the cylindrical case, only the far-zone backscattered field will be considered. Therefore,

$$r'_s = C_s$$

$$\theta'_s = \theta_c \quad (2.69)$$

$$\phi'_s = \pi$$

Consider the expressions for P_n^m given by equation (2.67) and its derivatives. Substitute the variables from equations (2.64) and (2.69).

Then,

$$P_n^m = \epsilon_m \frac{(n-m)!}{m(n+m)!} \left[P_n^m(\cos \theta_c) \right]^2 \quad (2.70)$$

$$\begin{aligned} P_{n\alpha}^m &= \epsilon_m \frac{(n-m)!}{m(n+m)!} P_n^m(\cos \theta_c) P_n^{m'}(\cos \theta_c) \sin \theta_c \quad (2.71) \\ &= -P_{n\theta}^m \end{aligned}$$

But²⁸,

$$P_n^{m'}(\cos \theta_c) = \frac{1}{\sin^2 \theta_c} \left[-n \cos \theta_c P_n^m(\cos \theta_c) + (n+m) P_{n-1}^m(\cos \theta_c) \right] \quad (2.72)$$

Let

$$Q_n^m = n \cos \theta_c - (n+m) \frac{P_{n-1}^m(\cos \theta_c)}{P_n^m(\cos \theta_c)} \quad (2.73)$$

Then,

$$P_{n\theta}^m = -P_{n\alpha}^m = P_n^m \frac{\rho_n^m}{\sin \theta_c} \quad (2.74)$$

$$P_{n\alpha\theta}^m = -P_n^m \left\{ \frac{\rho_n^m}{\sin \theta_c} \right\}^2$$

Second, consider the function $h_n(kr_s)$ and its derivatives. Since $r_s = C_s$ is large, $h_n(kr_s)$ may be approximated by the first term of its asymptotic expansion²⁷.

$$h_n(kr'_s) \sim -ie \frac{ikC_s(i)^{-n}}{kC_s} \quad (2.75)$$

$$\frac{[kr'_s h_n(kr'_s)]'}{kr'_s} \sim \frac{e^{ikC_s} (i)^{-n}}{kC_s}$$

Equation (2.65) for the backscattered field from the s^{th} hemisphere simplifies under the above approximations and substitutions to the following expression.

$$\begin{aligned} \bar{E}_{s'} \approx & -2iE'_0 \frac{e^{ikC_s}}{kC_s} \left\{ \left[\sum_{n=1}^{\infty} \frac{(-1)^n (2n+1)}{n(n+1)} \left\{ a_n \sum_{m=0}^n \frac{(-1)^{m+m+m^2} P_n^m P_n^{m^2}}{\sin^2 \theta_c} + a_n \sum_{m=0}^n \frac{(-1)^{m^2+m} P_n^m}{\sin^2 \theta_c} \right\} \sin(\delta - \Phi_s) \bar{\epsilon}_{\theta_{s'}} \right. \right. \\ & \left. \left. + \left[\sum_{n=1}^{\infty} \frac{(-1)^n (2n+1)}{n(n+1)} a_n \sum_{m=0}^n \frac{(-1)^{m^2+m} P_n^m}{\sin^2 \theta_c} - a_n \sum_{m=0}^n \frac{(-1)^{m+m+m^2} P_n^m P_n^{m^2}}{\sin^2 \theta_c} \right] \cos(\delta - \Phi_s) \bar{\epsilon}_{\theta_{s'}} \right\} \end{aligned} \quad (2.76)$$

The scattered field given by the above expressions is resolved into spherical components in the x'_s, y'_s, z'_s coordinate system. The final form of the field equations is most conveniently given as components in the antenna coordinate system. In this case, the components

can be recognized as the direct and cross-polarized components. Let

$$\overline{E}_{s'} = -2iE'_o \frac{e}{kC_s} \left[E_{\theta_s} \sin(\delta - \Phi_s) \overline{\epsilon}_{\theta_{s'}} + E_{\phi_s} \cos(\delta - \Phi_s) \overline{\epsilon}_{\phi_{s'}} \right] \quad (2.77)$$

Now, resolve these components into the corresponding rectangular components.

That is, as in equation (2.48), and using (2.69),

$$\begin{aligned} \overline{E}_{s'} = -2iE'_o \frac{e}{kC_s} \left[E_{\theta_s} \sin(\delta - \Phi_s) \cos\theta_c \overline{i}_{s'} + E_{\phi_s} \cos(\delta - \Phi_s) \overline{j}_{s'} \right. \\ \left. + E_{\theta_s} \sin(\delta - \Phi_s) \sin\theta_c \overline{k}_{s'} \right] \end{aligned} \quad (2.78)$$

From equation (2.61),

$$\begin{aligned} \overline{i}_{s'} &= -\cos\Phi_s \overline{i}_a + \sin\Phi_s \overline{j}_a \\ \overline{j}_{s'} &= \sin\Phi_s \overline{i}_a + \cos\Phi_s \overline{j}_a \\ \overline{k}_{s'} &= -\overline{k}_a \end{aligned} \quad (2.79)$$

So that at the antenna,

$$\begin{aligned} \overline{E}_s = 2iE_o \frac{e}{kC_s} \left\{ \right. \\ \left. \left[-E_{\theta_s} \sin(\delta - \Phi_s) \cos\theta_c \cos\Phi_s + E_{\phi_s} \cos(\delta - \Phi_s) \sin\Phi_s \right] \overline{i}_a \right. \\ \left. + \left[E_{\theta_s} \sin(\delta - \Phi_s) \cos\theta_c \sin\Phi_s + E_{\phi_s} \cos(\delta - \Phi_s) \cos\Phi_s \right] \overline{j}_a \right. \\ \left. - E_{\theta_s} \sin(\delta - \Phi_s) \sin\theta_c \overline{k}_a \right\} \end{aligned} \quad (2.80)$$

It is sufficient, however, to consider only the two polarizations for

$\delta = \frac{1}{2}\pi$ and $\delta = 0$ respectively. That is,

$$\begin{aligned} \overline{E}_s^{\parallel} = 2iE_o \left[\frac{e^{ikC_s}}{kC_s} \right]^2 f^{\parallel}(\theta_c, \pi - \Phi_s) \left\{ \right. \\ \left. \left[-E_{\theta_s} \cos^2 \Phi_s \cos \theta_c + E_{\phi_s} \sin^2 \Phi_s \right] \overline{i}_a \right. \\ \left. + \left[E_{\theta_s} \cos \theta_c + E_{\phi_s} \right] \sin \Phi_s \cos \Phi_s \overline{j}_a \right. \\ \left. - E_{\theta_s} \cos \Phi_s \sin \theta_c \overline{k}_a \right\} \end{aligned} \quad (2.81)$$

and

$$\begin{aligned} \overline{E}_s^{\perp} = 2iE_o \left[\frac{e^{ikC_s}}{kC_s} \right]^2 f^{\perp}(\theta_c, \pi - \Phi_s) \left\{ \right. \\ \left[E_{\theta_s} \cos \theta_c + E_{\phi_s} \right] \sin \Phi_s \cos \Phi_s \overline{i}_a \\ \left. + \left[-E_{\theta_s} \sin^2 \Phi_s \cos \theta_c + E_{\phi_s} \cos^2 \Phi_s \right] \overline{j}_a \right. \\ \left. + E_{\theta_s} \sin \Phi_s \sin \theta_c \overline{k}_a \right\} \end{aligned} \quad (2.82)$$

2.3.4 Normalization of Field Equations

Again, the normalized total backscattered field is the actual quantity which should be considered. Since the plane reference surface will not depolarize the incident radiation, the direct and depolarized components must be considered separately. That is,

$$E^{\parallel, \perp} = 1 + \frac{E_{\text{obj}}}{E_{\text{plane}}^{\parallel, \perp}} \quad (2.83)$$

as in equation (2.40) for the direct components. For the depolarized

components however,

$$E_{\parallel, \perp}^{\text{obj}} = \frac{E_{\text{obj}}}{E_{\parallel, \perp}^{\text{plane}}} \quad (2.84)$$

E_{plane} is, as before, the image of the incident field in the plane. The geometry is similar to that shown in figure 2.3 with $\alpha = 0$.

$$E_{\parallel, \perp}^{\text{plane}} = \pm E_0 \frac{e^{i2kL}}{2kL} \quad (2.85)$$

It must be noted that the total field scattered by the ensemble of objects will be given simply by the vector sum of the field scattered by each object, since the single scatter approximation is assumed. The normalization of the total field given by the sum over s of equations (2.81) and (2.82) by equations (2.84) and (2.85) may now be performed. First, the various polarization components of equation (2.83) must be recognized. That is, the field is in the form

$$\begin{aligned} \overline{E}^{\parallel} &= E_{11} \overline{i}_a + E_{12} \overline{j}_a + E_1 \overline{k}_a \\ \overline{E}^{\perp} &= E_{21} \overline{i}_a + E_{22} \overline{j}_a + E_2 \overline{k}_a \end{aligned} \quad (2.86)$$

where

E_{11} is the direct component due to the \parallel pol. incident wave

E_{12} is the depolarized component due to the \parallel pol. incident wave

E_{21} is the depolarized component due to the \perp pol. incident wave

E_{22} is the direct component due to the \perp pol. incident wave

These four components may now be correctly normalized. The other components E_1 and E_2 along the z_a axis are not considered here for two reasons. First, they will not be detected by an antenna in the same or cross-polarized

orientation as the transmitting antenna, which is physically the most realistic configuration. Second, they will tend to cancel out when averaged over the ensemble of the objects if the objects are distributed according to a continuous uniform distribution. This point will be further discussed in Chapter 4.

The normalized backscattered field from an array of perfectly conducting hemispheres on a perfectly conducting ground plane, illuminated by a narrow beam antenna at normal incidence, by the single scatter approximation can now be cast into the form:

$$\begin{aligned}
 E_{11} &= 1 + 4ikL \left\{ \frac{ik(C_s - L)}{kC_s} \right\}^2 f(\theta_c, \pi - \Phi_s) \left[-E_{\theta_s} \cos^2 \Phi_s \cos \theta_c + E_{\phi_s} \sin^2 \Phi_s \right] \\
 E_{12} &= 4ikL \left\{ \frac{ik(C_s - L)}{kC_s} \right\}^2 f(\theta_c, \pi - \Phi_s) \left[E_{\theta_s} \cos \theta_c + E_{\phi_s} \right] \sin \Phi_s \cos \Phi_s \\
 E_{21} &= 4ikL \left\{ \frac{ik(C_s - L)}{kC_s} \right\}^2 f(\theta_c, \pi - \Phi_s) \left[E_{\theta_s} \cos \theta_c + E_{\phi_s} \right] \sin \Phi_s \cos \Phi_s \\
 E_{22} &= 1 + 4ikL \left\{ \frac{ik(C_s - L)}{kC_s} \right\}^2 f(\theta_c, \pi - \Phi_s) \left[-E_{\theta_s} \sin^2 \Phi_s \cos \theta_c + E_{\phi_s} \cos^2 \Phi_s \right]
 \end{aligned} \tag{2.87}$$

2.4 Antenna Model

It is now possible to choose a specific function for the antenna space factors $f(\theta)$ and $f(\theta, \phi)$ respectively. There are several choices which could be made. The simplest one is the rectangular

$$f(\theta) = \begin{cases} 1, & -\theta_0 \leq \theta \leq \theta_0 \\ 0, & |\theta| > \theta_0 \end{cases} \quad (2.88)$$

This simple case was dismissed because the function has no sidelobes; only the beamwidth can be controlled. A slightly more complex function was tested and found to be a reasonable representation of a narrow beam antenna with readily controllable beamwidth and sidelobe level. The model chosen is that of an aperture with an appropriate illuminating function $\cos^n(\frac{1}{2}\pi x)$

The form of the space factor for the radiator is a slightly modified version of that given by Silver⁴.

$$g_n(u) = \frac{\cos\left(\frac{90(n+2)}{\theta_0}u\right)}{\prod_{k=0}^{(n-1)/2} \left[1 - \left(\frac{2}{\sqrt{\pi}}\left(\frac{90(n+2)u}{(2k+1)\theta_0}\right)^2\right) \right]} \quad n \text{ odd} \quad (2.89)$$

$$g_n(u) = \frac{\sin\left(\frac{90(n+2)}{\theta_0}u\right) / \left(\frac{90(n+2)}{\theta_0}u\right)}{\prod_{k=0}^{n/2} \left[1 - \left(\frac{2}{\sqrt{\pi}}\left(\frac{90(n+2)u}{2k\theta_0}\right)^2\right) \right]} \quad n \text{ even}$$

where

$$f(\theta) = g_n(\sin \theta) \quad (2.90)$$

and θ_0 is the angular distance to the first null of the beam in degrees. The integer n reduces the sidelobe level in discrete steps as n is increased. Note that $n = 0$ and $n = 1$ reduce equation (2.89) to the approximate radiation patterns of an open waveguide in the E-plane and H-plane respectively.

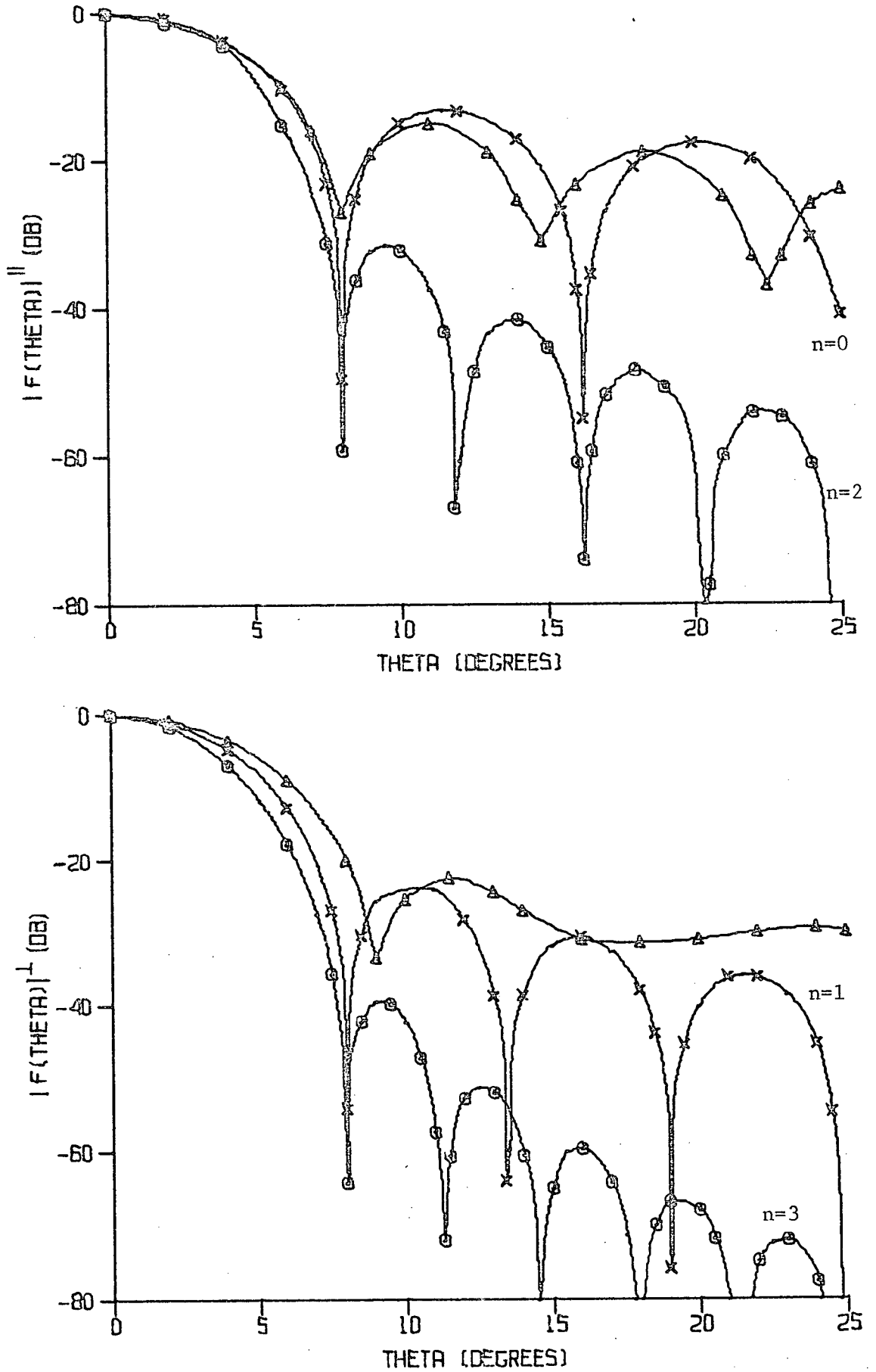


Figure 2.5 Radiation Patterns for Horn Antenna (\triangle) and for Approximate Beam Functions.

A comparison of (2.89) with the actual radiation pattern of a horn antenna is shown in figure 2.5. Here it can be seen that the simple forms given with $n = 0$ and $n = 1$ are sufficient to quite accurately describe this particular antenna. Therefore, the functions

$$g_{\parallel}^{\parallel}(u) = \frac{\sin\left(\frac{180}{\theta_e}u\right)}{\left(\frac{180}{\theta_e}u\right)} \quad (2.91)$$

$$g_{\perp}^{\perp}(u) = \frac{\cos\left(\frac{270}{\theta_h}u\right)}{1 - \left(\frac{2}{\pi}\right)^2 \left(\frac{270}{\theta_h}u\right)^2}$$

will be used almost exclusively for the study of the hemicylinder problem. For the three dimensional problem it is sufficient to consider the product of the above two functions with suitable arguments:

$$\begin{aligned} g_{\parallel}^{\parallel}(u,v) &= \frac{\sin\left(\frac{180}{\theta_e}v\right)}{\left(\frac{180}{\theta_e}v\right)} \frac{\cos\left(\frac{270}{\theta_h}u\right)}{1 - \left(\frac{2}{\pi}\right)^2 \left(\frac{270}{\theta_h}u\right)^2} \\ &= g(u,v) \end{aligned} \quad (2.92)$$

Similarly,

$$g_{\perp}^{\perp}(u,v) = g(v,u) \quad (2.93)$$

where

$$f(\theta, \phi) = g(\sin\theta \cos\phi, \sin\theta \sin\phi) \quad (2.94)$$

The subscripts e and h on the beamwidths refer to the beamwidths for the pattern in the E-plane and H-plane of the antenna.

2.5 Restriction to Narrow Beamwidth

As has already been mentioned, it was decided to use the beam factors (2.91) and (2.92) because of their similarity to a laboratory horn antenna. Therefore, it is also reasonable to assume that the beamwidths to be considered will be of the same order as that of an actual antenna. An effective surface area may now be introduced which is a function of the beamwidth, and suitable approximations may be made which simplify the final form of the field equations.

2.5.1 Two Dimensional Case

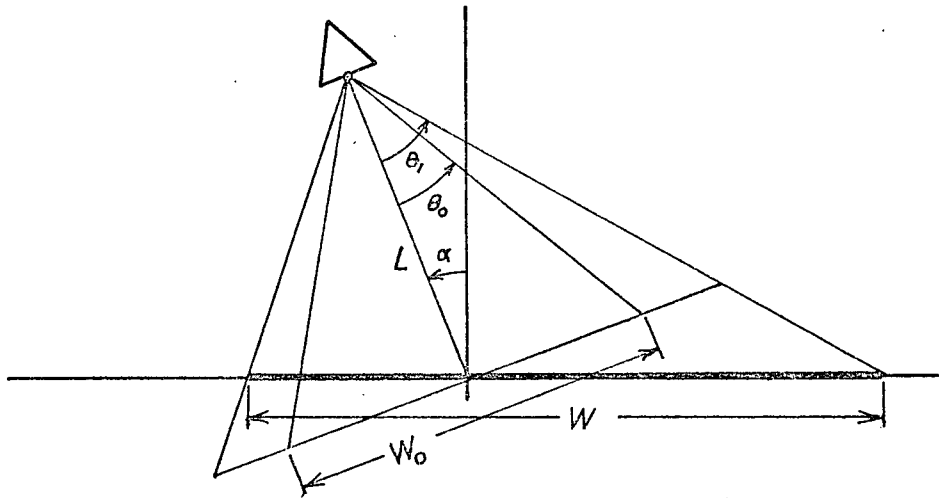


Figure 2.6 Effective Surface Width

Let θ_0 be the angular distance to the first minimum of the radiation pattern. Then from figure 2.6

$$W_0 = 2L \tan \theta_0 \quad (2.95)$$

$$W = \frac{L \sin \theta_1}{\cos(\theta_1 - \alpha)} + \frac{L \sin \theta_1}{\cos(\theta_1 + \alpha)} \quad (2.96)$$

Define a constant K such that

$$K \tan \theta_0 = \tan \theta_1 \quad (2.97)$$

and let

$$C_a = 2K \tan \theta_0 \quad (2.98)$$

Further assume that the coordinate, X_s , may be derived from some normalized distribution, ρ_s , $-\frac{1}{2} \leq \rho_s \leq \frac{1}{2}$. Then

$$X_s = W(\rho_s + \frac{1}{2}) - \frac{L \sin \theta_1}{\cos(\theta_1 - \alpha)} \quad (2.99)$$

$$= L \sin \theta_1 \left[\frac{\rho_s - \frac{1}{2}}{\cos(\theta_1 - \alpha)} + \frac{\rho_s + \frac{1}{2}}{\cos(\theta_1 + \alpha)} \right] \quad (2.100)$$

$$= \frac{1}{2} L C_a \frac{2\rho_s \cos \alpha + \frac{1}{2} C_a \sin \alpha}{\cos^2 \alpha - (\frac{1}{2} C_a)^2 \sin^2 \alpha} \quad (2.101)$$

Let

$$\rho'_s = \frac{1}{2} \frac{2\rho_s \cos \alpha + \frac{1}{2} C_a \sin \alpha}{\cos^2 \alpha - (\frac{1}{2} C_a)^2 \sin^2 \alpha} \quad (2.102)$$

Then

$$X_s = L C_a \rho'_s \quad (2.103)$$

Note that the condition

$$\alpha < \frac{1}{2}\pi - \theta_1 \quad (2.104)$$

must be fulfilled in order that the surface width, W , may be kept finite. This stipulation rules out the case of grazing incidence. For this part of the problem a different method must be devised for determining the width of the effective scattering area, and will not be discussed here. Equations (2.4) and (2.103) may now be combined to give

$$C_s = L \sqrt{(C_a \rho'_s + \sin \alpha)^2 + \cos^2 \alpha} \quad (2.105)$$

$$= LC'_s \quad (2.106)$$

The constant K of equation (2.97) can be determined by increasing its value until computed field values become constant. This will be investigated thoroughly in Chapters 3 and 4 for the periodic and random cases, respectively.

At this point, the discussion of the two dimensional case will also be restricted to normal incidence only. It seems pointless to keep the more general case as the three dimensional problem has already been restricted in this manner. It should however be pointed out that unlike the three dimensional case, all but grazing incidence can easily be considered in the two dimensional problem if it is desired. Since

$$C_a \rho_s \ll 1 \quad (2.107)$$

for a narrow beam, the following relationships are applicable.

$$W = LC_a \quad (2.108)$$

$$\rho'_s = \rho_s \quad (2.109)$$

$$C_s \approx L(1 + \frac{1}{2}C_a^2 \rho_s^2) \quad (2.110)$$

$$\sin \beta_s \approx 1 - \frac{1}{2}C_a^2 \rho_s^2 \quad (2.111)$$

$$\cos \beta_s \approx C_a \rho_s \quad (2.112)$$

These approximations may now be introduced into the field equations (2.23), (2.24), (2.25) and (2.26) along with the antenna function (2.91) to give the final form of the scattered field due to the array of hemicylinders:

$$E^{\parallel} = 1 + Ce^{-ikL} \sum_{s=1}^{N_0} U_s^{\frac{1}{2}} \sum_{n=0}^N (-1)^n X_{ns} \cos n\beta_s \quad (2.113)$$

$$E^{\perp} = 1 + iCe^{-ikL} \sum_{s=1}^{N_0} U_s^{\frac{1}{2}} \sum_{n=1}^N (-1)^n Y_{ns} \sin n\beta_s$$

where

$$X_{ns} = A_n^{\parallel} \left\{ \frac{e^{ikL}}{\sqrt{kL}} U_s^{\frac{1}{2}} g^{\parallel}(C_a \rho_s) \cos n\beta_s + \sum_{\substack{t=1 \\ t \neq s}}^{N_0} \sum_{m=0}^N (i)^{n-m} X_{mt} H_{mn}^+(k|X_t - X_s|) F_{nm}^{st} \right\} \quad (2.114)$$

$$Y_{ns} = A_n^{\perp} \left\{ -i \frac{e^{ikL}}{\sqrt{kL}} U_s^{\frac{1}{2}} g^{\perp}(C_a \rho_s) \sin n\beta_s + \sum_{\substack{t=1 \\ t \neq s}}^{N_0} \sum_{m=1}^N (i)^{n-m} Y_{mt} H_{mn}^-(k|X_t - X_s|) F_{nm}^{st} \right\}$$

and

$$U_s = e^{ikLC_a^2 \rho_s^2} \left(1 - \frac{1}{2} C_a^2 \rho_s^2 \right) \quad (2.115)$$

$$C = \frac{4(1-i)\sqrt{2}}{\sqrt{\pi}} \quad (2.116)$$

2.5.2 Three Dimensional Case

These same approximations may be applied to the three dimensional problem. If the active scattering surface is made larger than necessary, obviously the results must remain unaffected. Therefore, assume for simplicity that the effective area is a circle instead of an ellipse, where the radius is determined by the widest of the two beamwidths of the antenna. Thus, the diameter of the active area will be given by

$$W = C_a L \quad (2.117)$$

which is the equivalent of equation (2.108). Similarly if ρ_{x_s} and ρ_{y_s} are some normalized distribution of coordinates over the circle of unit diameter, then

$$\rho_s^2 = \rho_{x_s}^2 + \rho_{y_s}^2 \quad (2.118)$$

and therefore,

$$R_s = LC_a \rho_s \quad (2.119)$$

$$\tan \Phi_s = \frac{\rho_{y_s}}{\rho_{x_s}}$$

Furthermore, (2.111) still holds so that equations (2.56) and (2.57) become

$$C_s \approx L(1 + \frac{1}{2} C_a^2 \rho_s^2) \quad (2.120)$$

$$\cos \theta_c \approx 1 - \frac{1}{2} C_a^2 \rho_s^2 \quad (2.121)$$

$$\sin \theta_c \approx C_a \rho_s \quad (2.122)$$

as for the two dimensional case. The above approximations considerably simplify the expressions (2.87) for the scattered field, especially the functions E_{θ_s} and E_{ϕ_s} . These functions may now be expanded as a power series in the small quantity $C_a \rho_s$. These complex functions of spherical Bessel functions and Legendre functions have already been simplified by the restriction to normal incidence. In fact, if non-normal incidence is considered the following approximations do not yield a more usable form of the Legendre functions. From equation (2.76) it can be seen that the functions

$$f_{nm}^s = \frac{(-1)^m P_n^m Q_n^m}{\sin^2 \theta_c} \quad (2.123)$$

and

$$g_{nm}^s = \frac{(-1)^m P_n^m}{\sin^2 \theta_c} \quad (2.124)$$

are to be determined. The following approximation may be applied for

small θ_c :

$$P_n^m(\cos\theta_c) \approx \frac{(-1)^m}{2^{\frac{1}{2}m}} (1 - \cos\theta_c)^{\frac{1}{2}m} \frac{(n+m)!}{m!(n-m)!} \quad (2.125)$$

$$\approx \frac{(-1)^m (C_a \rho_s)^m}{2^{\frac{1}{2}m}} \frac{(n+m)!}{m!(n-m)!}$$

Note that for non-normal incidence, $\cos\theta_c \ll 1$ and hence the above expression becomes a much more complicated function of $C_a \rho_s$. Now,

$$Q_n^m \approx m - \frac{1}{2}n C_a^2 \rho_s^2 \quad (2.126)$$

$$P_n^m \approx \epsilon_m \frac{(n+m)!}{m!(n-m)!} \frac{(C_a \rho_s)^{2m}}{2^{2m}}$$

so that

$$f_{nm}^s \approx \frac{(-1)^m \epsilon_m (n+m)!}{(m!)^2 (n-m)!} \frac{(C_a \rho_s)^{2(m-1)}}{2^{2m}} \left[m^2 - mn C_a^2 \rho_s^2 + \frac{1}{4}n^2 C_a^4 \rho_s^4 \right] \quad (2.127)$$

$$g_{nm}^s \approx \frac{(-1)^m \epsilon_m (n+m)!}{(m!)^2 (n-m)!} \frac{(C_a \rho_s)^{2(m-1)}}{2^{2m}}$$

combine equations (2.127) and (2.77), keeping only terms to the order of $(C_a \rho_s)^2$. This operation yields

$$E_{\theta_s} = \sum_{n=1}^{\infty} \frac{(-1)^n (2n+1)}{n(n+1)} \left[-a' \sum_{m=0}^n f_{nm}^s + a \sum_{m=0}^n g_{nm}^s \right] \quad (2.128)$$

m+n odd m+n even

$$\approx \frac{1}{2}b(1 + b_{\theta} C_a^2 \rho_s^2)$$

where

$$b = \sum_{n=1}^{\infty} (2n+1) \begin{cases} a'_n, & n \text{ even} \\ a_n, & n \text{ odd} \end{cases} \quad (2.129)$$

$$b_{\theta} = \frac{1}{b} \sum_{n=1}^{\infty} (2n+1) \begin{cases} -na'_n + \frac{1}{4}(n+2)(n-1)a_n, & n \text{ even} \\ \left[\frac{n}{2(n+1)} + \frac{1}{2}(n+2)(n-1) \right] a'_n, & n \text{ odd} \end{cases} \quad (2.130)$$

Similarly,

$$E_{\phi_s} \approx -\frac{1}{2}b \left(1 + b_{\phi} C_{a_s}^2 O_s^2 \right) \quad (2.131)$$

where

$$b = \frac{1}{b} \sum_{n=1}^{\infty} (2n+1) \begin{cases} \left[\frac{n}{2(n+1)} + \frac{1}{4}(n+2)(n-1) \right] a_n, & n \text{ even} \\ -na_n + \frac{1}{4}(n+2)(n-1) a'_n, & n \text{ odd} \end{cases} \quad (2.132)$$

The final simplified form of the backscattered field by an array of hemispheres on a perfectly conducting ground plane for narrow beamwidth and normal incidence therefore becomes:

$$E_{11} = 1 - \frac{2ib}{kL} e^{i2kLC} a_s^2 O_s^2 g(C_{a_s} O_s \cos \bar{\Phi}_s, C_{a_s} O_s \sin \bar{\Phi}_s) \left[1 + \left(b_{\theta} - \frac{1}{2} \right) \cos^2 \bar{\Phi}_s + b_{\phi} \sin^2 \bar{\Phi}_s - 1 \right] C_{a_s}^2 O_s^2$$

$$E_{12} = \frac{2ib}{kL} e^{ikLC} a_s^2 O_s^2 g(C_{a_s} O_s \cos \bar{\Phi}_s, C_{a_s} O_s \sin \bar{\Phi}_s) \left\{ \left(b_{\theta} - \frac{1}{2} \right) - b_{\phi} \right\} C_{a_s}^2 O_s^2 \sin \bar{\Phi}_s \cos \bar{\Gamma}_s \quad (2.133)$$

$$E_{21} = \frac{2ib}{kL} e^{i2kLC} a_s^2 O_s^2 g(C_{a_s} O_s \sin \bar{\Phi}_s, C_{a_s} O_s \cos \bar{\Phi}_s) \left\{ \left(b_{\theta} - \frac{1}{2} \right) - b_{\phi} \right\} C_{a_s}^2 O_s^2 \sin \bar{\Phi}_s \cos \bar{\Phi}_s$$

$$E_{22} = 1 - \frac{2ib}{kL} e^{i2kLC} a_s^2 O_s^2 g(C_{a_s} O_s \sin \bar{\Phi}_s, C_{a_s} O_s \cos \bar{\Phi}_s) \left[1 + \left(b_{\theta} - \frac{1}{2} \right) \sin^2 \bar{\Phi}_s + b_{\phi} \cos^2 \bar{\Phi}_s - 1 \right] C_{a_s}^2 O_s^2$$

The above equations will be used for all the statistical studies on the three dimensional surface in Chapter 4. Similar two dimensional equations are given at the end of the next chapter, after a more detailed investigation of their more exact counterparts has been made.

2.6 Importance and Range of Parameters

Before any results (statistical or otherwise) are obtained from equations (2.114) or (2.133) it is advantageous to summarize the restrictions and proposed treatment of all the parameters of the problem. It is instructive at this time to decide upon suitable values for these parameters which naturally divide into two sections, those of the beam, and those of the surface, as listed in Table 2.1.

The reasons for the choices shown are the following. The angle of incidence is chosen mainly for convenience. n and θ_0 are chosen to agree with the laboratory antenna, while L is chosen to put the surface just into the far field of this antenna using the criterion⁴

$$R^2 \gg \frac{D^2}{\lambda} \quad (2.134)$$

The upper limits of the size of the objects and object density are directly related to multiple scatter, and will be investigated in the next chapter. The factor K will be determined for the periodic and random problems, and the results for both cases will be compared.

With these ideas in mind, the periodic configuration of scatterers may now be investigated.

Parameter	Description	Treatment	Value as fixed parameter
Antenna Parameters			
α	angle of incidence	set to normal incidence, $\alpha = 0$, for convenience	$\alpha = 0$
n	sidelobe level is a function of n	vary to find effect of sidelobes	$n^{\parallel} = 0$ $n^{\perp} = 1$
L	distance from antenna to surface	vary to find effect of antenna position	$L = 80\lambda$
θ_0	width of main beam	vary to find effect of beamwidth keeping $\theta_0 < 30^\circ$	$\theta_e = 8^\circ$ $\theta_h = 8^\circ$
Surface Parameters			
a	radius of objects	variable, but of lesser importance use a few values ≤ 0.5	$a = 0.2\lambda, 0.5\lambda$
K	proportionality between width of main beam and surface width	vary to find the smallest surface width required	small as possible
ρ	area density of objects	the main independent variable accuracy decreases with increasing ρ	$\rho \leq 0.25$

Table 2.1 The parameters of the Scattering Problem

3. PERIODIC ARRAYS OF HEMICYLINDERS

One of the simplest rough surface problems is that of the two dimensional periodic array of hemicylinders. As has already been mentioned, there are three main reasons for choosing this simple configuration. First, exact numerical values may be obtained for the X_{ns} and Y_{ns} of equations (2.114) so that the single scatter approximation (and other higher order approximations) may be compared with the exact solution. Second, the periodic results can be indicative of the behaviour of the random problem. In fact, it is hoped that any estimates of parameter limits will be even better for the random case due to the averaging processes. Third, all computation times are much shorter because only one configuration, not thousands, need be considered for each set of parameters. The three dimensional surface of course, will not be considered here due to its extreme complexity.

3.1 Solutions for Various Orders Of Accuracy

3.1.1 Exact Solution

In principle, equations (2.114) can be solved. The solution is obtained merely by inverting the matrix of coefficients of the X_{mt} and Y_{mt} . However, in a case where $N_o = 25$, which is quite reasonable, and $N = 5$, which corresponds to objects about 1.2λ in diameter, one is faced with solving a set of 125 simultaneous linear algebraic equations in 125 unknowns - a formidable problem. Therefore, the parameters in the cases that will be considered will be selected such that a solution is feasible.

For simplicity, locate the origin of the coordinate system at the centre of the middle hemicylinder for an odd number of hemicylinders and halfway between the two centre hemicylinders for an even number of hemicylinders as in figure 3.1.

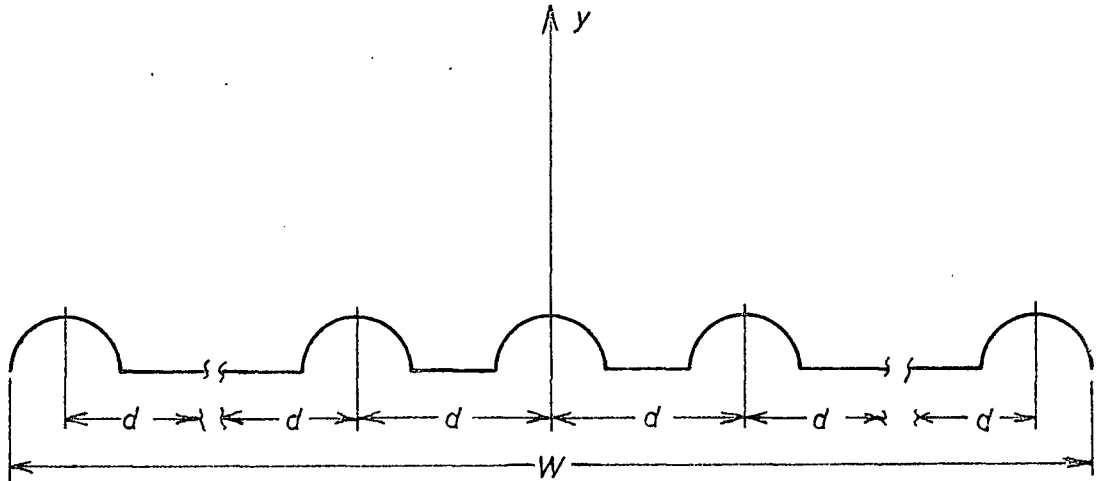


Figure 3.1 Periodic Two Dimensional Surface

Put

$$\rho_s = \begin{cases} s \left(\frac{d}{W} \right), & N_0 \text{ odd} \\ \frac{1}{2}(2s-1) \left(\frac{d}{W} \right), & N_0 \text{ even} \end{cases} \quad (3.1)$$

$$s = \begin{cases} -\frac{1}{2}(N_0-1), -\frac{1}{2}(N_0+1), \dots -1, 0, 1, \dots \frac{1}{2}(N_0-1), & N_0 \text{ odd} \\ -\frac{1}{2}N_0, -\frac{1}{2}(N_0+1), \dots \dots -1, 1, \dots \frac{1}{2}N_0, & N_0 \text{ even} \end{cases} \quad (3.2)$$

and hence

$$X_t - X_s = d(t - s) \quad (3.3)$$

Equation (3.3) when applied to the arguments of H_{mn}^+ in equations (2.23) and (2.24) immediately makes all the elements of every diagonal above and every diagonal below the main diagonal the same. Hence, the minor problem of merely calculating the elements of the coefficient matrix is now within the area of computational feasibility.

A quick glance at the number of unknowns in equations (2.114)

immediately rules out any hope of obtaining a solution by direct numerical inversion of the matrix (e.g. Gauss elimination). The digital computer available (IBM 360/67) did not have a large enough memory, and if auxiliary memory such as magnetic tape were used, the computation time and roundoff error would become prohibitive. Therefore, an iterative method, the only alternative, must be relied upon, but this does not necessarily converge in all cases. Twersky²⁹ has actually written down the series solution which one obtains by applying the method of direct iteration³⁰ to equations similar to (2.23) and (2.24). In a form suitable for iteration these can be written as

$$W_{ns} = A_n \left[C_{ns} + \sum_{\substack{t=1 \\ t \neq s}}^{N_0} \sum_{m=1}^N H_{mnst} W_{mt} \right] \quad (3.4)$$

or, more compactly

$$\bar{W} = H\bar{W} + \bar{C} \quad (3.5)$$

where the main diagonal of the matrix H is zero and H is symmetric. Then the iteration follows the scheme

$$\bar{W}^{-k+1} = H\bar{W}^{-k} + \bar{C}, \quad \bar{W}^0 = 0 \quad (3.6)$$

for the k^{th} iteration. Conditions for the convergence of (3.6) to the correct solution (the solution is correct if convergence is obtained at all) are given by Faddeeva³⁰. In fact, the matrix $H - I$, I being the unit matrix, must have a dominant main diagonal. Note that Twersky claims that (3.6) always converges for the scattering problem.

A better method is the so-called Gauss-Seidel method^{30,31}. Let

$$H = L + U \quad (3.7)$$

where L is a lower triangular and U an upper triangular matrix. Then, perform the iteration according to the scheme

$$\bar{W}^{-k+1} = L\bar{W}^{-k+1} + U\bar{W}^{-k} + \bar{C}, \quad \bar{W}^0 = 0 \quad (3.8)$$

That is, the new values are used immediately as they are calculated. Faddeeva³⁰ states that this method will converge whenever (3.6) converges, will probably converge faster, and will converge in other cases as well. Therefore this method, (3.8), was used in all subsequent calculations.

3.1.2 Nearest Neighbour Approximation

For the nearest neighbour (N-N) approximation, one stipulates that the multiple scatter is produced only by interactions between those cylinders on either side of the cylinder in question. That is,

$$H_{mnst} = \begin{cases} H_{mn}^+(kd), & t = s+1 \\ 0, & t \neq s+1 \end{cases} \quad (3.9)$$

in equation (3.4). The system matrix is now a tri-diagonal matrix which greatly reduces the amount of computation required in equation (3.8).

3.1.3 First Order Nearest Neighbour Approximation

The first order nearest neighbour approximation (N-N-1) is obtained by first assuming that there is a minimum separation of scatterers such that

$$k|X_t - X_s| \ll 1 \quad (3.10)$$

which implies a relatively low density. Then, it must be further assumed that the multiple scatter effects are small compared to the primary scattered field due to an isolated cylinder (e.g. low density and fairly small objects).

The resulting N-N-1 scattering coefficients

$$Y_{ns} \approx -iA \frac{e^{ikL}}{\sqrt{kL}} \left\{ U_{ns}^{\frac{1}{2}} h_{ns}^{\perp} - \frac{1}{4} i \sqrt{2C} \frac{e^{ikd}}{(kd)^{\frac{3}{2}}} n \left[U_{s-1}^{\frac{1}{2}} \sum_{m=1}^N (-1)^{m+n} m A_m^{\perp} h_{m,s-1}^{\perp} + U_{s+1}^{\frac{1}{2}} \sum_{m=1}^N m A_m^{\perp} h_{m,s+1}^{\perp} \right] \right\} \quad (3.11)$$

$$X_{ns} \approx A \frac{e^{ikL}}{\sqrt{kL}} \left\{ U_{ns}^{\frac{1}{2}} h_{ns}^{\parallel} + \frac{1}{4} \sqrt{2C} \frac{e^{ikd}}{(kd)^{\frac{3}{2}}} \left[U_{s-1}^{\frac{1}{2}} \sum_{m=0}^N (-1)^{m+n} m A_m^{\parallel} h_{m,s-1}^{\parallel} + U_{s+1}^{\frac{1}{2}} \sum_{m=0}^N m A_m^{\parallel} h_{m,s+1}^{\parallel} \right] \right\}$$

where

$$h_{ns}^{\parallel\perp} = g_{a,\rho_s}^{\parallel\perp} \begin{cases} \sin n\beta_s \\ \cos n\beta_s \end{cases} \quad (3.12)$$

are derived in Appendix C. Note that these are the actual coefficients; no iteration is required.

3.1.4 Single Scatter Approximation

The single scatter approximation is obtained by assuming that

$$H_{mnst} = 0 \quad (3.13)$$

for all s and t , or equivalently that the iteration scheme (3.6) converges sufficiently with no iteration at all. Therefore, only the first terms are kept in equation (3.11) with the result that

$$Y_{ns} \approx -iA \frac{e^{ikL}}{n\sqrt{kL}} U_s^{\frac{1}{2}} h_{ns}^{\perp} \quad (3.14)$$

$$X_{ns} \approx A \frac{e^{ikL}}{n\sqrt{kL}} U_s^{\frac{1}{2}} h_{ns}^{\parallel}$$

for the single scatter scattering coefficients.

3.2 Numerical Calculations of the Scattered Field

The preceding four methods for determining the X_{ns} and Y_{ns} were programmed on the IBM 360/67 digital computer along with equation (2.117) for the scattered field produced by these coefficients. Up to 30 objects and an N of 10 were allowed for. Any increase in these values would tend to use too much memory for the efficient running of the program under the MTS time-shared system.

3.2.1 Determination of Active Scattering Area

The first problem is to determine the optimum value of the ratio between the beamwidth at the surface and the necessary surface area. This factor (K in equation (2.98)) can be determined by increasing its value until the field is virtually invariant to any further increase. The results are shown in figure 3.2. The cylinders in this case are 1.0 wavelength in diameter and the spacing is 5.0 wavelengths which gives a density of 20%. For these parameter values it can be seen that the error due to the single scatter approximation is appreciable.

From figure (3.2) the smallest value of K that can be used appears to be about 1.5 and this value will be used for all further studies of the periodic surface. As K = 1 gives a surface width equal to the width of the main beam, this value (K = 1.5) implies that at least the first sidelobes make some contribution to the scattered field. Cylinder diameters of 0.4 and 0.6 wavelengths were also tried, but with similar results. The only difference to be noticed was the degree of multiple scatter.

3.2.2 Effect of the Orders of Scattering Approximations

The relative errors of the magnitude and phase of the scattered field for the single scatter and first order nearest neighbour approximations compared to the exact solution are shown in figure 3.3 and 3.4. Here, the independent variable is the area density of the objects,

$$\rho = \frac{N}{W} (2a)(100\%) \quad (3.19)$$

A density greater than 35% has not been shown because in several cases the exact solution did not converge. Similarly, a cylinder diameter greater than 1.0 wavelength was not used. This fact is in disagreement with Twersky²⁹ who claims that the series should always converge on physical grounds, although an even better converging series (3.8) was used here. As a consequence,

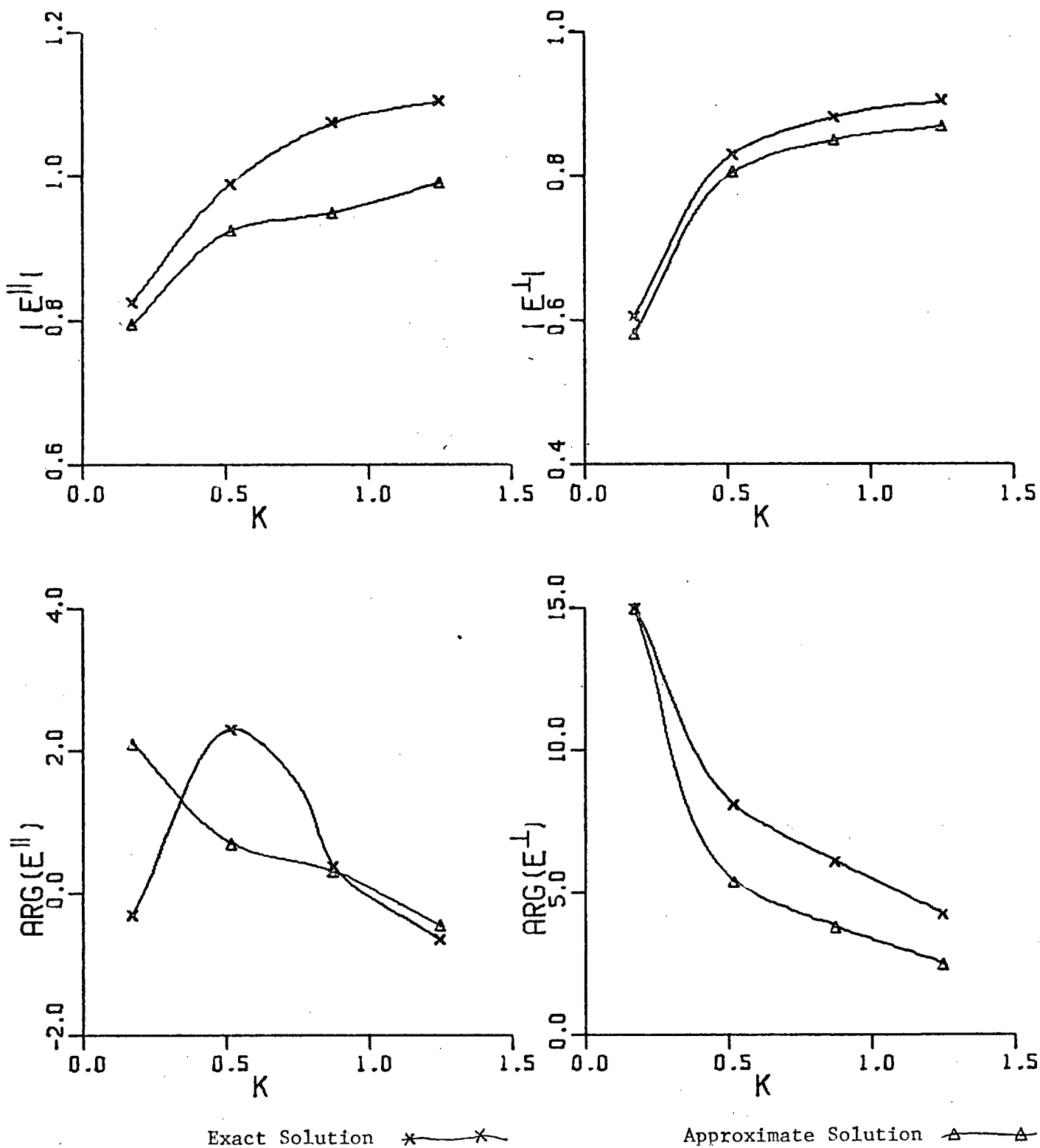


Figure 3.2 Magnitude and Phase of Scattered Field as a Function of the Ratio of Surface Width to Beamwidth.

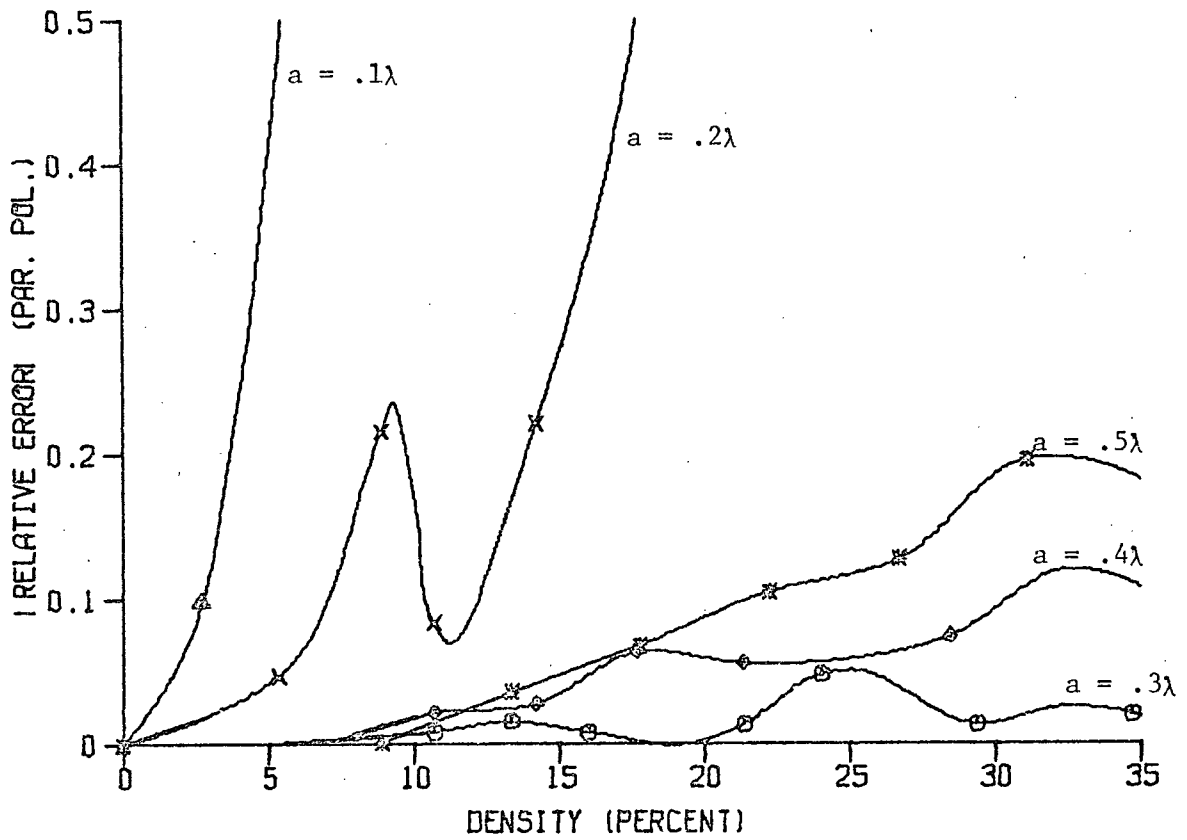
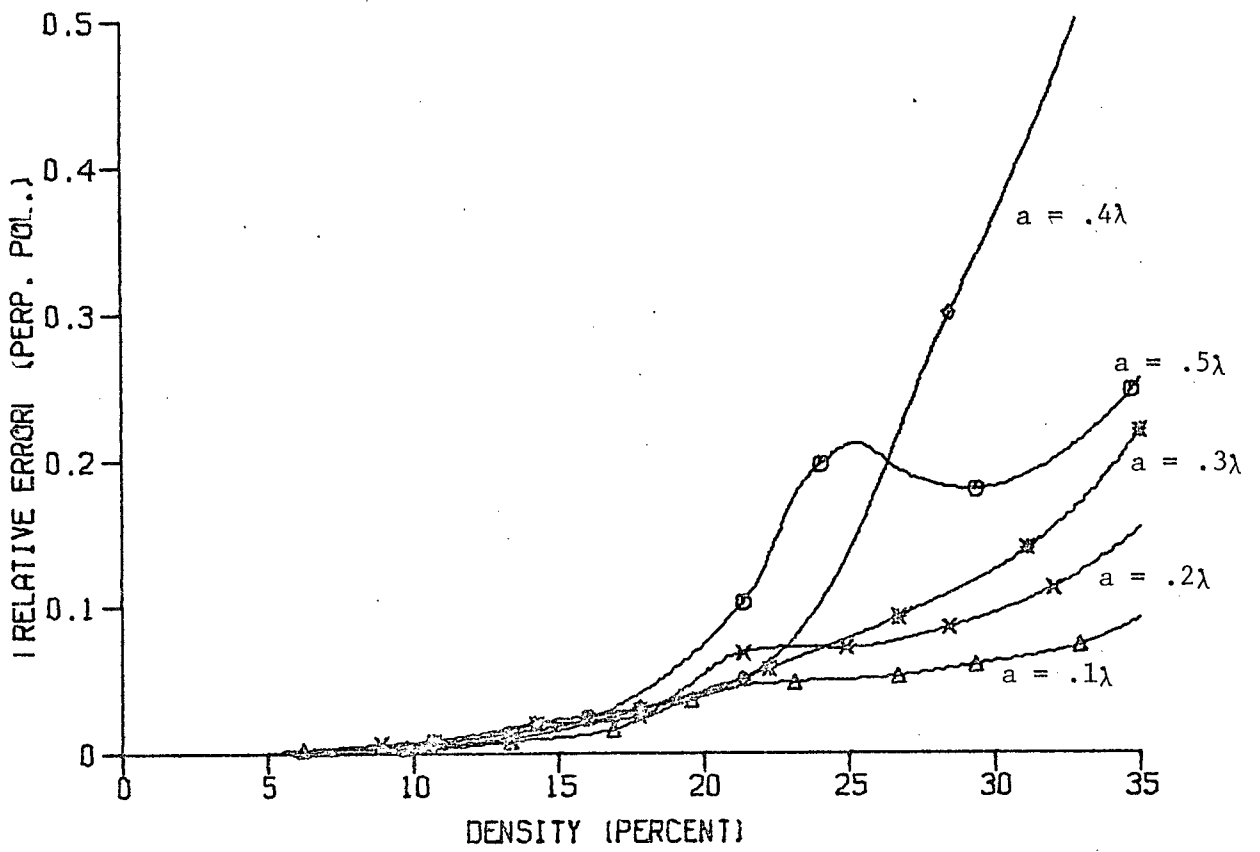


Figure 3.3 Error Introduced by the Single Scatter Approximation as a Function of Hemicylinder Density for Various Values of Hemicylinder Radius.

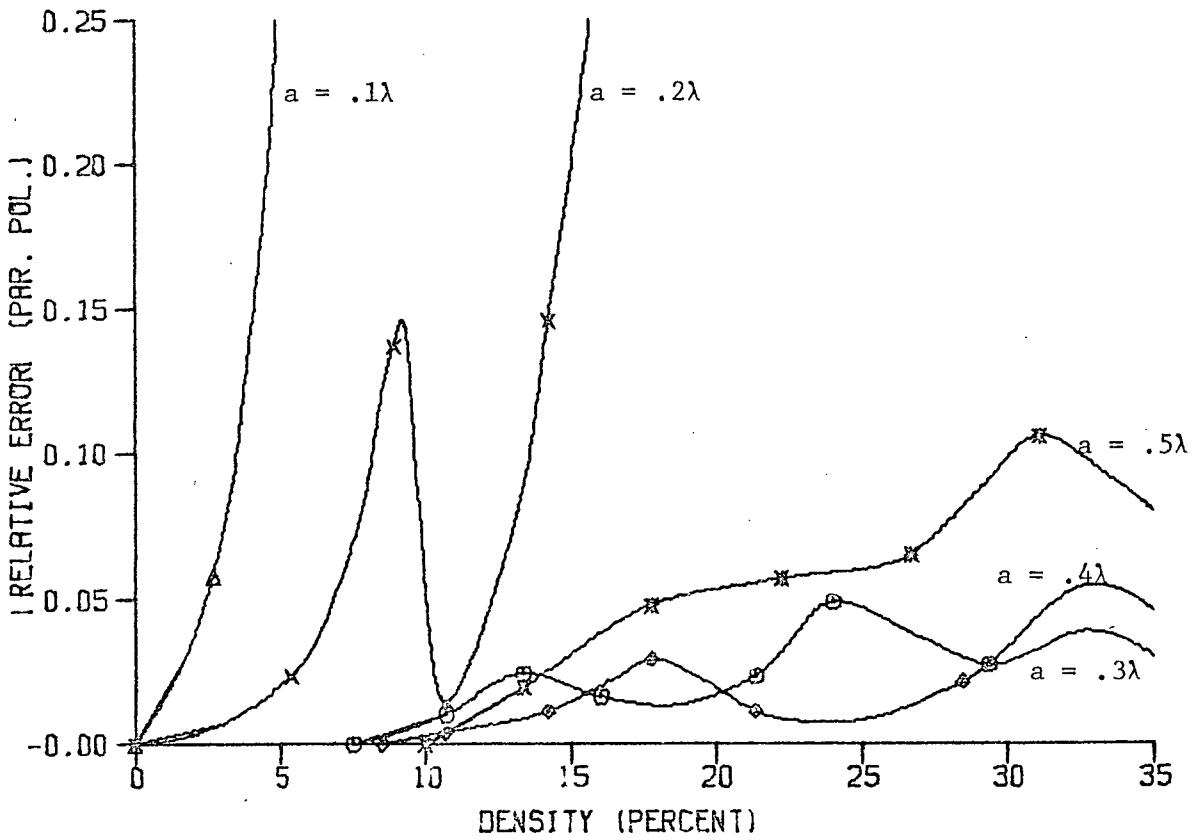
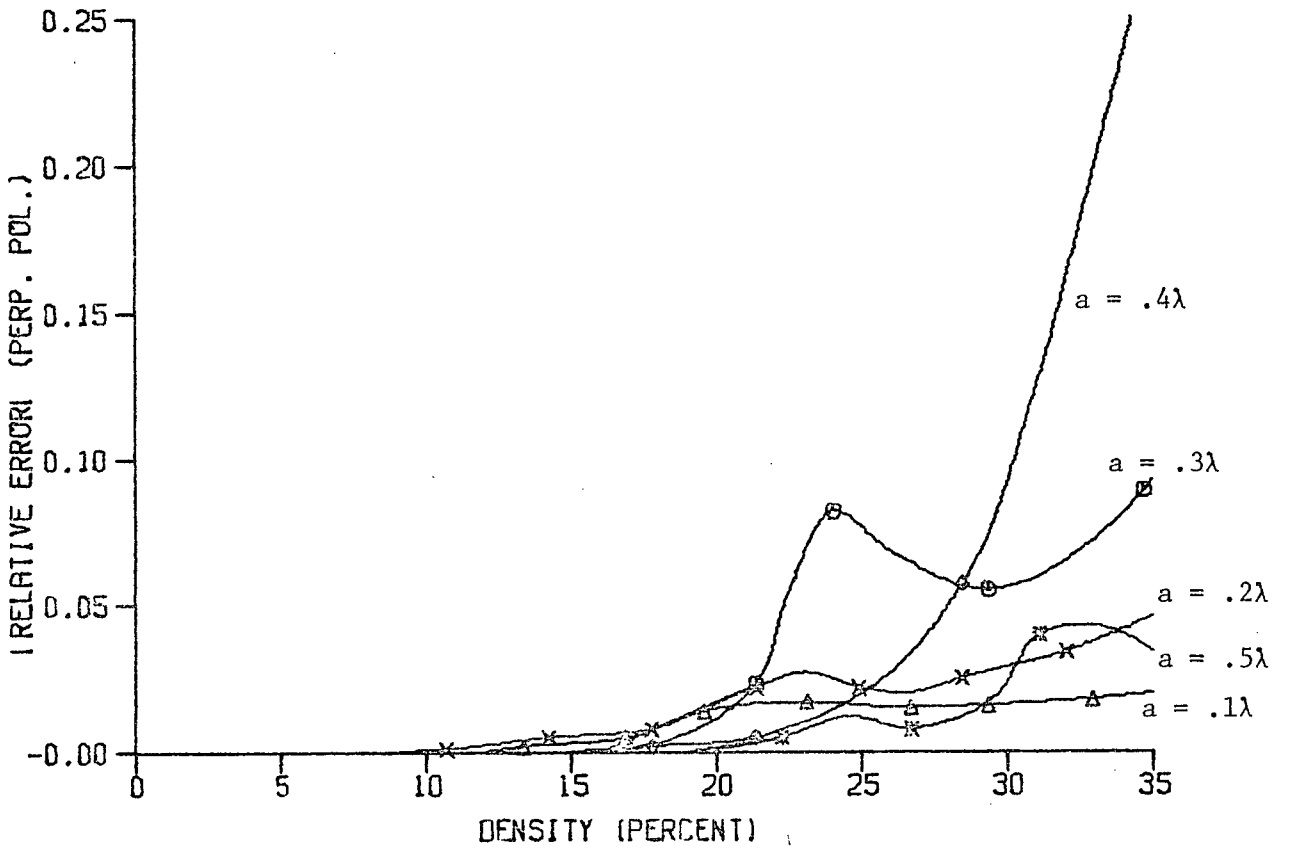


Figure 3.4 Error Introduced by the First Order Nearest Neighbour Approximation as a Function of Hemicylinder Density for Various Values of Hemicylinder Radius.

the usefulness of the series solution obtained by iteration is severely limited. In fact, it can be seen from (2.114) that the diagonal elements of the system matrix increase as the size of the objects is decreased, and the off-diagonal (multiple scattering) elements decrease as the spacing is increased. Therefore, the diagonal is dominant for small cylinders and large separation, and a point can be reached by increasing the relative amount of multiple scattering so that the diagonal is no longer dominant. This point corresponds to a fairly small amount of multiple scatter for the parameters considered.

Now, the actual problem to be dealt with is that of the random case. As the errors are seen to fluctuate as a function of object spacing, it is reasonable to expect that the average errors for the random array will be somewhat less than the maximum errors shown in figure 3.3 and 3.4. Therefore, with these points in mind, the following restrictions will be imposed:

$0.2\lambda < a < 0.5\lambda$, and average density $< 20\%$. Of course, very small value of $a/\lambda < 0.05$ will again be acceptable. These limits have been selected on the basis of using only the single scatter approximation. The higher order approximations would give smaller errors, but use too much computation time to be considered for the Monte-Carlo simulation.

3.3 Scattered Field Using Single Scatter Approximation

As the error in using the single scatter approximation has been ascertained, the field equations for the two dimensional problem equivalent to (2.133) for the three dimensional problem may now be determined from (2.114) and (3.17). The results are valid under the following restrictions.

1. Narrow beamwidth approximately 15°
2. Average separation about 2λ or larger
3. Object diameter about 1λ or smaller
4. Normal incidence backscatter

$$\begin{aligned}
 E^{\parallel} &= 1 + \frac{C}{\sqrt{kL}} \sum_{s=1}^{N_0} U_s g^{\parallel}(C_{a/s}) \sum_{n=0}^N (-1)^n A_n \cos n\beta_s \\
 E^{\perp} &= 1 + \frac{C}{\sqrt{kL}} \sum_{s=1}^{N_0} U_s g^{\perp}(C_{a/s}) \sum_{n=1}^N (-1)^n A_n \sin n\beta_s
 \end{aligned} \tag{3.21}$$

The above equations will be used for all statistical studies of the two dimensional rough surface.

4. RANDOM ARRAYS OF HEMICYLINDERS AND HEMISPHERES

The equations (2.91) and (3.21) derived in Chapters 2 and 3 may now be put to the use for which they were intended, namely the calculation of certain average properties of the electric field scattered from a rough surface. The so-called rough surface in this particular case consists of perfectly conducting hemicylinders or hemispheres situated on a perfectly conducting ground plane. The "roughness" is determined by the choice of the distribution of object coordinates, ρ_s . In Chapter 3, ρ_s was chosen such that the objects were located periodically. This situation is, in one sense rough because the surface so created is not flat. However, by rough, it is meant in this context, that at least one statistical moment other than the mean must be non-zero. Therefore the field statistics must be calculated by integration or by a Monte-Carlo method. The latter has been chosen for reasons already stated in the Introduction.

The essence of the particular Monte-Carlo technique to be used has already been outlined but the method is given here in more detail as follows.

1. Generate a set of coordinates, ρ_s .
2. Calculate the electric field from equation (2.91) or (3.21) as desired.
3. Keep a running total of statistical sums of the results of 2.
4. Repeat 1, 2, and 3 until enough configurations have been included to be reasonably representative of all configurations.
5. Take the final results from 3 and calculate the required statistics. These statistics may be used to determine when "enough" has been reached in 4. If not, 1, 2 and 3 may be repeated a number of additional times, and the results rechecked.

The usefulness of this method has already been discussed so now consider the implementation of the above sequence of events. Note that

step 2 has already been studied at length in the preceding chapters.

The first problem is that of determining the coordinate distribution $[\rho_s]$. A special distribution is developed here for finite scatterer separation with particular reference to the experimental problem.

With a suitable distribution chosen for the coordinates, steps 4 and 5 may be executed to find the field statistics. The remainder of this chapter is devoted to an investigation of the effects of the various parameters under the restrictions which have been imposed as a result of the study of the periodic problem.

4.1 Generation of Scatterer Coordinates

4.1.1 Uniform Distribution

The simplest method of obtaining the object locations is to use the continuous uniform distribution where all values of ρ_s in the unit interval $(-\frac{1}{2}, \frac{1}{2})$ are equally probable. This distribution will be used in most calculations for three reasons. First, this distribution may be obtained approximately from a digital computer in the form of a pseudo-random sequence. The statistical accuracy of such a sequence is discussed by Olsen³². Second, most theoretical calculations of the field statistics by the approximate integration method use this distribution. Third, it is a reasonable approximation to many practical problems. In this model the separation of the scatterers may take any value including those which make the objects overlap. The qualitative results may not be greatly affected by this, but it certainly does not completely represent a physical situation. Like the single scatter approximation it is useful in its simplicity provided that the density of scatterers is fairly low. (i.e. probability of overlaps is low).

4.1.2 Non-Uniform Distributions

There are situations which cannot be considered using the uniform

distribution, e.g. when attempting to construct a physical rough surface from a table of the coordinates. It is this problem, the construction of a laboratory surface for experiments, which prompts the development of a non-uniform distribution. Olsen³² has developed two methods for computing distribution functions which allow for finite dimensions of the scatterer.

One distribution of this type is formed by generating a set of coordinates using the continuous uniform random number generator RAND which is supplied with the IBM 360/67 computer. The distances between each pair of objects are calculated; any objects closer than a given value are rejected; then new coordinates for the rejected ones are calculated until all the minimum separation criteria are satisfied. These calculations are straight-forward when applied to a one dimensional array such as the coordinates for the hemicylinder problem and should give an accurate representation of a physical collection of finite scatterers. Note that a many-body distribution function of this type has only been determined numerically but never analytically.

There are three drawbacks inherent in the above method. The first is that many calculations and hence a relatively large calculation time is required to produce a set of coordinates. Also, the time increases sharply as the scatterers become more dense. The second is that the program itself becomes very complex when generating pairs of coordinates in a plane. Also too many numbers have to be remembered simultaneously. The third drawback is not an inherent problem, it is merely caused by the particular algorithm used by Olsen to calculate the distribution, and could therefore be remedied. Using this algorithm the Olsen distribution tends toward periodicity as the density is increased or the width of the empty regions is increased. Each single configuration must become periodic, of course, but each succeeding one should be different within the width of the empty region. Therefore, the Olsen distribution will give a smaller variance than one would expect from a truly

random surface.

The second distribution considered by Olsen³² has removed the computational problems noted above. This distribution provides the necessary minimum separation but cannot exactly represent a physical situation because the coordinates are allowed to attain only specific values. This method (see figure 4.1) consists of dividing the surface into square boxes, the width of which is the minimum allowed separation of the scatterers. The output of

×							
		×					×
×	×						×
			×	×			

Figure 4.1 Discrete Distribution of Scatterers

RAND is truncated to yield an integer between 1 and the number of boxes in a row (7 in figure 4.1). A pair of these integers is then used to place an object into the corresponding box. If there is already an object there, a new set of coordinates is calculated until an empty box is found. This distribution should be reasonably good for a low ratio of number of objects to number of boxes (25% shown in figure 4.1).

A distribution function that lies between the discrete and continuous methods outlined above and removes both the computational and theoretical disadvantages is now proposed. By increasing the number of discrete positions, it should be possible to approximate the desired continuous function as nearly as is required. The one problem associated with this

method is that the condition (full or empty) of each cell must be remembered. Therefore, as the number of cells is increased, an increasingly large amount of computer storage is required. Hopefully, then, a large number of cells will not be required.

This method is similar to the discrete Olsen method only now each cell is divided into a number of subcells, N_s , which gives a larger number of cells (and hence a larger number of discrete positions) per row (compare figure 4.2 where $N_s = 3$ with figure 4.1). In this case, a pair of cell coordinates are generated by RAND and then the required number of cells around the chosen one and the chosen cell itself are checked for the presence of an object. If there is no object detected, all these cells are set to full. The process is repeated until all the objects have a position.

For this distribution there is the added problem of determining N_s , which obviously must be kept as small as possible. N_s , like the antenna factor K , must be determined experimentally by increasing its value until the change in the field statistics is negligible.

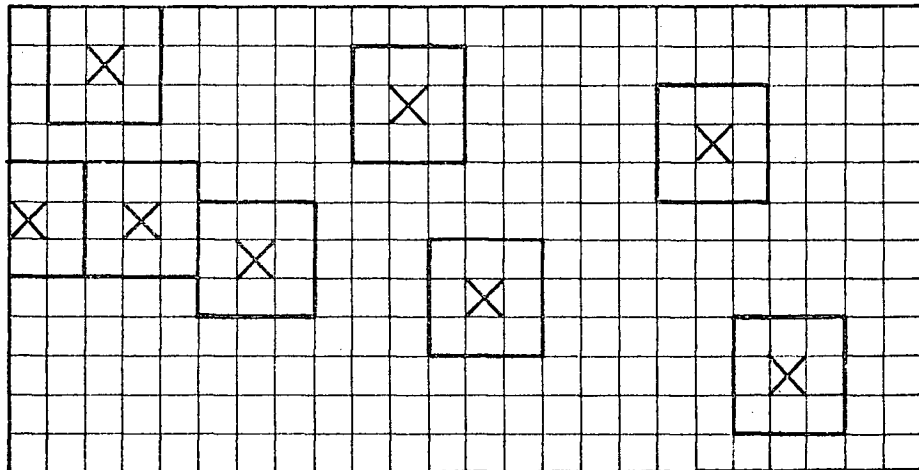


Figure 4.2 Modified Discrete Distribution of Scatterers

4.2 Calculation of Field Statistics

The remaining part of the Monte-Carlo technique is the actual calculation of the statistics from the collection of field values $[E_n]$. First of all, it must be decided upon which particular statistical functions should be considered. A thorough discussion of the properties of all the related statistical functions is given by Twersky¹⁷. The results presented here will primarily be concerned (for simplicity) with the first and second statistical moments only. Of course, higher order moments may be calculated as readily by this method, with only a small sacrifice in computational time and storage requirements. This is the great advantage of the Monte-Carlo method. Analytical methods become so complex that usually only the mean may be determined; even the calculation of the variance is extremely difficult.

A brief outline of the statistical parameters which will be used in conjunction with this particular problem may now be considered. Assume that N values of the complex electric field E_n have been calculated for N different configurations of the objects according to the desired distribution of coordinates. The functions required for the analysis of the mean and variance of the electric field for a rough surface are then:

$$\begin{aligned}
 \langle E_x \rangle &= \frac{1}{N} \sum_{n=1}^N \operatorname{Re}(E_n) \\
 \langle E_y \rangle &= \frac{1}{N} \sum_{n=1}^N \operatorname{Im}(E_n) \\
 \langle E_x^2 \rangle &= \frac{1}{N} \sum_{n=1}^N \left\{ \operatorname{Re}(E_n) \right\}^2 \\
 \langle E_y^2 \rangle &= \frac{1}{N} \sum_{n=1}^N \left\{ \operatorname{Im}(E_n) \right\}^2 \\
 \langle E_x E_y \rangle &= \frac{1}{N} \sum_{n=1}^N \operatorname{Re}(E_n) \operatorname{Im}(E_n)
 \end{aligned} \tag{4.1}$$

The set of numbers calculated according to equations (4.1) are the five basic outputs of the Monte-Carlo portion of the analysis. From these numbers, the desired statistical results may be derived. Note that there will be additional sums of higher order products if higher statistical moments are required.

The means of the real and imaginary parts of the field are useful as given above in the first two equations of (4.1). However, the usual functions which are considered are the so called "coherent intensity" and "coherent phase".

$$C^2 = \langle E_x \rangle^2 + \langle E_y \rangle^2 \quad (4.2)$$

$$\alpha = \tan^{-1} \frac{\langle E_y \rangle}{\langle E_x \rangle}$$

The variance of the real and imaginary parts of the field may be calculated from

$$\begin{aligned} \sigma_x^2 &= \frac{1}{N} \sum \left\{ \text{Re}(E_n) - \langle E_x \rangle \right\}^2 \\ &= \langle E_x^2 \rangle - \langle E_x \rangle^2 \end{aligned} \quad (4.3)$$

$$\sigma_y^2 = \langle E_y^2 \rangle - \langle E_y \rangle^2$$

Here, the usual function to be considered is the "incoherent intensity".

$$\langle I^2 \rangle = \sigma_x^2 + \sigma_y^2 \quad (4.4)$$

Finally, the co-variance and correlation coefficient may be determined from

$$\sigma_{xy} = \langle E_x E_y \rangle - \langle E_x \rangle \langle E_y \rangle \quad (4.5)$$

$$\rho = \frac{\sigma_{xy}}{\sigma_x \sigma_y}$$

The accuracy of the means may readily be calculated.³² These estimates should give a sufficient indication when enough samples have been used in the Monte-Carlo calculation. That is, the results may be checked after a certain number of samples have been processed, and then more samples may be taken. The size of the error will also give a good estimate of how many more samples are required. These errors of the means are:

$$\begin{aligned}\Delta\langle E_x \rangle &= 2\sqrt{\frac{\sigma_x^2}{N-1}} \\ \Delta\langle E_y \rangle &= 2\sqrt{\frac{\sigma_y^2}{N-1}}\end{aligned}\tag{4.6}$$

The above calculations will give the desired means and variances for any complex function E of the random variables X_1, X_2, \dots, X_N for any distribution of the X_n . These calculations must be adhered to unless the field equations and distribution function for the s^{th} object are functions of the s^{th} coordinate only (e.g. single scatter approximation with continuous uniform distribution). For this case the means may be calculated exactly and the variances calculated approximately with a considerable saving of computational effort. These special calculations are given in Appendix D. The main advantage of this method is that the density, ρ , appears after the Monte-Carlo operations have been completed. The disadvantages are its limited application and limited results. This method is only used as a comparison with the Monte-Carlo simulation.

4.3 Determination of Active Scattering Area

The value of $K = 1.5$ for the ratio of the effective surface width to the width of the area illuminated by the main beam of the antenna (see equation 2.97) was checked by performing the same experiment as in section 3.2.1 for the periodic surface, upon the random surface.

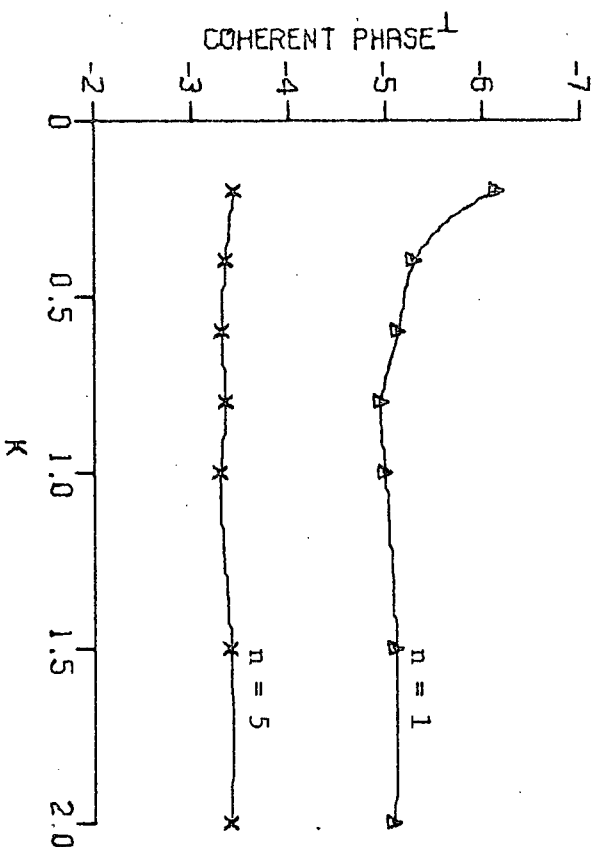
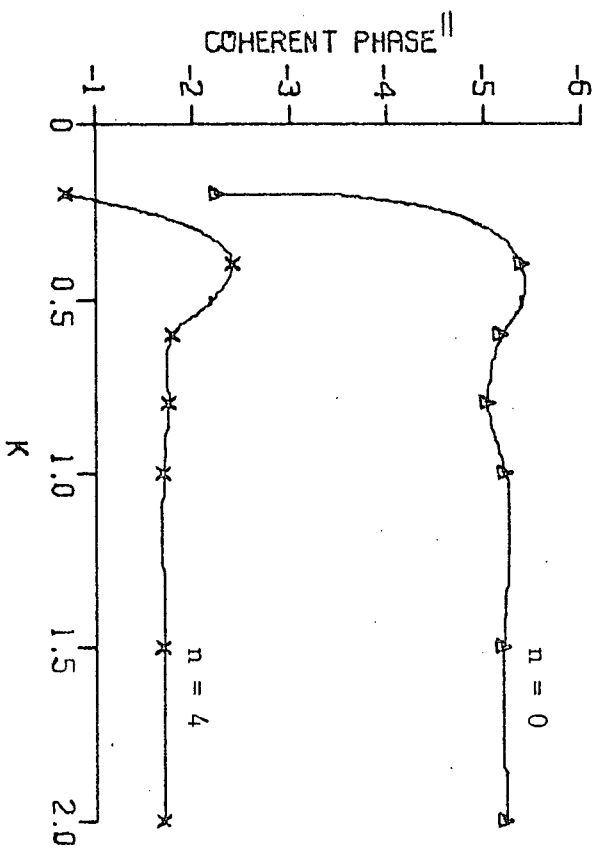
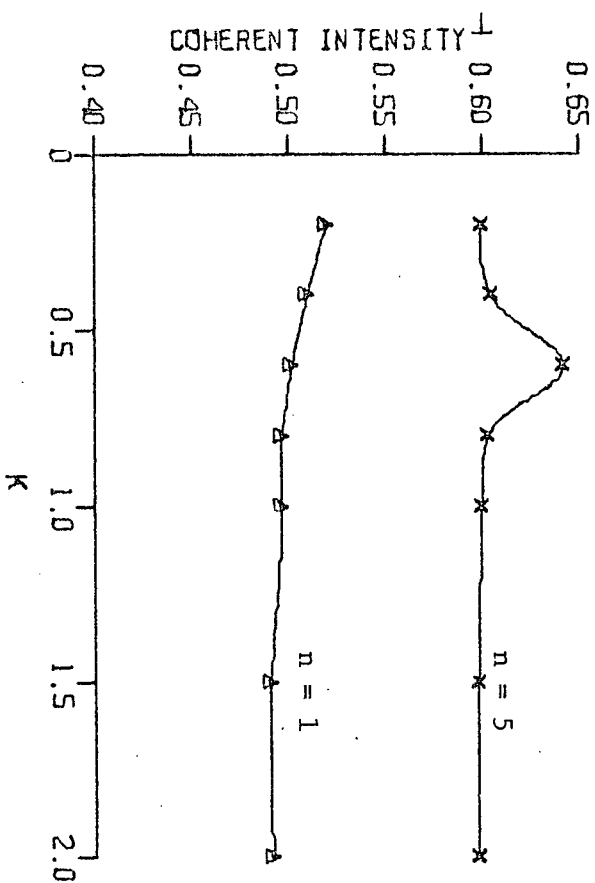
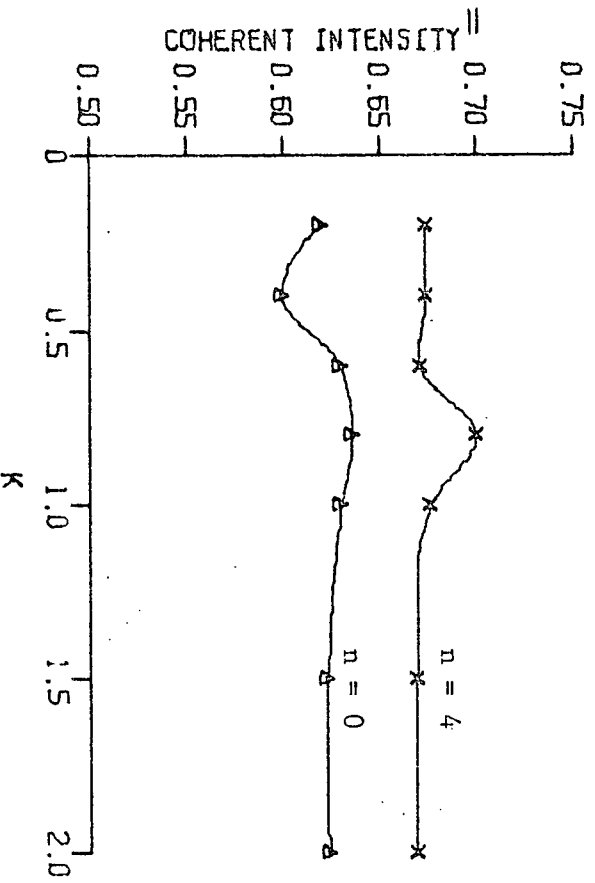


Figure 4.3 The Determination of Active Beamwidth - Coherent Field.

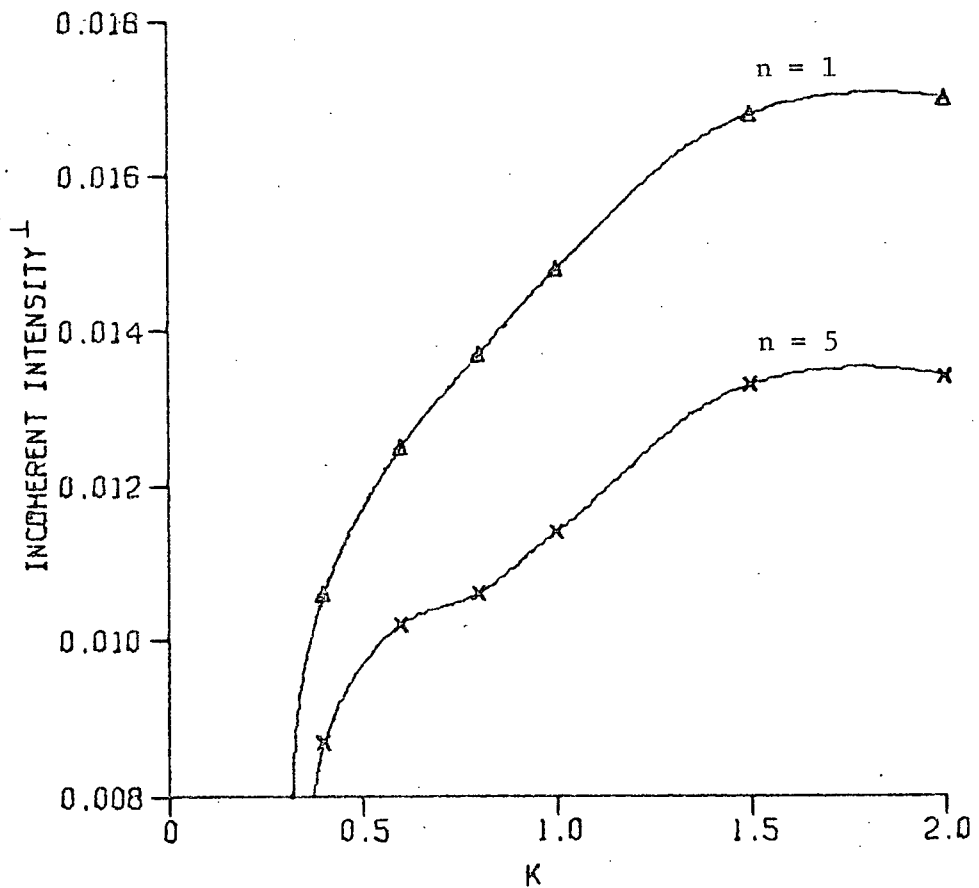
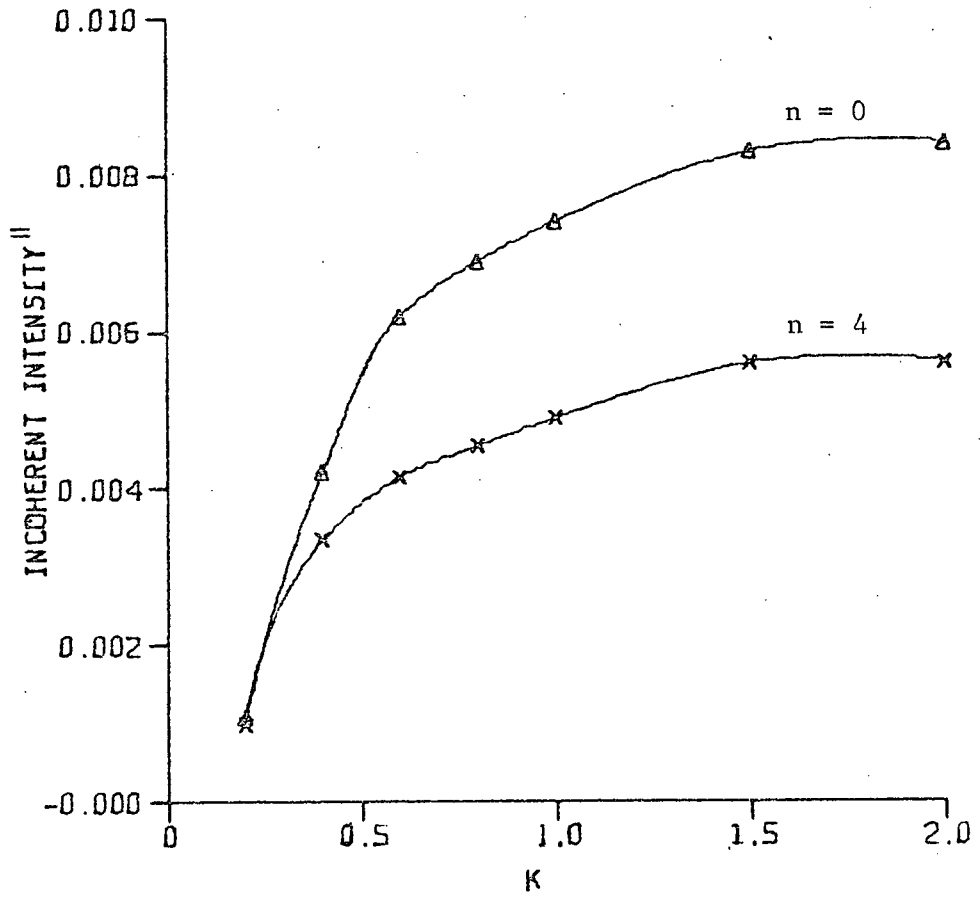


Figure 4.4 The Determination of Active Beamwidth - Incoherent Field.

In this case, the beam sharpness factor, n , was varied also.

As a finite number of objects are being considered, the density must take on only discrete values. So that all the results could be referred to one fixed density, two sets of data were calculated, one above and one below $\rho = 0.25$. The results were then linearly interpolated to $\rho = 0.25$ and are shown as functions of K in figures 4.3 and 4.4.

From figure 4.3 it can be clearly seen that the value $K = 1$ is sufficient, even for the case of large sidelobes ($n = 0$), to determine the coherent field. However, from figure 4.4 it appears that $K = 1.5$ would be preferable for calculation of the incoherent intensity. On closer inspection of the curves of figure 4.4 it can be seen that the curves are functions of K for $1.0 \leq K \leq 1.5$ but not of n . This fact may be interpreted as indicating that the effect of the sidelobes is negligible. Perhaps this variation with K appears because the main beam is seeing only a portion of the distribution of objects and hence slightly different surface statistics. Thus, in cases where it is necessary to restrict the number of objects for computational reasons, $K = 1.0$ will be used. In most cases, however, the value $K = 1.5$ (which agrees with the periodic array results) will be retained.

4.4 Comparison of Results

Two sets of functions are available with which to compare the Monte-Carlo simulation. The first of these is the Twersky results¹⁵ for the coherent and incoherent field scattered by the hemicylinder problem for a continuous uniform distribution and infinite plane wave incidence. The second functions are given in Appendix E and are obtained by approximate integration of the field equations derived in Chapter 2. These functions are for the continuous uniform distribution but include finite beam incidence. All methods are based upon the single scatter approximation.

4.4.1 Coherent Field

The Twersky coherent field¹⁵ is given by

$$\langle E_p \rangle = 1 + \rho' f_p \quad (4.7)$$

where

$$f_p^{\parallel, \perp} = \frac{1}{4} \pi \sum_{n=0}^{\infty} A_n^{\parallel, \perp} \quad (4.8)$$

and

$$\begin{aligned} \rho' &= \left(\frac{\rho \lambda}{2a} \right) \\ &= N_o \frac{\lambda}{W} \end{aligned} \quad (4.9)$$

is the number of active scatters per wavelength.

The function modified for finite beamwidth given in Appendix E is

$$\langle E_b \rangle = 1 + \rho' f_b \quad (4.10)$$

where

$$f_b = f_p \left\{ 1 - 2 \left[\frac{iB}{kL} + \frac{1}{C_a \sqrt{2kL}} (1 - BC_a^2) e^{i \frac{1}{4} \pi (1 + kLC_a^2)} \right] \right\} \quad (4.11)$$

and

$$\begin{aligned} B^{\parallel} &\approx \frac{1350}{\theta_e^2} \\ B^{\perp} &\approx \frac{1526.8}{\theta_h^2} \end{aligned} \quad (4.12)$$

As the above functions, (4.7) and (4.10) are explicit functions of the density, ρ' , and are both in the same form, it is easiest to compare only f_b and f_p independently of ρ' . However, for the Monte-Carlo results the function

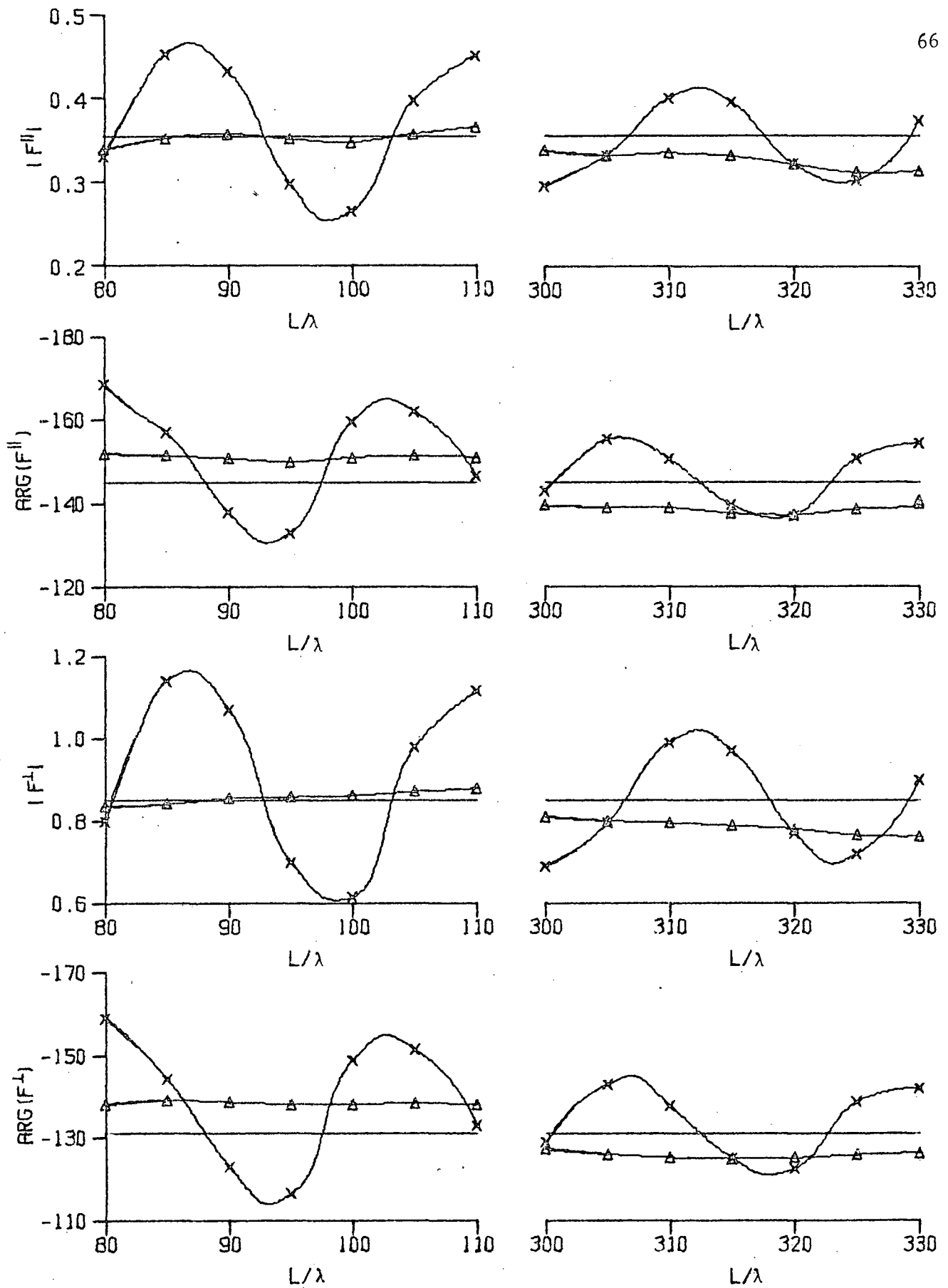


Figure 4.5 A Comparison of Three Methods for Calculating the Single Scattered Coherent Field for an Array of Hemicylinders with $\rho = 2\%$ and $a = 0.2\lambda$:

- (a) Twersky —————
- (b) Monte Carlo —△—△—
- (c) Approximate Integration —x—x—

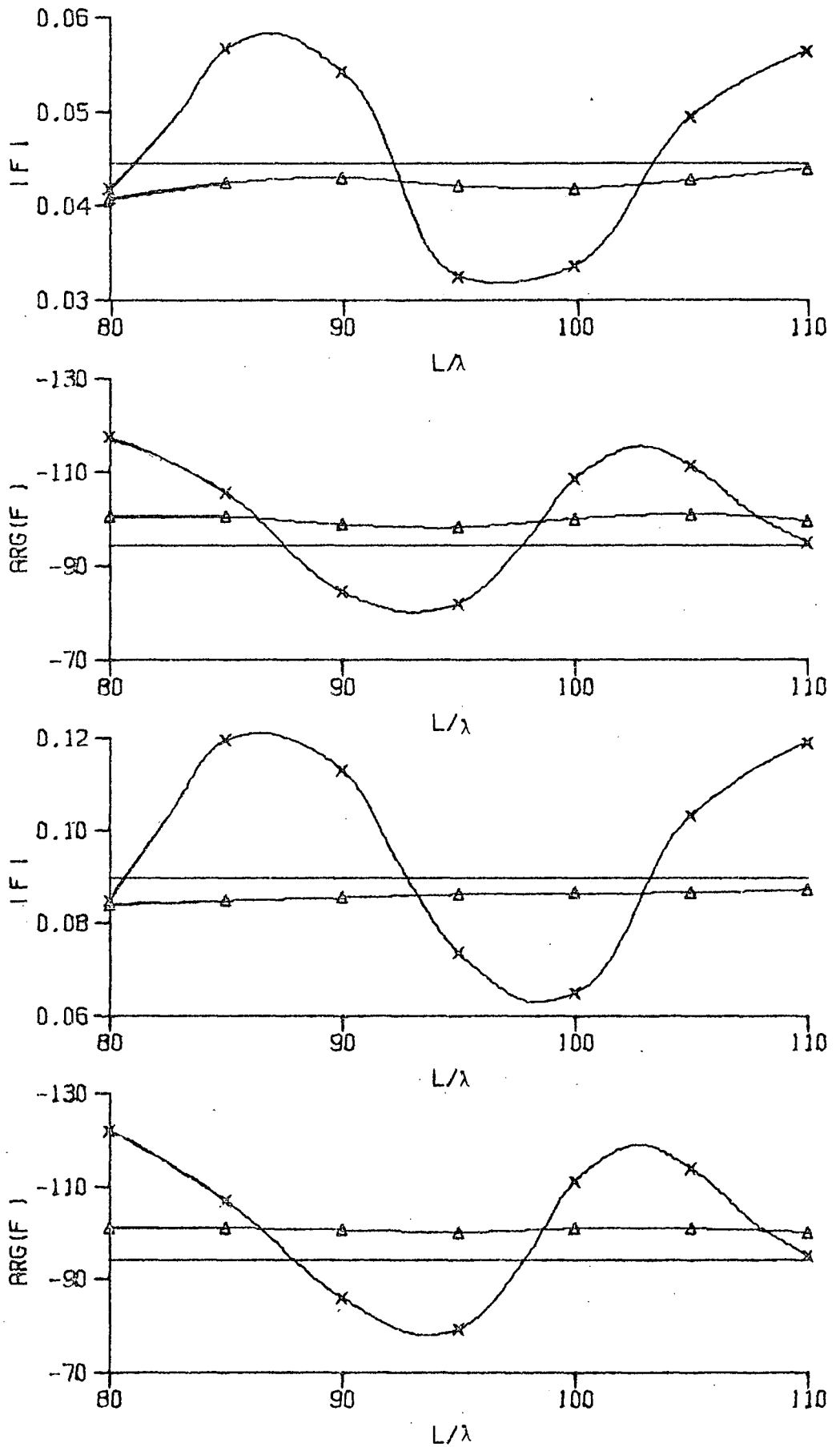


Figure 4.6 A Comparison of Three Methods for Calculating the Single Scattered Coherent Field for an Array of Hemicylinders with $\rho=2\%$ and $a=0.05\lambda$.

- (a) Twersky ———
- (b) Monte Carlo —△—△—
- (c) Approximate Integration —×—×—

$$f_{MC} = \frac{1}{\rho'} \left\{ \langle E \rangle - 1 \right\} \quad (4.13)$$

must be calculated for every value of ρ' .

f_b , f_p , and f_{MC} are shown in figure 4.5 as functions of the antenna to surface distance L/λ for a density, ρ , of 2% and object radius, a , of 0.2λ . The same functions are given in figure 4.6 for $a = 0.05\lambda$. From figure 4.5 the following results are evident:

1. The Monte-Carlo method is the best method for calculating the coherent intensity. At least, for the parameter values chosen, the analytic solution is too much in error.
2. The analytic method gives qualitatively the form of the curves, but their variation is too large.
3. The approximate analytic solution becomes better as the antenna to surface distance is increased.
4. The results for finite beam incidence are fairly close to the plane wave results even for the narrow beamwidth used here.

From figures 4.5 and 4.6 it can be seen that the accuracy of the methods is independent of the object radius. This fact verifies the result found in Appendix E that it is permissible to set $\beta_s = \frac{1}{2}\pi$ in the field equations. Thus, the use of this assumption (see equation (2.80)) for the three dimensional case is indeed reasonable.

4.4.2 Incoherent Intensity

The Twersky plane wave incoherent intensity¹⁵ is given by

$$\begin{aligned} \langle I_p^2 \rangle &= 1 - c_p^2 \\ &= \rho' \left[\langle I_{p_0}^2 \rangle - \rho' |f_p|^2 \right] \end{aligned} \quad (4.15)$$

where

$$\langle I_{p_0}^2 \rangle = -2\text{Re}(f_p) \quad (4.16)$$

which is derived by assuming that all the incoherent power is in the backscatter direction only.

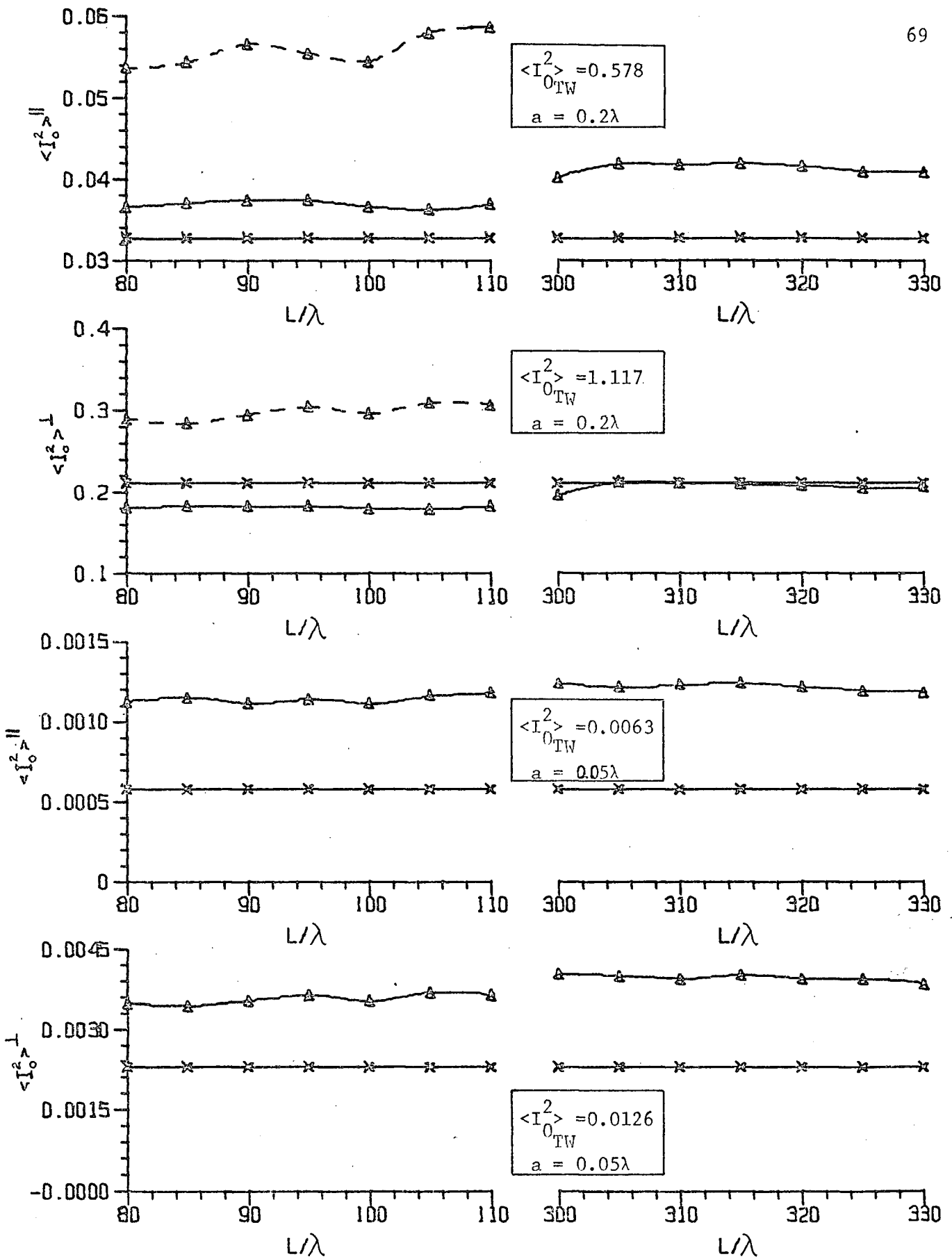


Figure 4.7 A Comparison of Three Methods of Calculating the Single Scattered Incoherent Intensity for an Array of Hemicylinders.

(a) Monte Carlo: $\rho=2\%$ \triangle $\rho=10\%$ $-\triangle-$

(b) Approximate Integration \times

(c) Twersky results are constants as indicated on each graph. The values are too large to plot.

The finite beamwidth modified function is derived in Appendix E as

$$\langle I_b^2 \rangle = \rho' \left[\langle I_{b_0}^2 \rangle - \rho' |f_b|^2 \right] \quad (4.17)$$

where

$$\langle I_{b_0}^2 \rangle^{\parallel} \approx |f_p^{\parallel}|^2 \frac{2\pi\theta_e}{90} \left[1 - \frac{2}{\pi b c_a} \right] \quad (4.18)$$

$$\langle I_{b_0}^2 \rangle^{\perp} \approx |f_p^{\perp}|^2 \frac{\pi^2 \theta_h}{270}$$

Again, the Monte-Carlo results may be put into the same form

$$I_{MC}^2 = \rho' \left[\langle I_{MC_0}^2 \rangle - \rho' |f_{MC}|^2 \right] \quad (4.19)$$

so that

$$\langle I_{MC_0}^2 \rangle = \frac{1}{\rho'} \left[\langle I_{MC}^2 \rangle + | \langle E_{MC} \rangle - 1 |^2 \right] \quad (4.20)$$

The behaviour of f_b , f_p , and f_{MC} has already been discussed so now it is necessary only to compare $\langle I_p^2 \rangle$, $\langle I_{b_0}^2 \rangle$, and $\langle I_{MC_0}^2 \rangle$ to determine the behaviour of the incoherent intensity. These functions are shown in Figure 4.7 for the same parameter values as the coherent intensity.

From 4.7 it is clear that:

1. The Twersky model gives far too large an incoherent intensity, and therefore the assumption that most power is scattered into the backscatter direction is not valid at least for this range of parameters.
2. The Twersky results are better for smaller diameter objects.
3. The analytic method ignores the fine variations due to changes in L/λ , but gives a reasonably good result, especially for low densities.
4. The analytic and Monte-Carlo results agree more closely for a lower number of objects.

4.5 Summary

In summary, then, it has been found that the Monte-Carlo method as implemented in this chapter is a useful method for calculating the mean and variance of the field scattered from the discrete scatterer model of a rough surface. The Monte-Carlo method also allows the use of the same distributions of object coordinates to be used for both computer simulations and physical experiments. The actual distribution function to be used has been developed, and will be studied in detail in the next chapter.

The analytic solution has the advantage of being simple to calculate numerically but gives large errors in some cases. In fact, the plane wave solution is better than the analytic solution for the coherent intensity while the opposite is true for the incoherent intensity. Thus, a good estimate of the behaviour of the scattered field may be obtained by using a combination of the plane wave and analytic beam solutions. That is,

$$\begin{aligned}
 c^2 &\approx \left| 1 + \rho' f_p \right|^2 \\
 \alpha &\approx \arg(1 + \rho' f_p) \\
 \langle I^2 \rangle &\approx \rho \left| f_p \right|^2 \left(F^{\parallel, \perp} - \rho' \right)
 \end{aligned} \tag{4.21}$$

with $F^{\parallel, \perp}$ given by equation (E. 44).

For the three dimensional problem, the Monte-Carlo method remains the only useful means of numerical analysis.

5. CONSTRUCTION OF A LABORATORY SURFACE AND THE MEASUREMENT OF ITS SCATTERED FIELD

Perhaps the most accurate method for determining the field statistics is the direct measurement of the field scattered from a sufficiently large number of independent ensembles of scatterers which are illuminated by a real antenna. This experimental investigation is attractive because of the inherent freedom from mathematical approximations (such as the single scatter approximation).

On the other hand, there are two main disadvantages to the experimental approach. The first arises from the difficulty of adjusting the system parameters to exact values, that is the system must have close mechanical tolerances and stability. The second is the inherent inflexibility of the system. The variation of most parameters requires the construction of a new part of the system.

These disadvantages are outweighed, however, by two features which are difficult, if not impossible, to implement in the computer simulation. First, object shapes other than hemicylinders or hemispheres may be considered with little extra effort. Second, a distribution of sizes as well as locations of objects may be used. Although these features will not be utilized in this study, their application is immediate and therefore provides impetus for the development of a workable experimental system.

5.1 Design of the Experimental System

For the design of the experiment, four major problems must be considered. The first is the choice of suitable parameters so that the greatest amount of information can be obtained for the simplest and least number of changes in the experimental set-up.

The second is the method of construction of a specific rough surface. The third is the method of measurement and data collection. The final problem is the method of analysis of the data itself.

5.1.1 Parameter Values

For the experimental problem, the selection of suitable parameter values is limited mainly by the dimensional constraints of the experimental set-up and the computation time limitations of the corresponding Monte-Carlo simulation.

The wavelength was chosen in the 8 millimeter range to keep all the physical dimensions of the experiment reasonably small. For example, at 3 cm. wavelengths, the dimensions of a single surface would be too large, while at 4 mm. wavelengths, the mechanical tolerances (to a fraction of a wavelength) could become a problem.

The simulation time is a function of the number of objects so it is necessary to work with as few scatterers as possible. This implies that their size/wavelength should be large, their density low, the antenna close to the surface, and the beamwidth narrow. In terms of the approximations used in the simulation, the narrow beamwidth and low density are desirable while the large size of scatterers and small antenna to surface distance are undesirable.

The upper bound of the object size, then, is limited by the single scatter approximation, while the lower bound is determined from the limited number of objects. These considerations give a useful range for the object radius of

$$0.3 \leq \frac{a}{\lambda} \leq 0.5 \quad (5.1)$$

The upper limit was chosen for this experiment to yield as large an amount

of incoherent scattering as possible. Therefore, at 8 mm.,

$$\begin{aligned} a &= \lambda/2 \\ &= .169 \text{ in.} \end{aligned} \tag{5.2}$$

The antenna-surface distance is limited by the requirement that the surface lie in the far field of the antenna. That is⁴

$$L > \frac{D^2}{\lambda} \tag{5.3}$$

where D is the width of the radiating aperture. For the horn used in figure 2.5 and at a frequency of 35.0 GHz.,

$$\begin{aligned} L &\geq \left(\frac{7.62}{.851}\right)^2 \\ &\geq 79\lambda \end{aligned} \tag{5.4}$$

Therefore, choose

$$\begin{aligned} L &= 80\lambda \\ &\approx 27 \text{ in.} \end{aligned} \tag{5.5}$$

Actually,⁴ twice the above value is to be preferred to be absolutely certain that the surface is in the far field of the antenna, but (5.5) must be used to keep the illuminated surface area as small as possible.

The laboratory antenna has a fixed beamwidth of

$$\theta_o = 8^\circ \tag{5.6}$$

which will also be used for the simulation.

Some parameters in this experiment can be varied without too much effort. The most readily variable parameter is the frequency, which may be varied from 32 to 38 GHz. for the particular generators used. The

other easily variable parameter is the object density. As the density is to be kept low, a good starting value is chosen to be

$$\rho \approx 5\% \quad (5.7)$$

5.1.2 Method Of Measurement

The problem of experimentally measuring the statistics of the field scattered from a rough surface proceeds as follows:

1. Construct a rough surface sufficiently larger than the area illuminated by the main beam of the antenna.
2. Place the surface in the beam at a certain position.
3. Measure the scattered field from this surface.
4. Measure the scattered field from a flat surface at the same position.
5. Normalize the field (3) by the field (4).
6. Repeat steps (1) to (5) keeping all parameters fixed for a large number of independent surfaces (1).

As such a large number of independent surfaces are required, it was decided to reduce the manual labour by constructing a surface which was several beamwidths in area. By this method, several independent samples may be obtained from one surface. This surface may then be moved continuously past the antenna to give a continuous scattered field as a function of position. The maximum number of independent samples may then be selected by some method from this continuous set of data. This method was implemented using the transverse positioner and anechoic chamber developed by Olsen³² for his scattering investigations.

This scanning method has one disadvantage, however. It is difficult to construct a surface where the ground plane portion is flat over as large an area as is required for a large number of samples. It is also hard to adjust the positioning of the surface on the scanner such that the

ground plane is always the same distance from, and in the same orientation with respect to the antenna. These errors can easily introduce phase errors of the order of 2 radians at 8 mm. wavelengths.

The solution to this problem was to devise a system which tends to cancel the phase errors. The system used for this experiment is shown in figure 5.1. The direction of motion of the surface is normal to the page. Here,

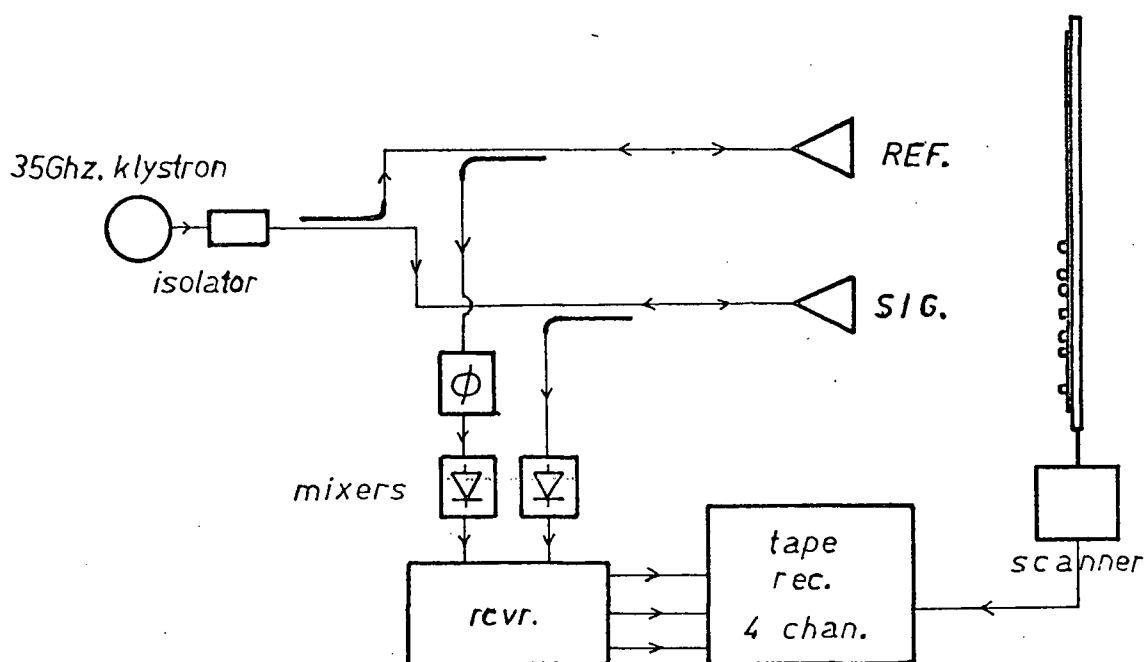


Figure 5.1 Experimental System

the surface is covered with the distribution of hemispheres in the lower half, while the upper half remains flat. A reference signal is obtained from the upper antenna, while the actual scattered signal from the rough surface is obtained from the lower antenna. The division of the rough surface signal by the flat surface signal should then give the normalized scattered field. The remaining errors are now due only to tilting of the surface as it is moved. Every effort was made to mount the surface so that these errors were kept to a minimum.

The reference signal is then fed to the reference channel of the

Scientific Atlantic Model 1751, #8 phase-lock receiver while the random signal is sent to the signal channel. The three outputs (signal phase - reference phase, reference magnitude, and phase magnitude) are recorded on an Ampex Model SP - 300 F.M. tape recorder for later analysis. Before any measurements can be taken, an absolute reference must be established since the gain and phase shifts will not necessarily be the same over the signal channel and the reference channel. This reference is obtained by placing a flat metal plate against the rough surface and parallel to it as in figure 5.2. The slight variation in position between the flat surface and the actual one under it should not noticeably affect the magnitude, and the phase shift will cancel due to the measurement method. The system gain controls and phase shifts could now be set to give a

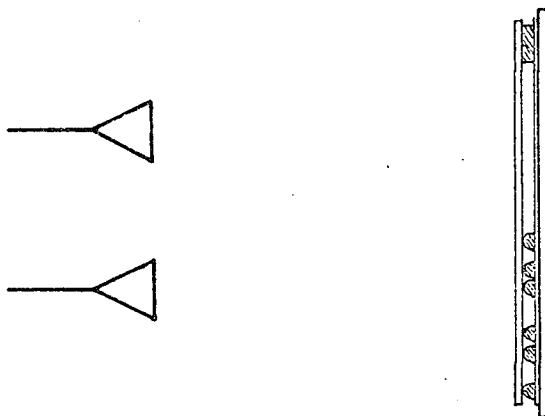


Figure 5.2 Reference Plate for Normalization

reading of 1 (0 db) on the magnitude channels and 0 on the phase channel. It is more convenient, however, to merely record the actual readings on the three channels, and then record the subsequent data from the rough surface without altering the controls. The data can then be normalized later at the time of processing (see section 5.4.1).

5.1.3 Construction of the Surface

The material chosen for the surface was .05 in. thick soft annealed aluminum. Ordinary aluminum and soft copper sheet were tried, but these materials were not ductile enough. The hemispheres were then formed in the sheet at the appropriate locations using a punch and die as shown in figure 5.5.

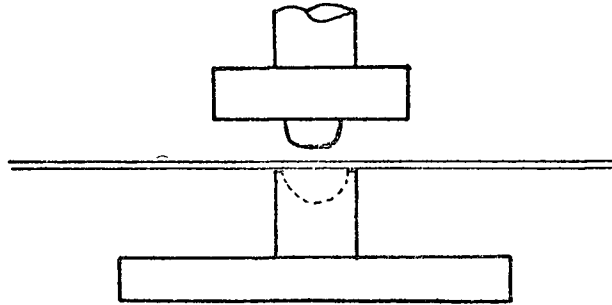


Figure 5.3 Forming a Hemispherical Scatterer in Aluminum Sheet

The die was machined to be a perfect hemisphere of the desired radius, but the shape of the punch had to be carefully determined by trial and error. The main problems encountered were tearing of the metal and pointed "hemispheres".

The distribution of scatterer positions was generated by the algorithm developed in Chapter 4 for the discrete distribution of finite-separation scatterers. As the method was programmed on the IBM 360/67 digital computer, it was advantageous to use the Calcomp digital plotter to obtain a direct plot of the object positions for each surface. Part of a scaled down output is shown in figure 5.4.

The coordinates were plotted in real size so that the computer output could be fastened directly to the aluminum sheet. The object locations were then transferred to the metal surface with an automatic centre punch.

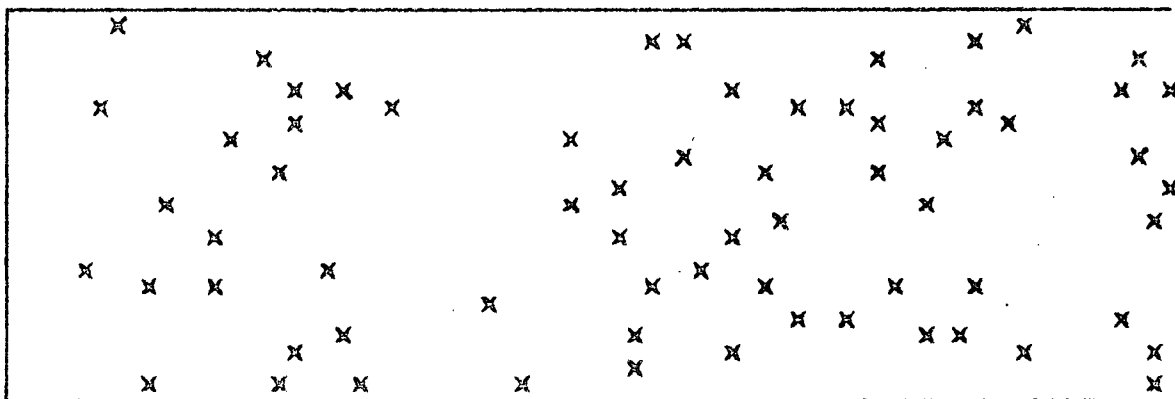


Figure 5.4 Computer Generated Hemisphere Coordinates

5.2 Simulation Test of the Surface Distribution

Recall at this point (see section 4.1.2) that there are two main parameters which characterize the distribution function developed for use in the experimental study. These parameters are the minimum separation, d_{\min} , and the number of subdivisions of the basic cell, N_s . The limiting effect of these parameters is shown in figure 5.5. Obviously, N_s should be as large as possible and d_{\min} as small as possible to allow

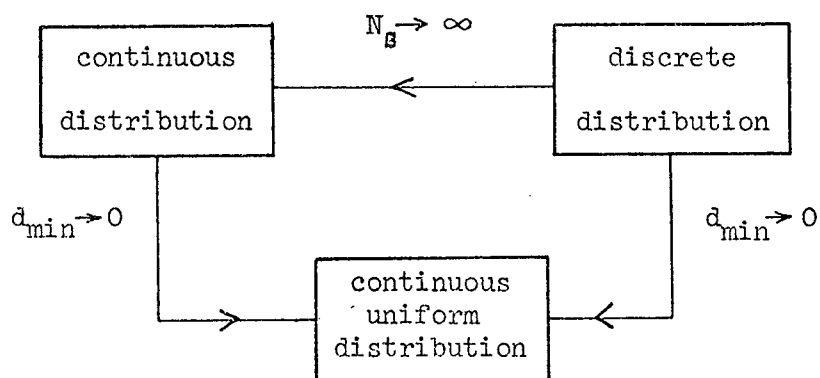


Figure 5.5 Effect of Distribution Parameters

comparison to be made with the continuous uniform distribution (ideal case).

5.2.1 Determination of Minimum Grid Subdivision

The coordinate distribution function of section 4.1.2 may now be investigated by the Monte-Carlo simulation to determine the minimum value of N_s , the number of cell subdivisions required to approximate a continuous distribution. The minimum value is used, of course, to minimize the computation time. As the same parameter values should be used as for the experiment, this problem was not discussed earlier in Chapter 4.

Figure 5.6 shows the coherent intensity, C^2 , the coherent phase, α , and the incoherent intensity, $\langle I^2 \rangle$ as a function of N_s for densities of 2.5%, 5%, and 10%. The minimum separation has been conveniently chosen to be 0.5 in. or 1.48λ at 35.0 GHz. This is about the minimum separation that can be mechanically formed because of the finite dimensions of the walls of the die. These curves (figure 5.6) indicate that $N_s = 3$ is sufficient for densities of 10% while $N_s = 2$ is sufficient for lower densities. In the interest of minimizing computation time, the value of $N_s = 2$ was selected as sufficiently large for the purposes of this experiment.

Note that the coherent phase is the quantity most sensitive to changes in N_s and shows some variation even for a density as low as 2.5%. This increase of the coherent phase with increasing N_s shows that the surface actually becomes "rougher" even though it can be seen that the incoherent intensity is decreasing. The reason for this effect is that the increased roughness causes more power to be scattered into other directions instead of increasing the fluctuations in the specular direction.

5.2.2 Effect of Minimum Separation

The other distribution parameter, d_{\min} , may now be investigated, although the value of $d_{\min} = 1.48\lambda$ has already been selected. Figure 5.7 shows the coherent intensity, coherent phase, and incoherent intensity as

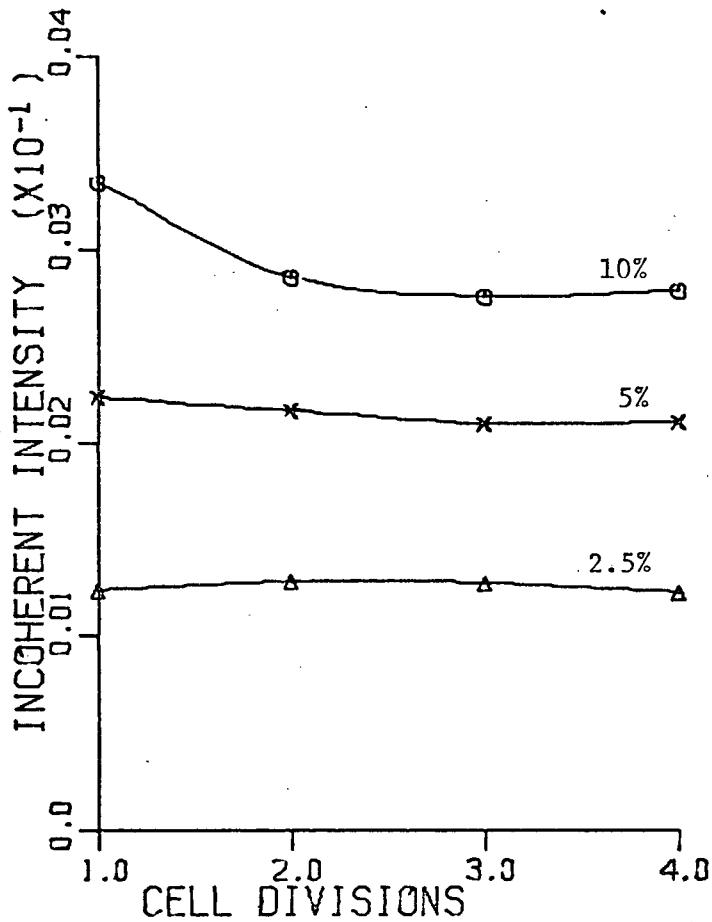
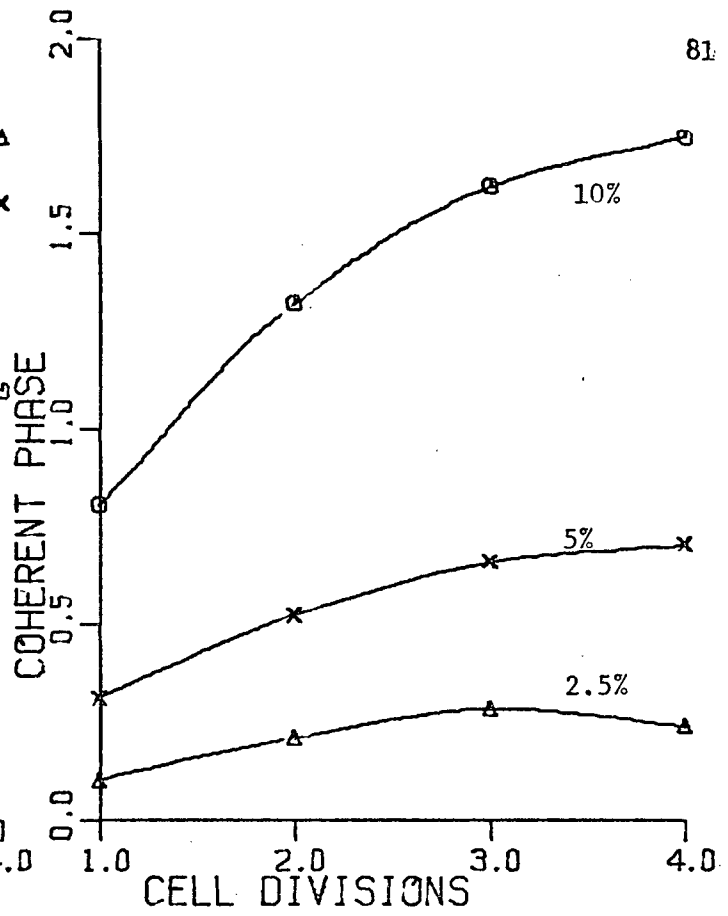
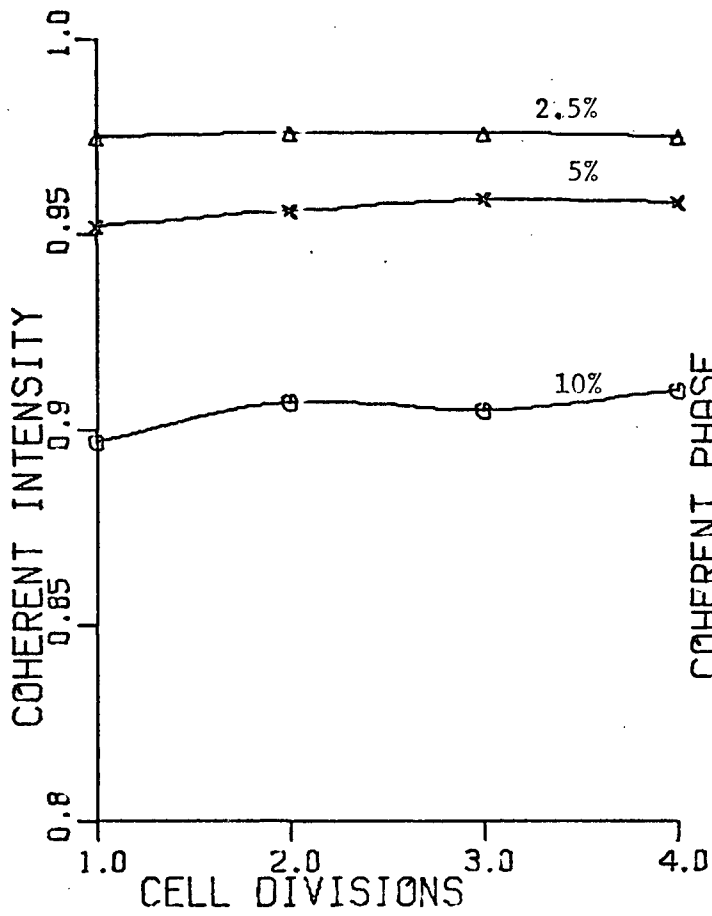


Figure 5.6 Scattered Field Statistics as a Function of N_s for Various Densities of Hemispheres.

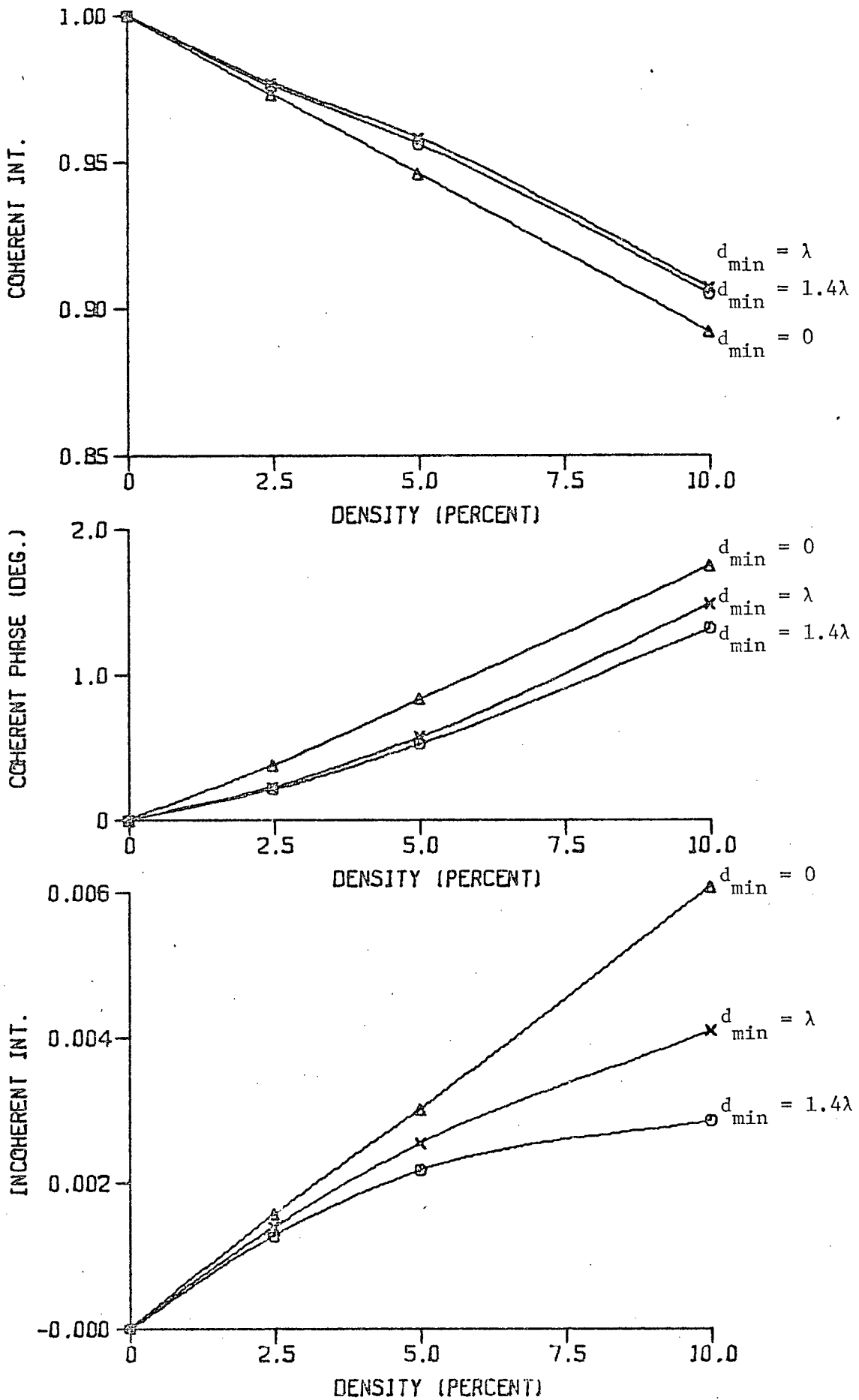


Figure 5.7 Scattered Field Statistics vs. Density of Hemispheres for Various Separations.

a function of density for a minimum separation of 0, 1, and 1.48 wavelengths for $N_s=2$. For a density of 5% (the value chosen for the experiment) the variation over the range of d_{\min} can be seen to be relatively slight.

In this case, the surface is actually becoming **more** periodic as d_{\min} is increased. This fact is illustrated by the decrease in coherent intensity. Obviously, the coherent field will approach some limiting value < 1 since even the periodic surface is rough to the extent that it will scatter power into directions other than the specular one.

5.2.3 Probability Density of Coordinates

A more direct check upon the behaviour of the distribution function may be obtained by numerically calculating the probability density of the normalized polar coordinates of the scatterers as a histogram. Polar coordinates are used to minimize problems in calculating the histograms due to an accidental correlation between the discrete divisions of the distribution function and the discrete "boxes" of the histogram. The radial coordinate is that given by equation (2.118), that is

$$r = \sqrt{\rho_{x_s}^2 + \rho_{y_s}^2} \quad (5.8)$$

while the angular coordinate is given by

$$\theta = \frac{1}{\pi} \tan^{-1} \frac{\rho_{y_s}}{\rho_{x_s}} \quad (5.9)$$

The individual coordinates are sorted into 25 discrete ranges for 500 independent samples of the surface. On the average there are about 15 scatterers per surface giving about 7500 coordinate values per graph. Figures 5.8 - 5.10 show the probability density histograms for an object density of 5% with $N_s = 1, 2, \text{ and } 3$ respectively. Figures 5.11 - 5.13 show the same functions for an object density of 10%. The continuous straight lines on the graphs indicate an ideal continuous uniform distribution.

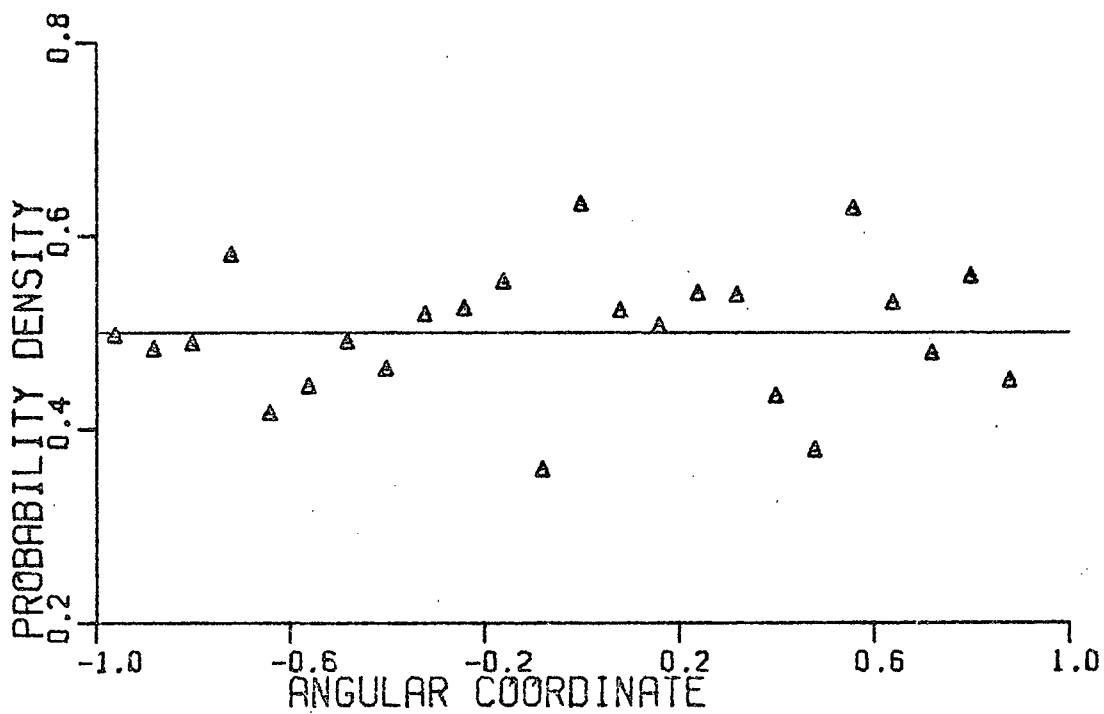
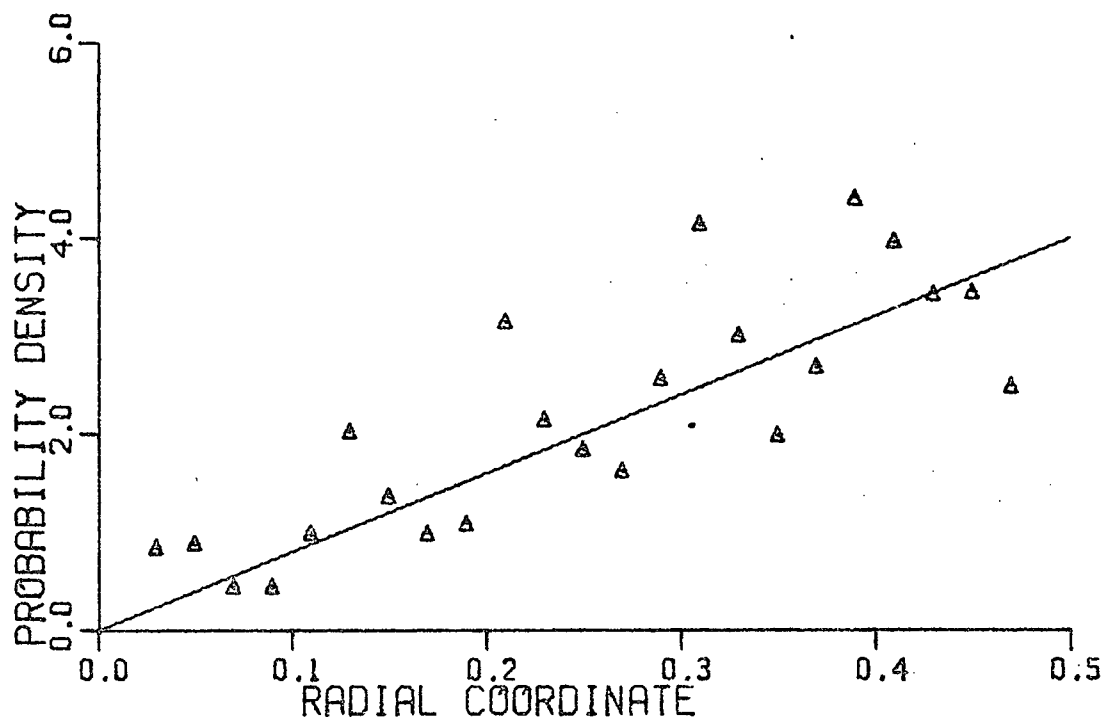


figure 5.8 Probability Density of Hemisphere Coordinates for an Object Density of 5% and 500 Sample Surfaces, $N_s = 1$.

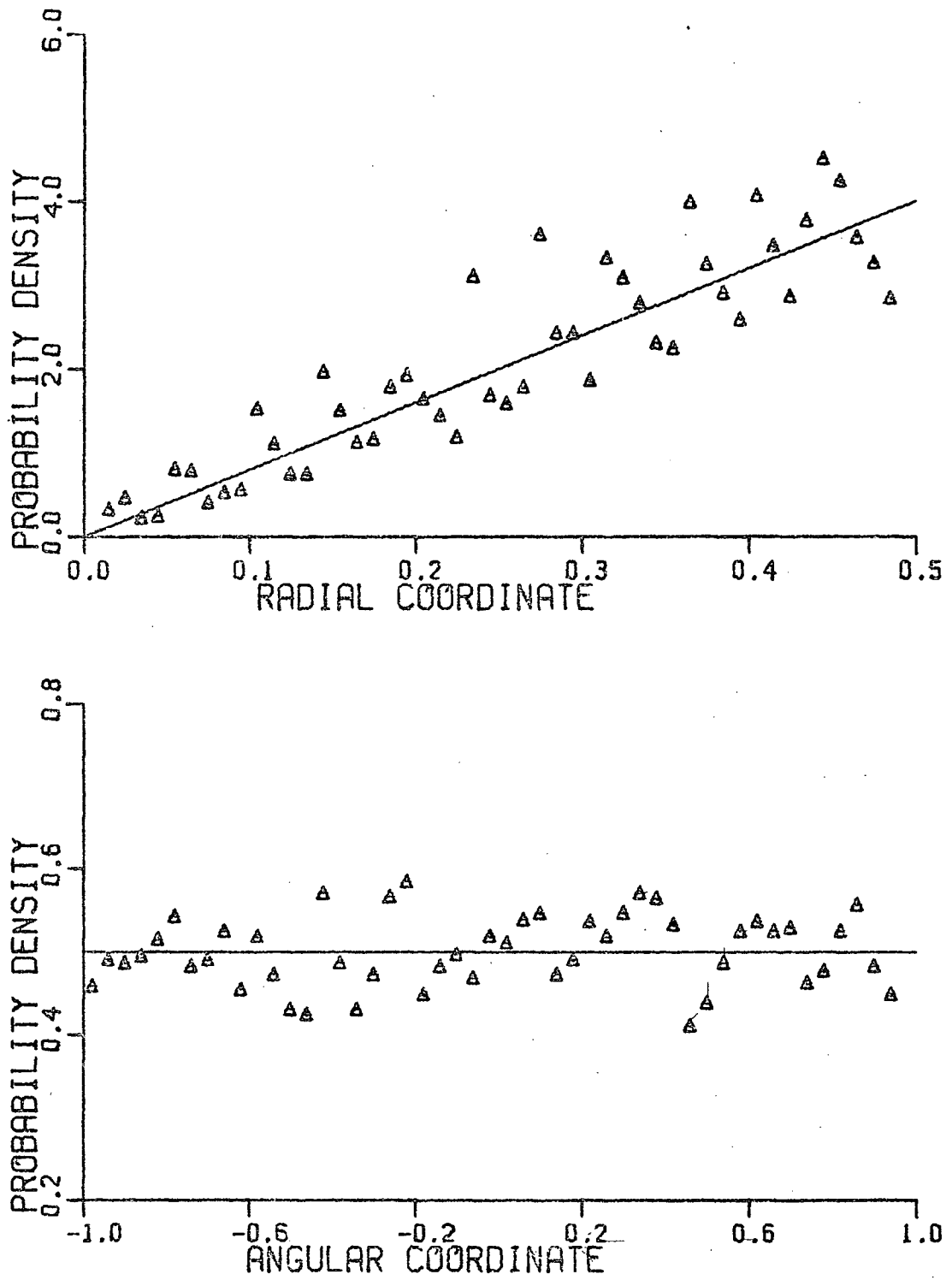


Figure 5.9 Probability Density of Hemisphere Coordinates for an Object Density of 5% and 500 Sample Surfaces, $N_s = 2$.

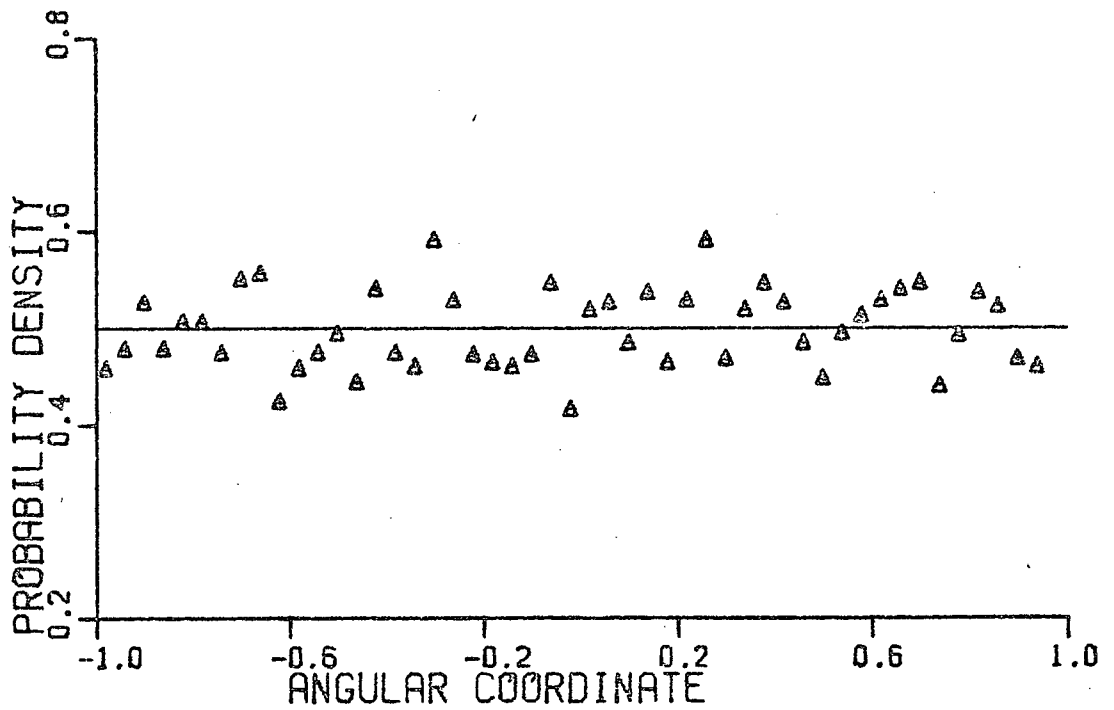
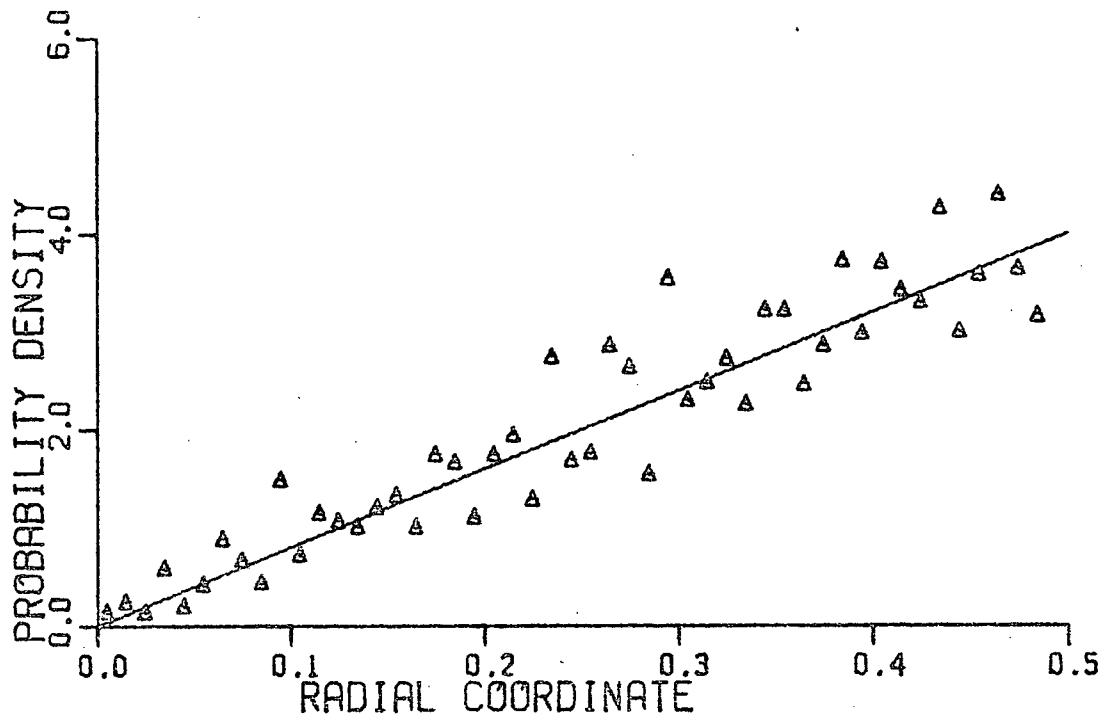


Figure 5.10 Probability Density of Hemisphere Coordinates for an Object Density of 5% and 500 Sample Surfaces, $N_s = 3$.

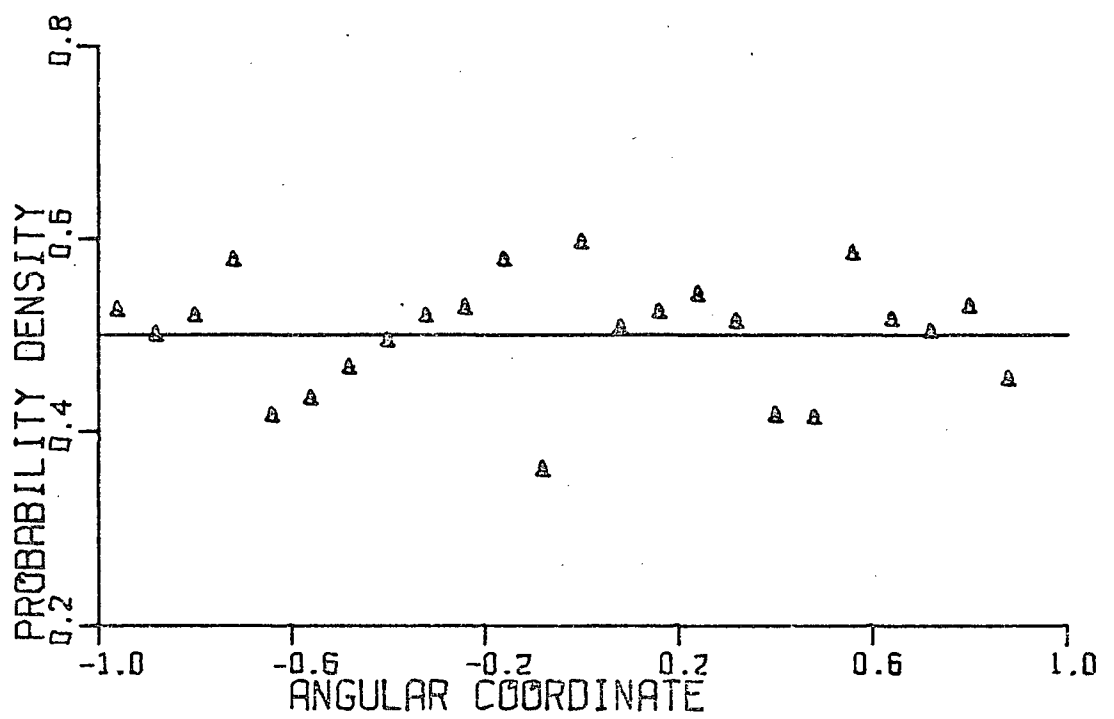
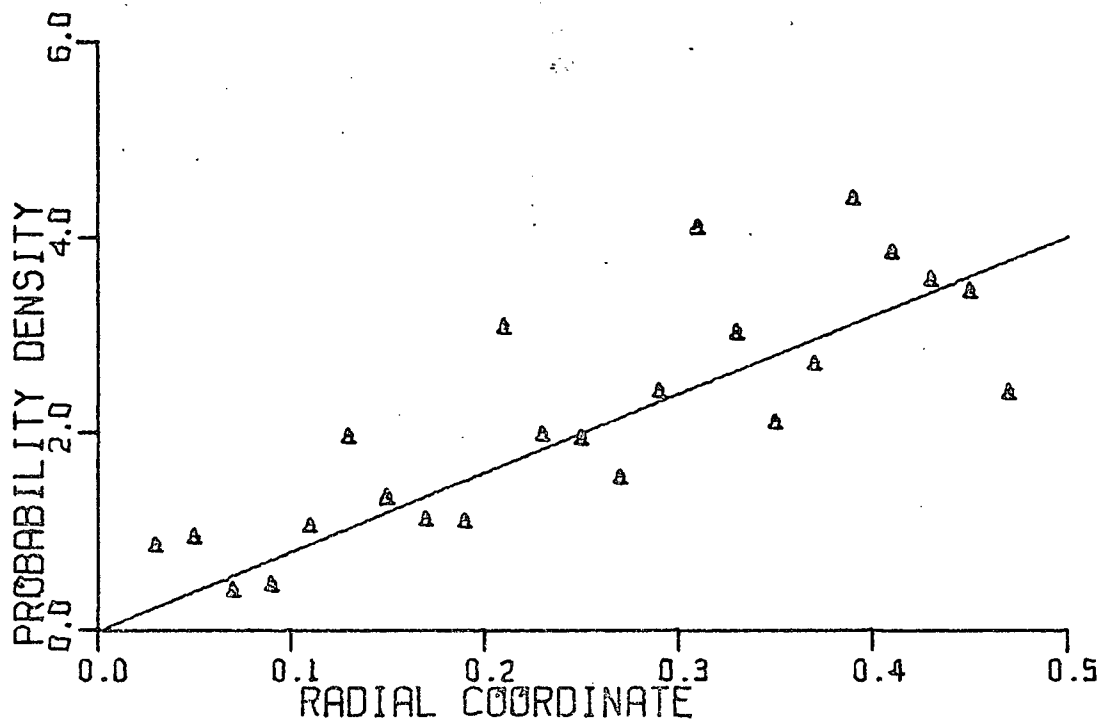


Figure 5.11 Probability Density of Hemisphere Coordinates for an Object Density of 10% and 500 Sample Surfaces, $N_s = 1$.

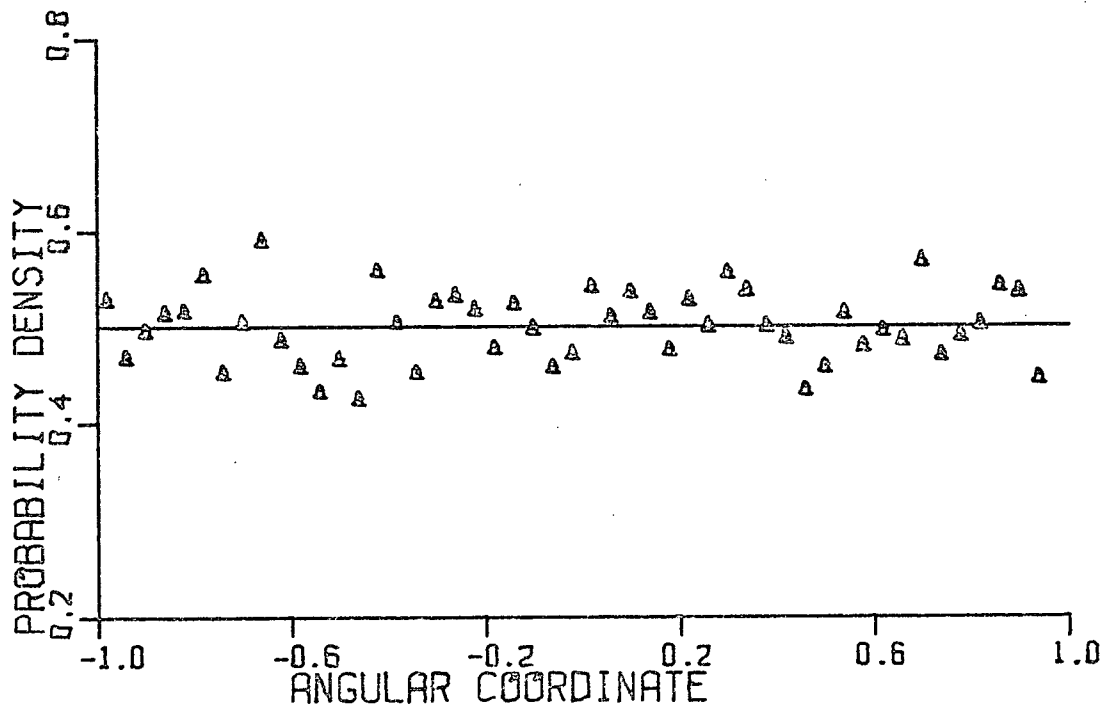
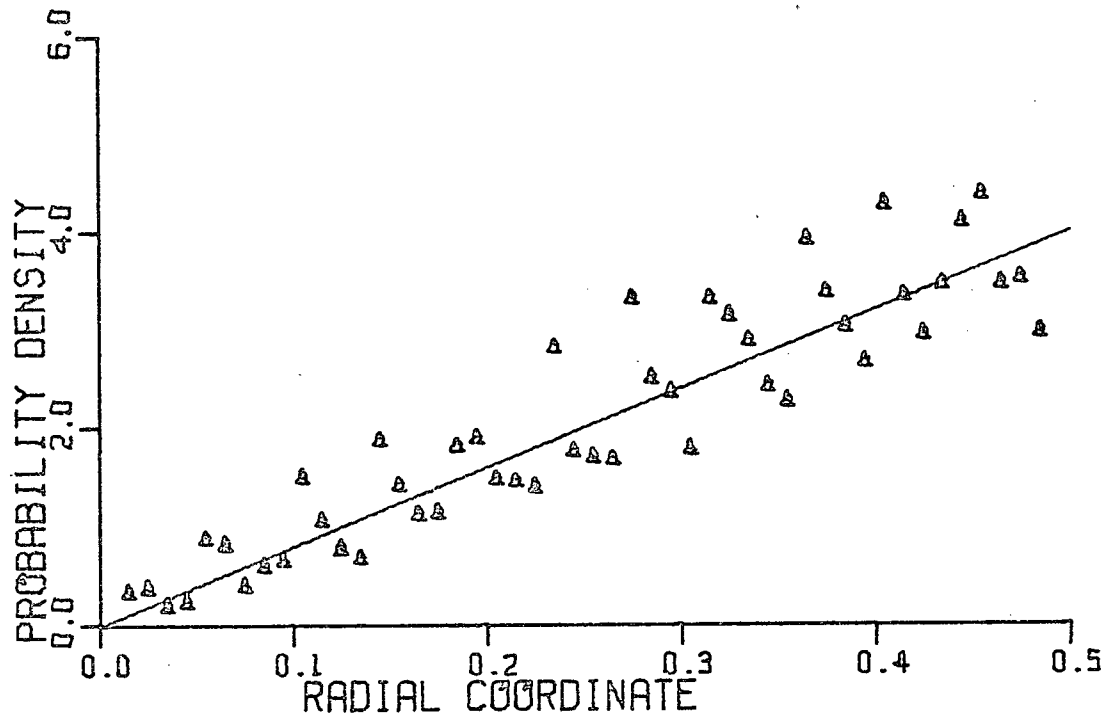


Figure 5.12 Probability Density of Hemisphere Coordinates for an Object Density of 10% and 500 Sample Surfaces, $N_s = 2$.

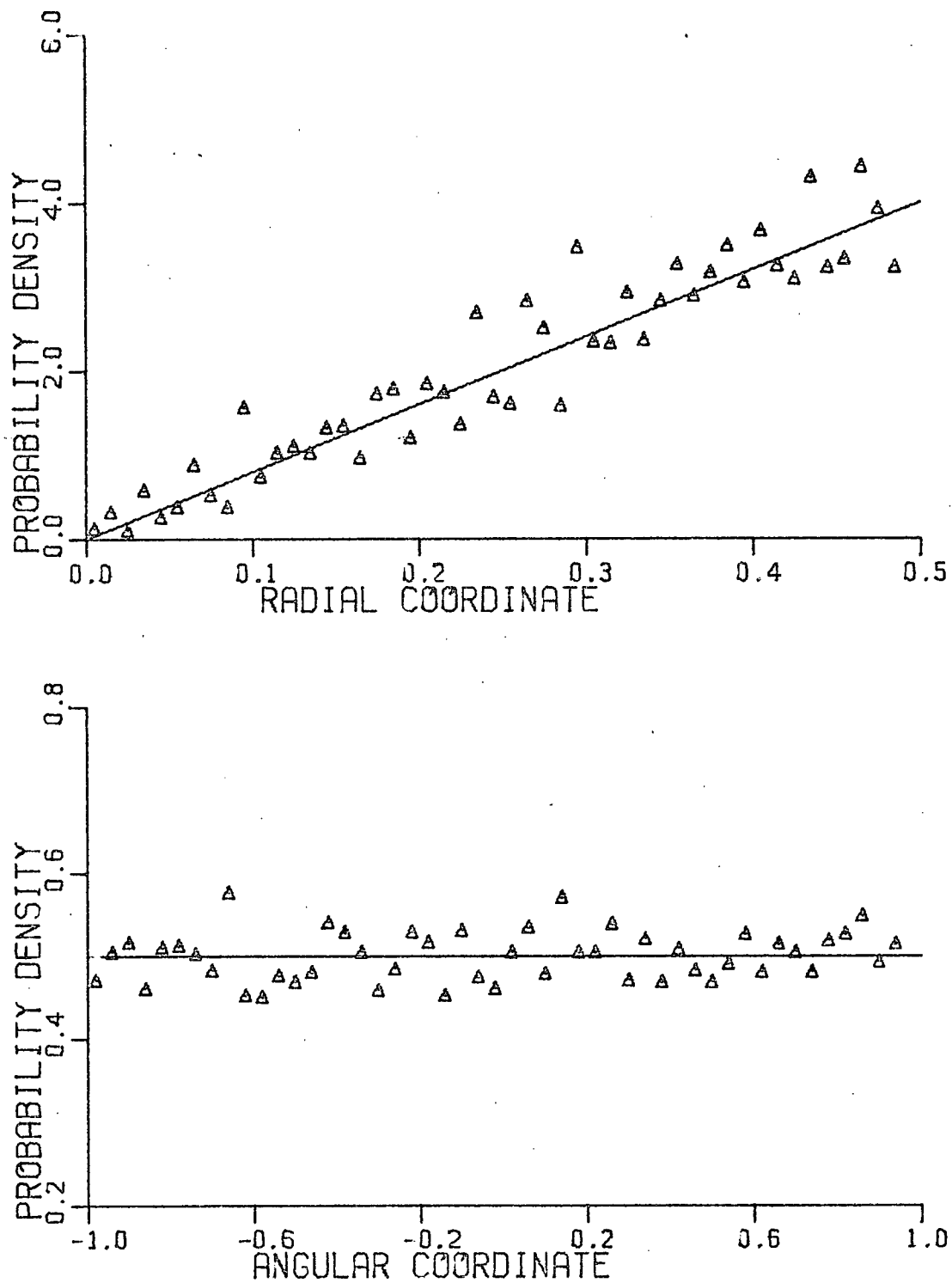


Figure 5.13 Probability Density of Hemisphere Coordinates for an Object Density of 10% and 500 Sample Surfaces, $N_s = 3$.

The following important characteristics of the surface distribution are illustrated by these graphs:

1. The distribution for $N_s=2$ (4 subcells) is more uniform than for $N_s=1$ (no subcells). For $N_s=3$, however, the improvement is not so pronounced.
2. As N_s is increased, the density function itself becomes more random. A moderate periodic effect can be seen for $N_s=1$.
3. For $N_s=1$, the probability density functions are almost identical for an object density of either 5% or 10% while for larger values of N_s , the higher object density shows the greatest amount of improvement.

Characteristics #1 and #2 show that the distribution function behaves as desired, and point out the poor characteristics of the simple discrete distribution ($N_s = 1$). Thus, the use of such a distribution is justified and #3 shows that it is even more important to use this distribution as the object density is increased. #2 also strengthens the previous choice of $N_s = 2$ for the experimental study.

The variance of the coordinate distribution is shown in figure 5.14 as a function of N_s . These curves also show that increasing N_s causes the distribution of coordinates to behave more like a continuous uniform distribution. Of course, (see figure 5.5) the minimum separation must also

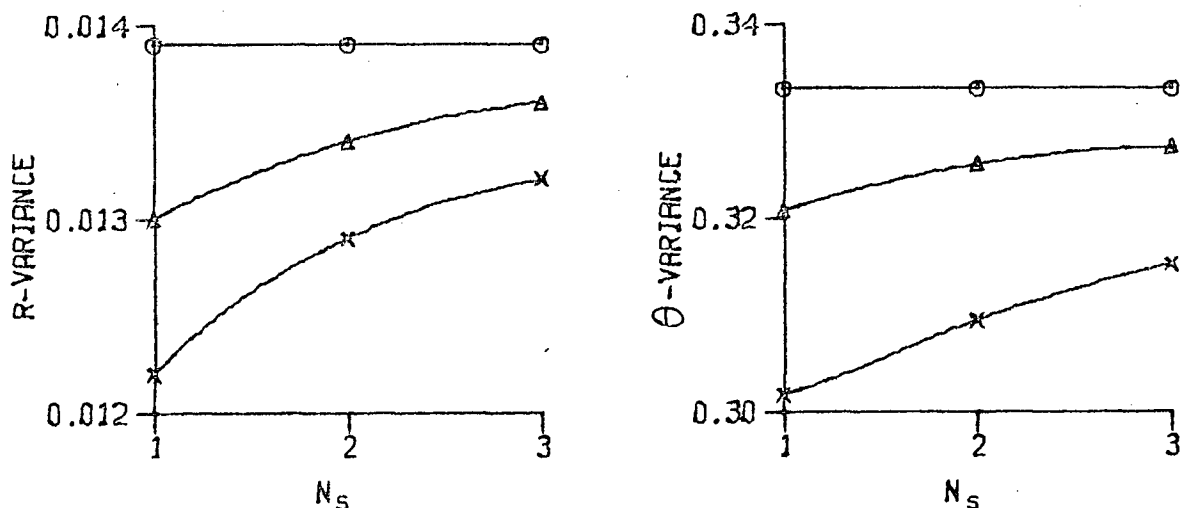


Figure 5.14 Variance of Scatterer Coordinates as a Function of N_s :
 (a) $\rho = 5\%$
 (b) $\rho = 10\%$
 (c) Continuous Uniform Distribution

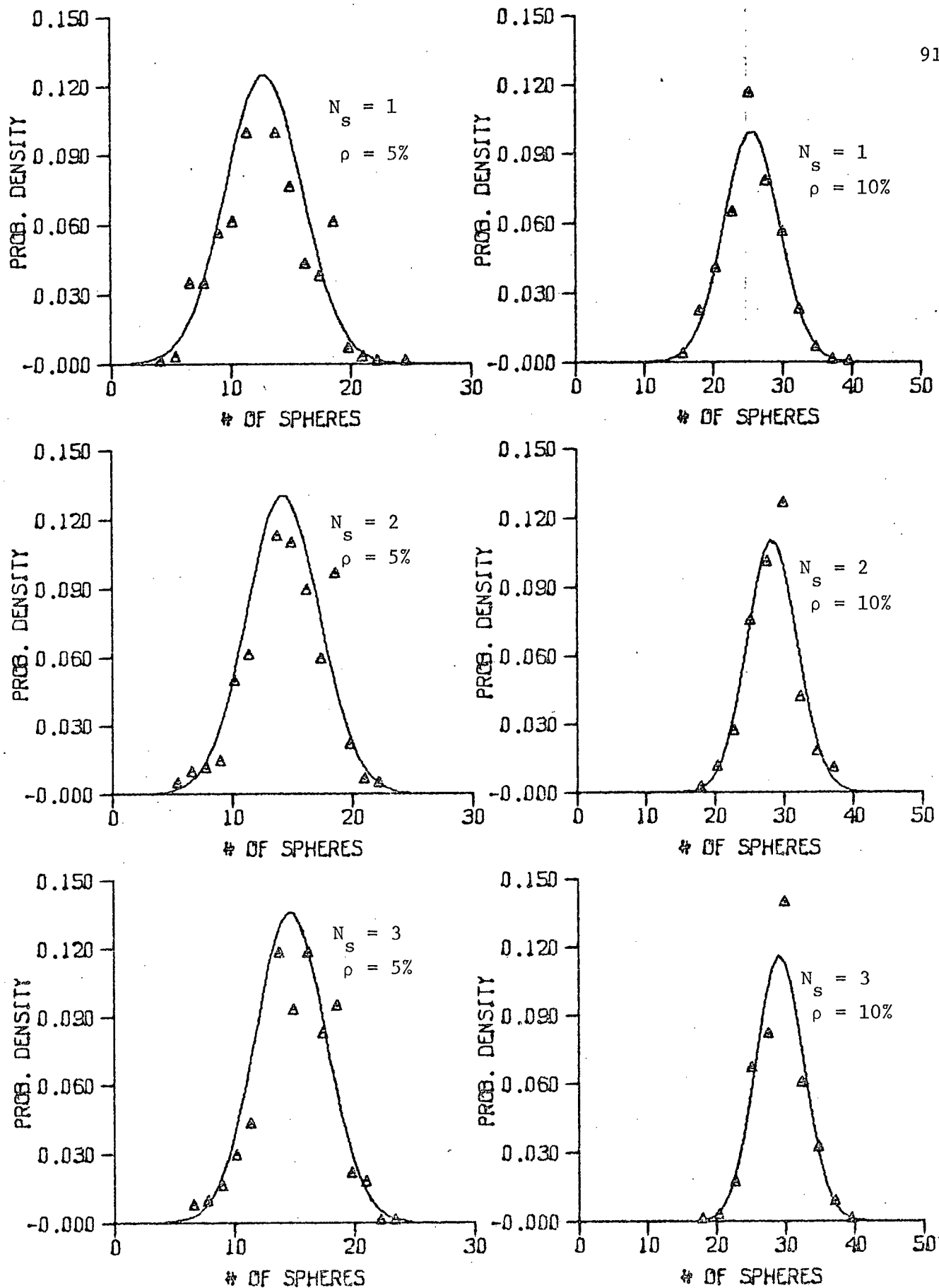


Figure 5.15 Probability Density of the Number of Spheres in the Illuminated Area for $N_s = 1, 2, 3$ and densities of 5% and 10%.

go to zero before the continuous uniform distribution is reached exactly. Notice that for the particular parameters chosen for this surface, the higher density behaves more like the continuous uniform distribution. Such behaviour is not general, however, as can be seen by the following example. Take $N_s = 1$ and a density high enough so that all boxes are filled. For this case, the distribution has become periodic for a large density, not more random.

The means of the coordinates have not been illustrated because they are quite insensitive to changes in the distribution parameters and hence remain essentially constant over the range of variables studied here.

5.2.4 Distribution of the Number of Scatterers per Independent Sample

As a final check upon the surface distribution, the probability density of the number of spheres per independent illuminated area is shown in figure 5.15. The solid curves are Normal (Gaussian) distributions calculated using the mean and variance which were determined from the actual distributions. In all cases it can be seen that the number of scatterers is distributed almost normally. The correspondence becomes better for increasing N_s , further illustrating the improvement obtained using this distribution function.

The fact that the distributions are almost normal also indicates that the illuminated areas are chosen from a sufficiently larger area. That is, edge effects and odd effects due to the fact that the density must be actually fixed over a limited area (for computational expediency) are negligible.

5.3 Initial Testing of the Experimental Surface

For an initial test to determine the magnitude of the edge effects, separation distance of the antennas, and the best widths for the flat and rough sections of the experimental surface, a special test surface was used. This surface consisted of a 2 ft. square aluminum sheet with hemispheres formed only in the lower right hand quarter.

The surface was scanned by the system shown in figure 5.1 with the antennas arbitrarily separated by 4.75 in. centre to centre. The resulting output from the receiver is shown in figure 5.16. The distances shown are actually the average of several tests performed with the surface at different elevations. The variation between these tests was slight.

From figure 5.16 it can be seen that both antennas should be about 4 in. from the edge of the surface and about 2 in. from the transition line. These figures give a smallest surface that is 12 in. wide with random scatterers over the lower 6 in.

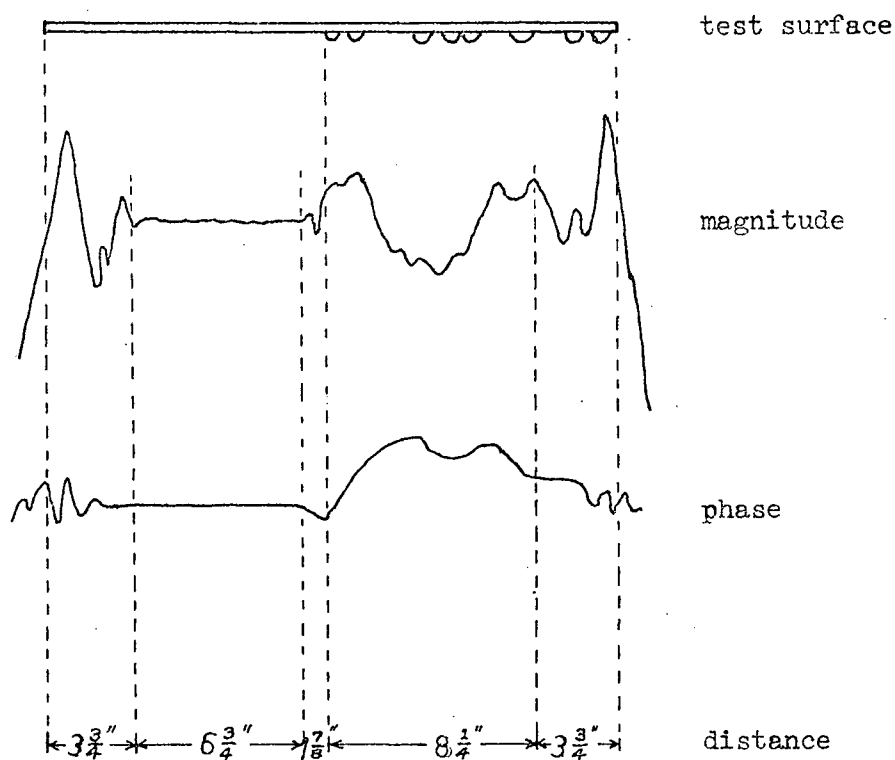


Figure 5.16 Results from the Test Surface

The "length" of the surface is determined from the facts that there must be 4 in. extra at each end to take care of edge effects while the chamber itself is 96 in. wide. These dimensions give a surface width of 52 in. with a

scanning distance of 44 in. If the apparent figure of 4 in. is assumed to give the distance between independent samples, then each surface should give at least 13 independent samples of the scattered field.

5.4 Experimental Results Compared With Simulation Results

A set of ten experimental surfaces were built according to the preceding specifications. These surfaces were scanned with the measuring and recording apparatus of figure 5.1 using the method of section 5.1.2. Frequencies of 35 to 39 GHz. in steps of 0.5 GHz. were used. A Monte-Carlo simulation was also performed, using the equations (2.133) to calculate the field. The object coordinates were generated by the same program as used for the experiment and the relative coordinates were calculated for the antenna at 100 positions across the surface to simulate the experimental scanning as closely as possible.

5.4.1 Preliminary Processing of the Experimental Data

The analog signals from the tape recorder were converted to a set of digital samples using the DEC PDP-9 digital computer and its associated multiplexed analog to digital converter. Use of the multiplexer allowed essentially simultaneous sampling of the three signal channels plus a fourth control channel, which was generated automatically by the scanner, to indicate the beginning and end of data on the other three channels. The digitalized samples were then transferred from the PDP-9 memory to punched paper tape. This paper tape was then used as input data for the much larger IBM 360/67 digital computer, which is a superior machine for performing the many accurate numerical operations required for the statistical analysis of large amounts of data. The raw data as read from the paper tape is unnormalized and consists of the following: (1) the level on the phase channel (ϕ_0) for 0°

phase shift on the receiver phase meter, (2) The reference plate reading (R_p, S_p, ϕ_p) , and (3) The signal from the surface (R_s, S_s, ϕ_s) .

The next part of the data processing is concerned with the calculation of the actual normalized samples of the scattered field. First, the 0° phase reference is averaged over all samples to minimize effects of channel noise and frequency drift. Second, the reference plate signals are averaged over all samples (there are added fluctuations here due to deviations from a perfectly flat reflector). For the normalized fields,

$$\begin{aligned} R'_p &= K_r \langle R_p \rangle \\ S'_p &= K_s \langle S_p \rangle \\ \phi'_p &= \pi \left[1 - \frac{\langle \phi_p \rangle}{\langle \phi_o \rangle} \right] + K_o \end{aligned} \quad (5.10)$$

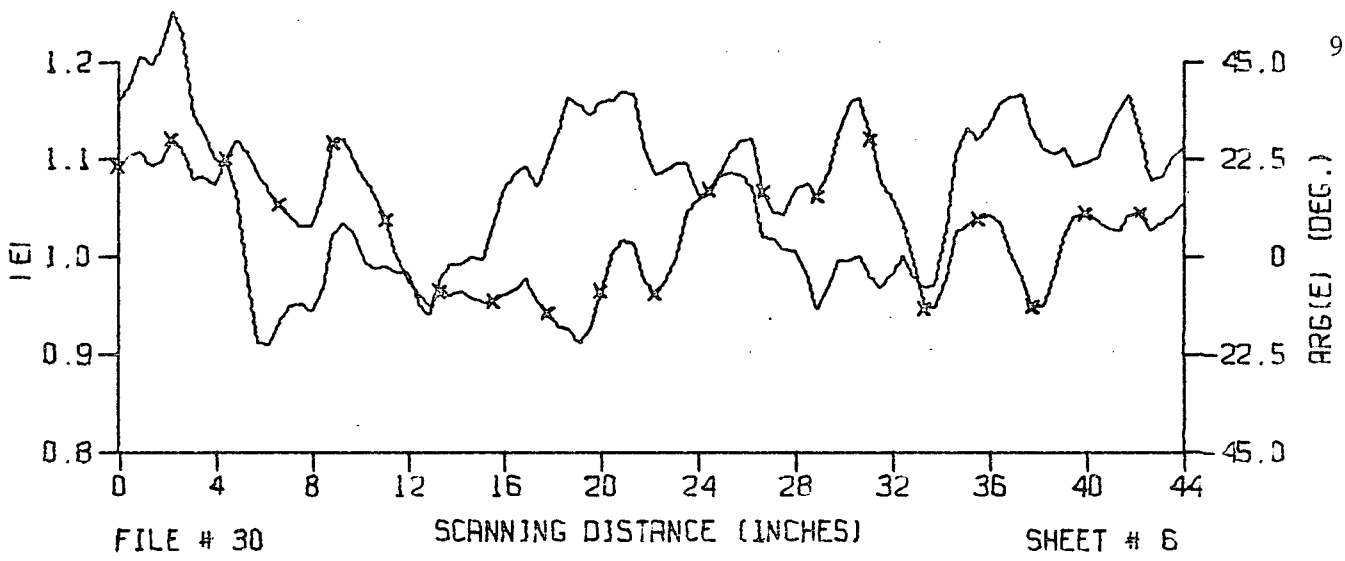
where K_r , K_s , and K_o are the overall channel gains, and R'_p , S'_p , and ϕ'_p are the true normalized field values. Thus

$$\begin{aligned} R'_p &= S'_p = 1 \\ \phi'_p &= 0^\circ \end{aligned} \quad (5.11)$$

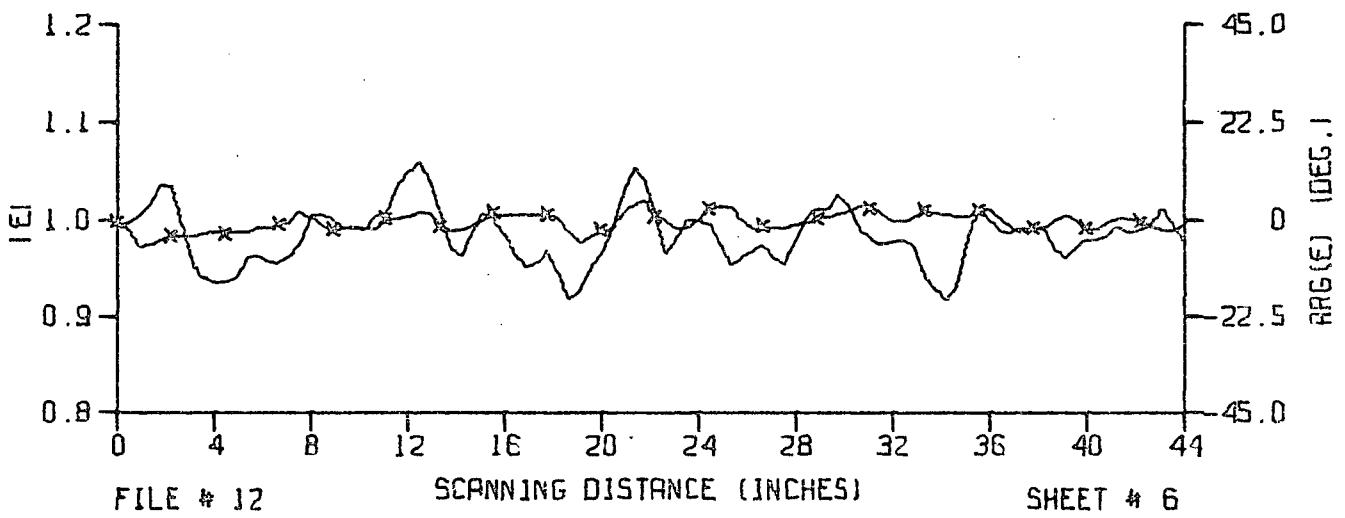
so that the k^{th} sample of the normalized field scattered from the rough surface is given by

$$\begin{aligned} |E(k)| &= \frac{S_s \langle R_p \rangle}{R_s \langle S_p \rangle} \\ \arg(E(k)) &= \left\{ \langle \phi_p \rangle - \phi_s \right\} \frac{\pi}{\phi_o} \end{aligned} \quad (5.12)$$

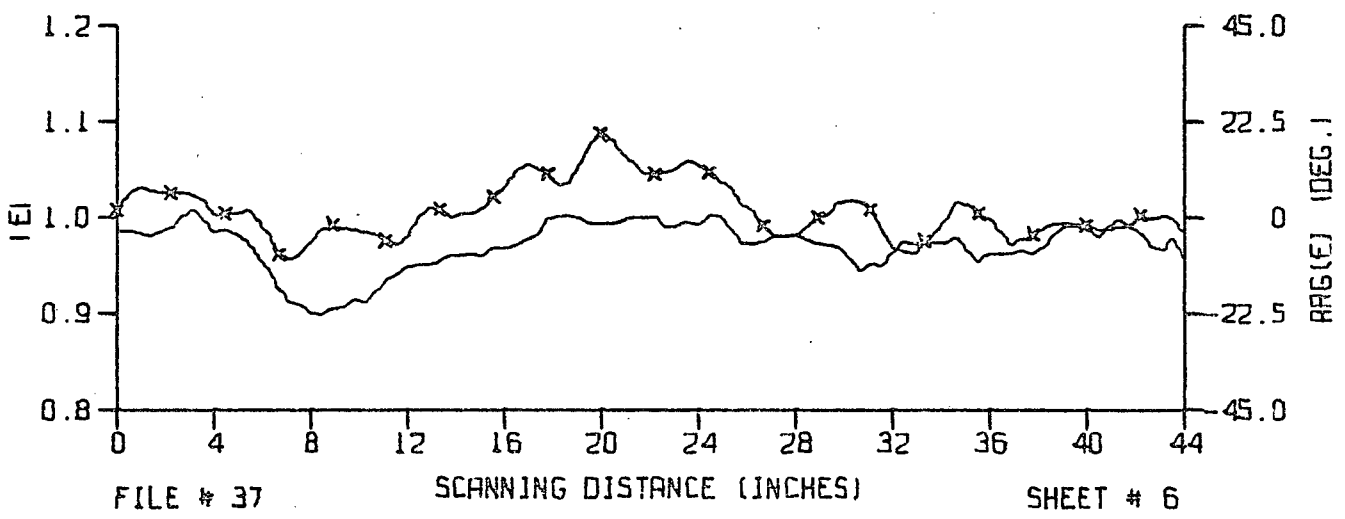
These two quantities were calculated for each sheet (approximately 100 samples per sheet per frequency) and stored on digital magnetic tape for the subsequent statistical analysis which comprises the third and final stage



(a)



(b)



(c)

$|E|$  $Arg(E)$ 

Figure 5.17 (a) Experimental Data from a Typical Sheet
(b) Simulation Data from a Typical Sheet
(c) Experimental Data Averaged over the Frequency Range

of the processing of the experimental data. The corresponding samples generated by the Monte-Carlo simulation were also stored on the same magnetic tape for ease of comparison.

These sets of normalized data were plotted against the scanning position for a preliminary inspection before any further processing was carried out. Data for a typical sheet is shown in figure 5.17 (a) and (b). It was noticed that some of the experimental curves showed an appreciable linear offset from the normalized values, as well as the expected random variations. These offsets were completely different from sheet to sheet and for different frequencies, indicating that some measurement errors due to improper normalization remain in spite of the precautions which have been taken (see section 5.1.2). The Monte-Carlo simulation results, however, do not exhibit this characteristic and furthermore, they show very little variation over the range of frequencies used (due to the fact that the field is normalized for each frequency). The absence of this variation with frequency was fortunate, and suggested one final method for reducing measurement errors.

Assume that the offset errors are completely random for each scan, and that the actual variation with frequency is essentially negligible as indicated by the simulation. Then, average the data over the various frequencies to obtain one set of frequency averaged data. The data so obtained will then be approximately that obtained by performing the identical experiment nine times and using the average of the nine readings. This process will also reduce errors due to measurement of the parameters of the system such as the antenna to surface distance. Typical frequency averaged data is shown in figure 5.17 (c). Notice that the offset for this sheet has been considerably reduced.

5.4.2 Correlation Distance for the Scattered Field

To determine the maximum number of independent samples which can be obtained from each surface, the magnitude of the complex autocorrelation coefficient,

$$\rho_d = \frac{1}{\sigma_E^2} \left[\frac{1}{N} \sum E^{(k)} E^{(k+d)*} - \langle E \rangle \langle E^* \rangle \right] \quad (5.13)$$

was calculated both for the experimental data and for the simulation data.

ρ_d was calculated separately for each sheet and then averaged over all sheets to yield the curves shown in figure 5.18 (a). For comparison, it can be seen from figure 2.5 that for the experimental antenna to surface distance of 27 inches, the 3 db width of the beam at the surface is approximately 3.6 in. while the width of the entire main beam is about 7.9 in.

The simulation curve gives an uncorrelated distance of about 1.75 in. which is considerably less than the half-power width, while the experimental results yield an uncorrelated distance slightly larger than the half-power width (similar results were obtained in the preliminary testing of section 5.3). This discrepancy may be explained by considering the opposing errors for the two methods.

For the Monte-Carlo simulation, the main source of error is caused by the single scatter approximation. The absence of M.S. will cause the autocorrelation function to be narrower, and have a sharper transition from correlated to uncorrelated samples because interactions from adjacent but unilluminated areas are not considered. A secondary source of error, that of considering the antenna beam amplitude to be zero beyond a certain angle will also contribute to this effect.

On the other hand, the main experimental errors will tend to widen the correlated area. These errors are caused by improper normalization and surface

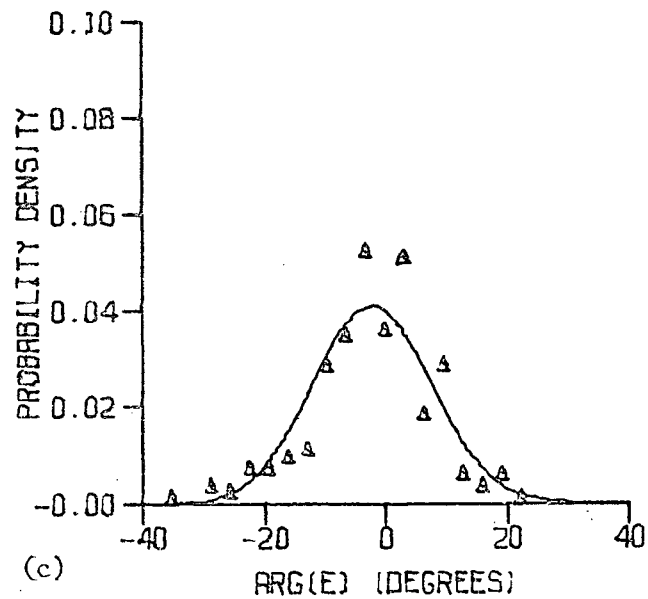
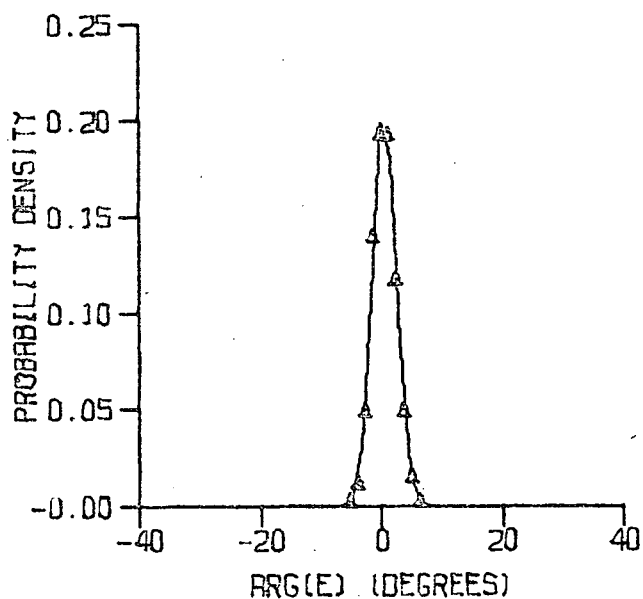
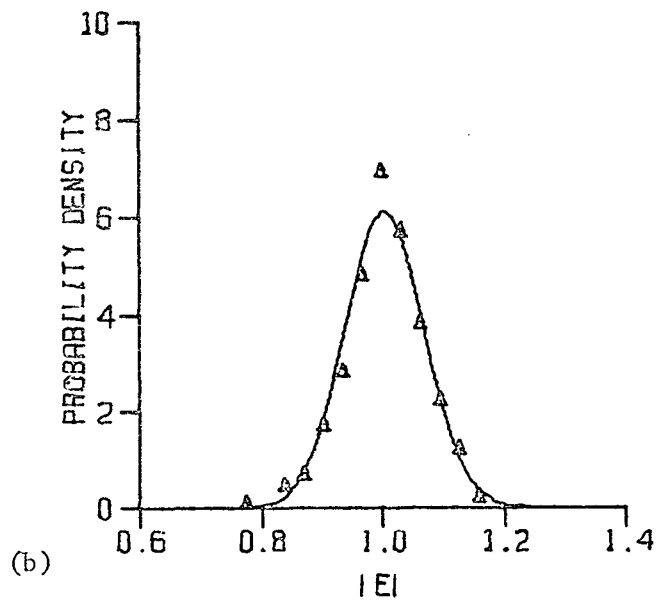
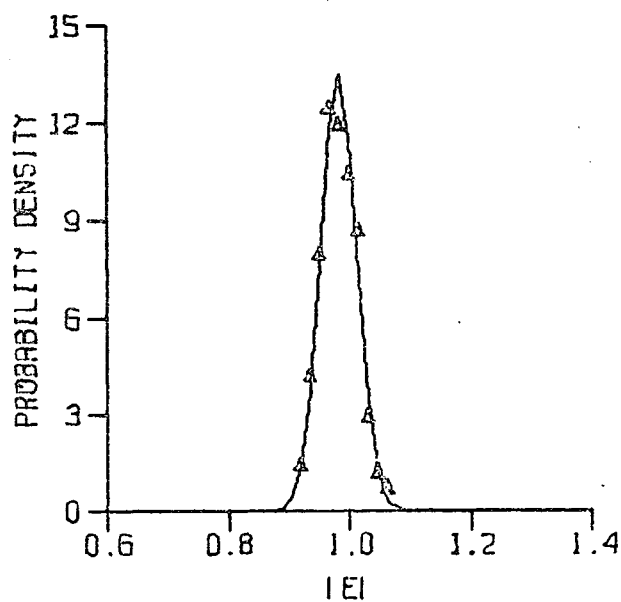
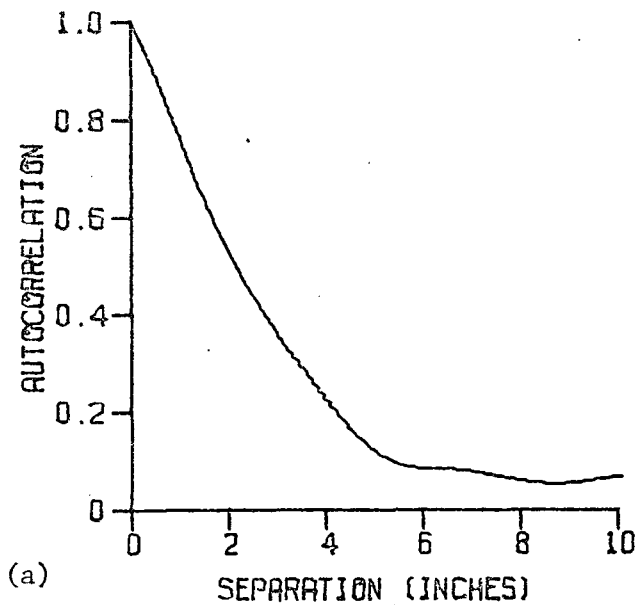
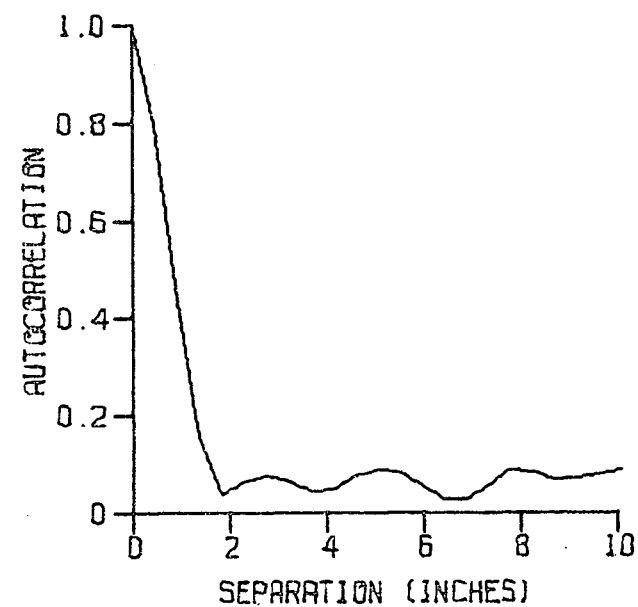


Figure 5.18 Statistics of Simulated (left) and Experimental (right) Data.
 (a) Autocorrelation of the Electric Field as a function of the distance between samples.
 (b) Probability Density of the Magnitude of the Field.
 (c) Probability Density of the Phase of the Field.

waviness due to slight bending of the aluminum sheet. Both of these effects cover areas wider than the beamwidth, and hence will increase the correlation over a fairly long distance.

In view of the above results, it was decided to keep samples that were the half-power width (i.e. 3.6 in.) apart. Thus, 13 independent samples per sheet were obtained.

5.4.3 Statistics of the Scattered Field

For the simulation and for the experiment, the coherent and incoherent fields were calculated along with their probability density functions. The probability densities are shown in figures 5.18 (b) and (c). The solid curves are normal densities calculated using the mean and variance of the respective data. The statistical moments are given in table 5.1.

	c^2	α	I^2	$\langle E \rangle$	$\sigma_{ E }^2$	$\langle \arg E \rangle$	$\sigma_{\arg E}^2$
simulation	.9541	.3469 ^o	.00221	.9835	.595	.0009	2.79
experiment	.9755	2.335 ^o	.03265	1.0025	2.17	.0052	98.0

Table 5.1 Statistics of Simulation and Experimental Data.

From figure 5.18 (b) and table 5.1 it can be seen that the distributions of the field magnitude for the experiment and for the simulation are reasonably similar. The means are very close, while the standard deviation for the experiment is increased by a factor of about 2.4. A reasonable agreement between these figures is expected because the measurement of the magnitude of the field is not nearly as sensitive to experimental error as is the phase measurement. Thus, it is reasonable to conclude that a high percentage of the deviation is due to multiple scattering effects. The sensitivity of the phase measurements is illustrated in figure 5.18 (c) where the phase

distributions are shown. Here there is an appreciable difference between the experiment and the simulation. In fact, the standard deviation for the experimental data is now almost 6 times larger.

5.5 Summary

The experimental approach as investigated in this chapter can be considered to be a qualified success. The method itself is an excellent one, but the use of the existing scanner introduced some large errors which made it difficult to assess quantitatively the comparative behaviour of the simulation and the experiment. Suggestions for improving this situation are given in sections 6.3 and 6.4.

The design of the surface model and its associated distribution function, though, was found to be experimentally practical and a good representation of a random surface. The actual distribution used for the experiment was based upon a division of the original $\frac{1}{2}$ in. cells into four $\frac{1}{4}$ in. subcells. The coordinate distribution generated for this choice of N_s was found to give an acceptable trade-off between computation time and the required characteristics of the distribution.

A detailed study of the behaviour of the model would require that many more surfaces be built for several different parameter values. This extension of the work was considered to be beyond the range of this thesis.

6. CONCLUSIONS

6.1 Surface model

The results of section 5.1.3 and 5.2 indicate that the surface model developed in this thesis has all the characteristics that were originally required. Basically, these requirements were

1. That the statistics could be controlled as desired.
2. That the model be usable both for computer simulation and for actual experiments.

The first criterion was satisfied by using an array of discrete scatterers (as opposed to a continuous rough surface) where the randomness was determined by using a computer generated pseudo-random sequence. In the case studied here, the randomness was introduced by the scatterer coordinates although other variables such as scatterer size and/or shape could have been used. In the simplest case, the simulation of the single scattered field, no special problems arise. That is, a continuous uniform distribution may be used directly to generate the coordinates because overlapping scatterers do not matter.

For any simulation which includes multiple scatter (and hence scatterer separation) or to satisfy the second criterion above, a more sophisticated coordinate distribution function must be utilized. Such a distribution function was developed in section 4.1 and fully tested in section 5.2. The test results, which are illustrated in figures 5.6 to 5.16, show that this distribution is an acceptable function to use for the study of any discrete scatterer problem. It is a good approximation to a continuous uniform distribution, and it is simple and quick to numerically calculate for one, two, or three dimensional position vectors.

The second criterion further limited the model to be composed of specific shapes (hemicylinders and hemispheres) so that either the scattered field could be represented mathematically with ease, or that a metal surface model could be machined into the same shape. The mathematical scattering functions are derived in Chapter 2 while the method of surface construction is outlined in section 5.1.3. The accuracy of data obtained using this surface model depends upon the degree of approximation which is applied to the mathematical scattering functions and the degree of precision with which the surface is machined. For this study, the single scatter approximation was mainly used for the simulation, and the experimental surface was formed with a tolerance of better than $\pm 5\%$ for object size and shape. Slight distortion of the surface between scatterers was inevitable.

The surface model developed in this thesis for the study of rough surface scattering was, therefore, found to be entirely satisfactory. This model is versatile, easy to use, and lends itself to generalization to higher orders of randomness.

6.2 Simulation

The aims of the computer simulation of the rough surface scattering problem were essentially:

1. To find a good mathematical method for the field calculations based upon the prior choice of surface model.
2. To use finite non-plane incident radiation, representative of a physical antenna.
3. To provide comparison with experimental studies.

As only a numerical method for determining a surface distribution was developed, the average field calculations were based on a Monte-Carlo method. A single calculation will therefore involve only the instantaneous field

value due to a fixed configuration, while the actual statistics are calculated from a set of such values. It was found impractical to use any other than the single scatter or first order nearest neighbour approximation for the field due to a single configuration, but only the single scatter method was generally used. Higher order multiple scattering effects were investigated however, for the restricted case of a periodic array of hemicylinders. The results indicated that for densities of greater than 30% and object size greater than $\frac{1}{2}\lambda$ in radius the multiple scattering effect is definitely not negligible.

The Monte-Carlo method requires that only a finite number of scatterers be considered. This is not a serious constraint because physical problems are nearly always composed of finite areas of surface. In fact, the second aim of this part of the study automatically restricts the number of scatterers per sample by requiring only a finite beam of illumination. The particular form of the incident radiation is developed in section 2.4 and illustrated in figure 2.5. The functions were chosen to reasonably approximate a horn antenna radiation pattern, have independently variable beamwidth and sidelobe level, and be simple to calculate numerically. The values of the variable parameters of this model were subsequently set to approximate the horn antenna used for the experiment.

The one problem which is encountered with the finite beam is that it is difficult to directly compare the results with other methods of calculation. This was attempted in section 4.4, where some analytical solutions are given for the coherent and incoherent fields. It was concluded that the Monte-Carlo simulation was the best means of calculation.

6.3 Experiment

The aims of the experimental study were

1. To demonstrate that a suitable experiment could be performed.
2. To compare with numerical methods.
3. To extend the investigation to areas where numerical methods are prohibitive.

The first goal above was amply demonstrated. The technique of scanning a formed metal surface was shown to be a practical method. The forming of the sheet according to the pre-calculated distribution of coordinates was quick and very simple once the proper punch and die had been constructed. The scanning system that was used though, was less than perfect, giving rise to relatively large phase measurement errors. Some methods of preventing this problem in future experiments are discussed in the next section.

The experimental results compare favorably with the simulation, but the aforementioned phase errors make it difficult to interpret the deviations in terms of specific mechanisms. A set of experimental data for various densities would most likely help to analyse the various errors, but this is beyond the scope of this work.

The third goal has been attained in theory, but was judged also to be beyond the present scope. The formed metal surface can directly accommodate high densities of scatterers, large sizes of scatterers, and odd shaped scatterers. With a slight modification to the distribution function random sizes of scatterers could also be included.

6.4 Numerical Results

The main result of this study has been to develop certain valid methods for investigating the behaviour of rough surface scattering. There are a large number of variable parameters, and even for a fixed set of parameters, a large number of random variables inherent in this problem. Because of this, a detailed numerical study of the scattered field was not

undertaken. Instead, the behaviour of parts of the scattering were investigated for suitability and for the best parameter values to use for subsequent calculations.

For the periodic model of hemicylinders it was found that

1. The width of the active scattering area should be at least comparable to the width of the main beam of the antenna at the surface.
2. The relative error from neglecting multiple scatter is less than 20% for $a \leq 0.5\lambda$ and $\rho \leq 35\%$ except for some special values of a .
3. The first order nearest neighbour approximation reduces these errors by a factor of 1/2.
4. Computation time is prohibitive for higher order approximations.

For the random single scatter model of hemicylinders with a continuous uniform coordinate distribution, the coherent field and incoherent intensity were determined analytically. Comparison with the Monte-Carlo simulation showed that the calculation of the coherent field is relatively inaccurate while the calculation of the incoherent intensity gives excellent results.

The following results were noticed for the coordinate distribution:

1. The improvement attained by using this distribution increases with object density.
2. Division of the simple model into only four subcells is sufficient to produce a reasonably uniform distribution without excessive computation time.
3. The finite separation of the scatterers necessitated by the experiment causes a negligible effect.

6.5 General Recommendations

The main problem involved in this investigation is the need for control of the various errors so that their effect can be evaluated. This was done

to a limited extent by studying a special case - the periodic two dimensional array. It would thus be very instructive to extend the accuracy in a specific manner of the three dimensional problem for the simulation and for the experiment.

The accuracy of the simulation could be improved by deriving the first order nearest neighbour approximation for the array of hemispheres. The comparison of these results with the single scatter results would give a better indication of the amount of multiple scatter in this case.

The experimental results could be greatly improved, and the actual setting up of the experiment (it took a long time to properly mount the sheets and align the scanner for each data set) made easier by redesigning the scanner itself. The scanner which was used for the experiment was originally designed as an antenna positioner for pattern measurements, and therefore moved in a vertical plane. The problems encountered were due to the surface to antenna distance changing due to improper alignment. These problems would be eliminated if the surface was lying in a horizontal plane, and supported upon a flat backing plate which was in turn supported on rollers. The antennas could then be directed straight downward from some point above the device (e.g. suspended from the ceiling) while the surface was gently pulled across beneath by means of a wire winding on a drum. Mounting of the surface upon the scanner would also be facilitated because gravity would hold it in position, unlike the vertical mounting system that was used.

APPENDIX A DETERMINATION OF UNKNOWN SCATTERING COEFFICIENTS

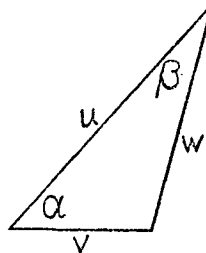
The total electric field, using the equations (2.1), (2.14), and (2.15) of Chapter 2, may be written as:

$$\begin{aligned}
 E_T &= E_{inc} + \sum_{s=1}^{N_o} E_s \\
 &= E_{inc} + E_s + \sum_{\substack{t=1 \\ t \neq s}}^{N_o} E_t \\
 &= E_o D_s \sum_{n=-\infty}^{\infty} J_n(kr_s) (i)^n e^{in(\theta_s + \beta_s)} + \sum_{n=-\infty}^{\infty} B_{ns} H_n(kr_s) e^{in\theta_s} \\
 &\quad + \sum_{\substack{t=1 \\ t \neq s}}^{N_c} \sum_{n=-\infty}^{\infty} B_{mt} H_m(kr_t) e^{im\theta_t}
 \end{aligned} \tag{A.1}$$

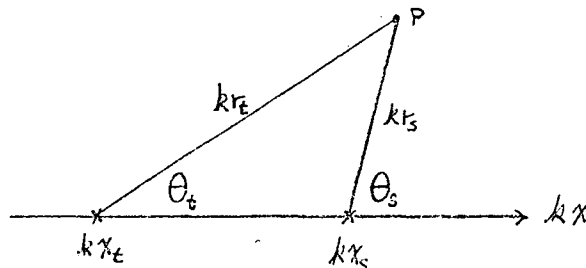
Now, Graf's addition theorem for cylinder functions²⁷ is

$$C_n(w) e^{in\alpha} = \sum_{k=-\infty}^{\infty} C_{n+k}(u) J_k(v) e^{ik} \tag{A.2}$$

where $|v| < |u|$ and u, v, w, α , and β are related by the following geometry,



and $C_n(x)$ is any cylinder function. Apply this theorem to equation (A.1) for $t < s$:



From the above diagram,

$$H_m(kr_t) e^{im\theta_t} = \sum_{n=-\infty}^{\infty} H_{m+n}(k(x_s - x_t)) J_n(kr_s) e^{in(\pi - \theta_s)} \tag{A.3}$$

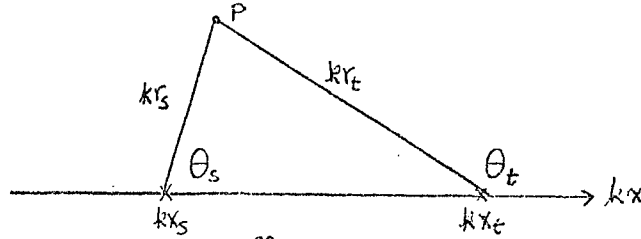
or, by using the fact that

$$C_n(Z) = (-1)^n C_{-n}(Z) \quad (\text{A.4})$$

replacing n by $-n$ and summing in the opposite direction obtain the equivalent expression

$$H_m(kr_t)e^{im\theta_t} = \sum_{n=-\infty}^{\infty} (-1)^{m+n} H_{n-m}(k|X_s - X_t|) J_n(kr_s) e^{in\theta_s} \quad (\text{A.5})$$

Now, for $t > s$,



$$H_m(kr_t)e^{im\theta_t} = \sum_{n=-\infty}^{\infty} H_{n+m}(k(X_t - X_s)) J_n(kr_s) e^{in\theta_s} \quad (\text{A.6})$$

Again,

$$H_m(kr_t)e^{im\theta_t} = \sum_{n=-\infty}^{\infty} H_{n-m}(k(X_t - X_s)) J_n(kr_s) e^{in\theta_s} \quad (\text{A.7})$$

The combination of equations (A.5) and (A.7) may be written

$$H_m(kr_t)e^{im\theta_t} = \sum_{n=-\infty}^{\infty} H_{n-m}(k|X_s - X_t|) J_n(kr_s) e^{in\theta_s} F_{nm}^{st} \quad (\text{A.8})$$

with

$$F_{nm}^{st} = \begin{cases} (-1)^{m+n}, & t < s \\ 1, & t > s \end{cases} \quad (\text{A.9})$$

Therefore, the total electric field becomes

$$E_T = \sum_{s=1}^{N_0} \left[E_{0s} D_s \sum_{n=-\infty}^{\infty} J_n(kr_s) (i)^n e^{in(\theta_s + \phi_s)} + \sum_{n=-\infty}^{\infty} B_{ns} H_n(kr_s) e^{in\theta_s} \right] + \sum_{\substack{t=1 \\ t \neq s}}^{N_0} \left[\sum_{m=-\infty}^{\infty} B_{mt} \sum_{n=-\infty}^{\infty} H_{n-m}(k|X_s - X_t|) J_n(kr_s) e^{in\theta_s} F_{nm}^{st} \right] \quad (\text{A.10})$$

The following boundary conditions must be satisfied on the surfaces of the cylinders, i.e. at $r_s = a$,

$$\begin{aligned} E_T &= 0, \quad \perp \text{ polarization} \\ \frac{\partial E_T}{\partial r_s} &= 0, \quad \parallel \text{ polarization} \end{aligned} \quad (\text{A.11})$$

Since (A.10) must hold for all θ_s , the coefficients of each $e^{in\theta_s}$ may be equated to zero in equation (A.10) or its r_s derivative, which yields the equation for the unknown coefficients, B_{ns} :

$$B_{ns}^{\parallel, \perp} = A_n^{\parallel, \perp} \left[E_0 D_s (i)^n e^{in\theta_s} + \sum_{\substack{t=1 \\ t \neq s}}^{N_0} \sum_{m=-\infty}^{\infty} B_{mt} H_{n-m} (k |X_s - X_t|) F_{nm}^{st} \right] \quad (\text{A.12})$$

where

$$\begin{aligned} A_n^{\perp} &= -\frac{J_n(ka)}{H_n(ka)} \\ A_n^{\parallel} &= -\frac{J_n'(ka)}{H_n'(ka)} \end{aligned} \quad (\text{A.13})$$

APPENDIX B RELATIONS BETWEEN REAL AND IMAGE FUNCTIONS

The problem is to simplify the expression for the scattered field caused by the th hemisphere as given by equation (2.30) of Chapter 2, that is

$$E_s^{||, \perp} = E_s^r + E_s^i \quad (\text{B.1})$$

where the superscripts r and i refer to the real and image functions respectively. Therefore, from equation (2.15),

$$E_s^{||, \perp} = \sum_{n=-\infty}^{\infty} (B_{ns}^r \pm B_{ns}^i) H_n(kr_s) e^{in\theta_s} \quad (\text{B.2})$$

And, from equation (2.17),

$$B_{ns}^r = A_n \left[E_0 \frac{e^{ikC_s}}{\sqrt{kC_s}} f\left(\frac{\pi}{2} - \alpha - \beta_s\right) (i)^n e^{in\theta_s} + \sum_{\substack{t=1 \\ t \neq s}}^{N_0} \sum_{m=-\infty}^{\infty} B_{mt} G_{nmst} \right] \quad (\text{B.3})$$

Note that G_{nmst} is not a function of α . To find B_{ns}^i , α must be replaced by $\pi - \alpha$. First, it is obvious that the distance C_s must be the same for the real and image functions. Second, the angle β_s is given by

$$\begin{aligned} \tan \beta_s^i &= \frac{L \cos(\pi - \alpha)}{X_s + L \sin(\pi - \alpha)} \\ &= \frac{-L \cos \alpha}{X_s + L \sin \alpha} \\ &= -\tan \beta_s^r \end{aligned} \quad (\text{B.4})$$

Therefore,

$$B_s^i = -B_s^r \quad (\text{B.5})$$

Third, the antenna radiation pattern is given by

$$\begin{aligned} f^i &= f\left(\frac{\pi}{2} - \pi + \alpha + \beta_s^r\right) \\ &= f\left(-\frac{\pi}{2} + \alpha + \beta_s^r\right) \end{aligned} \quad (\text{B.6})$$

But, the antenna pattern may be assumed to be an even symmetric function, therefore

$$f^i = f^r \quad (\text{B.7})$$

The above may be applied to equation (B.5)

$$B_{ns}^i = A_n \left[E_0 \frac{e^{ikC_s}}{\sqrt{kC_s}} f\left(\frac{\pi}{2} - \alpha - \beta_s\right) (i)^{-n} e^{-in\theta_s} + \sum_{t=1}^{N_0} \sum_{m=-\infty}^{\infty} B_{mt}^i G_{nmst} \right] \quad (\text{B.8})$$

By a comparison of (B.3) and (B.8) it can be seen that

$$B_{-ns}^i = (-1)^n B_{ns}^r \quad (\text{B.9})$$

Hence, after dropping the superscript r ,

$$\begin{aligned} E_s^{\parallel, \perp} &= \sum_{n=-\infty}^{\infty} (B_{ns} \pm (-1)^n B_{-ns}) H_n(kr_s) e^{in\theta_s} \\ &= \sum_{n=1}^{\infty} (B_{-ns} \pm (-1)^n B_{ns}) (-1)^n H_n(kr_s) e^{-in\theta_s} \\ &\quad + (B_{ns} \pm (-1)^n B_{-ns}) H_n(kr_s) e^{in\theta_s} + (B_{0s} \pm B_{0s}) H_0(kr_s) \\ &= \sum_{n=1}^{\infty} (-1)^n H_n(kr_s) e^{in\theta_s} (B_{-ns} \pm (-1)^n B_{ns}) (e^{-in\theta_s} \pm e^{in\theta_s}) \\ &\quad + (B_{0s} \pm B_{0s}) H_0(kr_s) \\ &= 4E_0 \sum_{n=1}^{\infty} (i)^n H_n(kr_s) \begin{Bmatrix} X_{ns} \cos n\theta_s \\ -iY_{ns} \sin n\theta_s \end{Bmatrix} + \begin{Bmatrix} 2E_0 X_{0s} H_0(kr_s) \\ 0 \end{Bmatrix} \end{aligned} \quad (\text{B.10})$$

APPENDIX C FIRST ORDER NEAREST NEIGHBOUR APPROXIMATION

For a low density of objects, the average separations will be large. Thus, any terms involving the object separation may be approximated by their large argument asymptotic expansion. In particular, the asymptotic expansion²⁷

$$H_n(z) \sim \sqrt{\frac{2}{\pi z}} e^{iz} (-i)^n e^{-i\frac{1}{4}\pi} \left\{ 1 + \frac{i(4n^2-1)}{8z} - \dots + \dots \right\} \quad (C.1)$$

may be utilized to calculate the coefficients

$$H_{mn}^+ = \left\{ H_{m-n}(kd) + (-1)^n H_{m+n}(kd) \right\} (i)^{n-m} f_{nm}^{st} \quad (C.2)$$

in equation (3.9) with the result that in equation (3.4)

$$H_{mns, s+1} \sim \frac{(1-i)e^{ikd}}{\sqrt{\pi}} \frac{1}{\sqrt{kd}} \left\{ \begin{array}{l} 1 \\ (-1)^{m+n} \end{array} \right\} \left\{ \begin{array}{l} -\frac{2imn}{kd} \\ 2 + \frac{i}{kd} (m^2 + n^2 - \frac{1}{4}) \end{array} \right\} \begin{array}{l} \perp \text{ pol.} \\ \parallel \text{ pol.} \end{array} \quad (C.3)$$

For large kd , the coefficients for the perpendicular polarization tend to zero faster than those for parallel polarization. Thus it is expected that most calculations will be more accurate for the perpendicularly polarized case.

As a large separation has been assumed, it is also reasonable to assume that multiple scattering effects are small and hence only one iteration is required to obtain convergence of equation (3.6). This means physically that the multiple scattered wave from the s^{th} cylinder is caused by the singly scattered waves from the $(s-1)^{\text{th}}$ and $(s+1)^{\text{th}}$ cylinder. That is,

$$Y_{mt} \approx -iA_m^{\perp} \frac{e^{ikL}}{\sqrt{kL}} U_t^{\frac{1}{2}} g^{\perp}(C_a Q_t) \sin m\beta_t \quad (C.4)$$

$$X_{mt} \approx A_m^{\parallel} \frac{e^{ikL}}{\sqrt{kL}} U_t^{\frac{1}{2}} g^{\parallel}(C_a Q_t) \cos m\beta_t$$

for $t = s+1$ only. Substitution of equations (C.3), (C.4), and (3.9) into equation (3.4) gives the N-N-1 approximation to the scattering coefficients:

$$Y_{ns} \approx -iA_{\perp} \frac{e^{ikL}}{n\sqrt{kL}} \left\{ U_{s,ns}^{\frac{1}{2}\perp} - \frac{1}{4}i\sqrt{2}C \frac{e^{ikd}}{(kd)^{\frac{3}{2}}} n \left[U_{s-1}^{\frac{1}{2}} \sum_{m=1}^N (-1)^{m+n} m A_{m,m,s-1}^{\perp} + U_{s+1}^{\frac{1}{2}} \sum_{m=1}^N m A_{m,m,s+1}^{\perp} \right] \right\} \quad (C.5)$$

$$X_{ns} \approx A_{\parallel} \frac{e^{ikL}}{n\sqrt{kL}} \left\{ U_{s,ns}^{\frac{1}{2}\parallel} + \frac{1}{4}\sqrt{2}C \frac{e^{ikd}}{(kd)^{\frac{3}{2}}} \left[U_{s-1}^{\frac{1}{2}} \sum_{m=0}^N (-1)^{m+n} A_{m,m,s-1}^{\parallel} + U_{s+1}^{\frac{1}{2}} \sum_{m=1}^N A_{m,m,s+1}^{\parallel} \right] \right\}$$

with

$$h_{ns}^{\perp,\parallel} = g_{\perp,\parallel}^{\perp,\parallel}(C_{\theta}/O_s) \begin{cases} \sin n\beta_s \\ \cos n\beta_s \end{cases} \quad (C.6)$$

Equation (C.5) for the parallel polarized field was derived under the additional assumption that the $(kd)^{-\frac{1}{2}}$ term sufficiently dominates the $(kd)^{-\frac{3}{2}}$ term in equation (C.3).

APPENDIX D SINGLE OBJECT SINGLE SCATTER STATISTICAL CALCULATIONS

This simplified method consists of using the statistics of a single object averaged over all possible positions to calculate the exact means and the approximate variances for the given ensemble of objects. Higher order moments may not be calculated with any accuracy at all. The potential saving here is very large, because the values calculated by the Monte-Carlo section of the analysis are independent of the density of the objects, thus eliminating one of the many variable parameters of the problem. For the single scatter uniform distribution,

$$E = 1 + \sum_{s=1}^{N_o} E_s(X_s) \quad (D.1)$$

Therefore,

$$\begin{aligned} \langle E \rangle &= \langle E_x \rangle + i \langle E_y \rangle \\ &= \left\langle 1 + \sum_{s=1}^{N_o} E_s \right\rangle \\ &= 1 + \left\langle \sum_{s=1}^{N_o} E_s \right\rangle \end{aligned} \quad (D.2)$$

But, as all the objects are identical and independent,

$$\begin{aligned} \left\langle \sum_s E_s \right\rangle &= \sum_s \langle E_o(X_o) \rangle \\ &= N_o \langle E_o \rangle \end{aligned} \quad (D.3)$$

Here, the subscript o means that any one of the N_o objects is to be used to calculate the average. Therefore

$$\begin{aligned} \langle E_x \rangle &= 1 + N_o \langle E_{x_o} \rangle \\ \langle E_y \rangle &= N_o \langle E_{y_o} \rangle \end{aligned} \quad (D.4)$$

To calculate the variance, an approximation must be made³².

$$\begin{aligned}
 \sigma_x^2 &= \langle E_x^2 \rangle - \langle E_x \rangle^2 \\
 &= \left\langle \left(1 + \sum_{s=1}^{N_0} E_{x_s} \right)^2 \right\rangle - \langle E_x \rangle^2 \\
 &= N_0 \langle E_{x_0}^2 \rangle - N_0^2 \langle E_{x_0} \rangle^2 + \sum_{s=1}^{N_0} \sum_{\substack{t=1 \\ s \neq t}}^{N_0} \langle E_{x_s} E_{x_t} \rangle
 \end{aligned} \tag{D.5}$$

It may be assumed that, for large numbers of objects in conjunction with a fairly low density, the last term of equation (D.5) may be neglected. If this is indeed possible, then (D.5) reduces to

$$\begin{aligned}
 \sigma_x^2 &\approx N_0 (\langle E_{x_0}^2 \rangle - N_0 \langle E_{x_0} \rangle^2) \\
 \text{Similarly,} \quad \sigma_y^2 &\approx N_0 (\langle E_{y_0}^2 \rangle - N_0 \langle E_{y_0} \rangle^2) \\
 \sigma_{xy} &\approx N_0 (\langle E_{x_0} E_{y_0} \rangle - N_0 \langle E_{x_0} \rangle \langle E_{y_0} \rangle)
 \end{aligned} \tag{D.6}$$

Now, from the area density function used in Chapter 4,

$$\begin{aligned}
 N_0 &= \rho \left\{ \left(\frac{C_a}{2ka} \right) kL \right\}^p \\
 &\cong \rho (C_0 kL)^p
 \end{aligned} \tag{D.7}$$

where

$$p = \begin{cases} 1 & \text{for hemicylinders} \\ 2 & \text{for hemispheres} \end{cases} \tag{D.8}$$

Therefore, the statistical functions become

$$\begin{aligned}
 \langle E_x \rangle &= 1 + \rho(c_o kL)^P \langle E_{x_o} \rangle \\
 \langle E_y \rangle &= \rho(c_o kL)^P \langle E_{y_o} \rangle \\
 \sigma_x^2 &\approx \rho(c_o kL)^P \left(\langle E_{x_o}^2 \rangle - \rho(c_o kL)^P \langle E_{x_o} \rangle^2 \right) \\
 \sigma_y^2 &\approx \rho(c_o kL)^P \left(\langle E_{y_o}^2 \rangle - \rho(c_o kL)^P \langle E_{y_o} \rangle^2 \right) \\
 \sigma_{xy} &\approx \rho(c_o kL)^P \left(\langle E_{x_o} E_{y_o} \rangle - \rho(c_o kL)^P \langle E_{x_o} \rangle \langle E_{y_o} \rangle \right)
 \end{aligned} \tag{D.9}$$

These functions are valid only for a uniform distribution with the single scatter approximation.

APPENDIX E INTEGRATION OF SINGLE SCATTER COHERENT AND INCOHERENT
INTENSITY FOR THE CONTINUOUS UNIFORM DISTRIBUTION

The comparison of the mean scattered field calculated by the Monte-Carlo method for the finite beamwidth problem and the Twersky infinite plane wave problem in Chapter 4 indicates that the differences are small, and hence amenable to approximation.

E.1 Two Dimensional Problem

E.1.1 Coherent Field

The average field scattered by a single object in the active scattering area is

$$\langle E_o \rangle = \frac{1}{W} \int_{-\frac{W}{2}}^{\frac{W}{2}} E(x) dx \quad (E.1)$$

let

$$\rho = \frac{x}{W} \quad (E.2)$$

be the continuous counterpart of the coordinate distribution ρ_s . Then

$$E_o = \int_{-0.5}^{0.5} E(\rho) d\rho \quad (E.3)$$

Therefore, using equation (3.21),

$$\langle E_o^{||, \perp} \rangle = \frac{4\sqrt{2}}{\pi} e^{-i\frac{1}{4}\pi} \sqrt{\frac{2\pi}{kL}} \int_{-0.5}^{0.5} e^{ikL(C_a \rho)^2} (1 - \frac{1}{2} C_a^2 \rho^2) g(C_a \rho) \sum_n (-1)^n A_n^{||, \perp} \begin{Bmatrix} \cos n\beta \\ 2 \\ \sin n\beta \end{Bmatrix} d\rho \quad (E.4)$$

The method of steepest descents³³ indicates that, provided $kL C_a^2$ is large, the major contribution to the integral occurs for ρ near zero. This fact means that β_s (from equation 2.5) may be approximated by $\frac{1}{2}\pi$. Hence,

$$\langle E_o^{||, \perp} \rangle \approx \sqrt{2} e^{-i\frac{1}{4}\pi\sqrt{\frac{2\pi}{kL}}} \left\{ \int_{-0.5}^{0.5} e^{i2kL C_a^2 \rho^2} (1 - \frac{1}{2} C_a^2 \rho^2) g^{||, \perp}(C_a \rho) d\rho \right\} \left\{ \frac{1}{4\pi} \sum_n A_n^{||, \perp} \right\} \quad (E.5)$$

$$= \sqrt{2} e^{-i\frac{1}{4}\pi\sqrt{\frac{2\pi}{kL}}} \int_{-0.5}^{0.5} e^{ikL C_a^2 \rho^2} (1 - \frac{1}{2} C_a^2 \rho^2) g^{||, \perp}(C_a \rho) d\rho$$

A very important point to note here is that it was necessary to assume the equivalent of $\beta_s = \frac{1}{2}\pi$ in the three dimensional case in order to obtain a useful solution. It was mentioned at that time that this would be valid only for a very narrow beam. However, it is indicated by equation (E.4) that only the product $\frac{L}{\lambda} C_a^2$ must be large. Thus, it will be reasonable to expect good results even for fairly wide beams provided that the antenna is a few hundred wavelengths away from the surface. This will certainly be the case in most physical situations.

To perform the integration of (E.4), let

$$t = -ikL C_a^2 \rho^2 \quad (E.6)$$

and, since ρ is small, expand the antenna space factor, g , in a Taylor series about $\rho = 0$. From equation (2.95)

$$g^{||}(u) \approx 1 - \frac{1}{6} \left(\frac{180}{\theta_e} \right)^2 u^2$$

$$g^{\perp}(u) \approx 1 - \left(\frac{270}{\theta_h} \right)^2 \left\{ \frac{1}{2} - \left(\frac{u}{\pi} \right)^2 \right\} u^2 \quad (E.7)$$

or more simply,

$$g^{||, \perp}(u) \approx 1 - b_{e,h} u^2 \quad (\text{E.8})$$

where

$$b_e = \frac{5400}{\theta_e^2} \quad (\text{E.9})$$

$$b_h = \frac{36450}{\theta_h^2} \left\{ 1 - \frac{8}{\pi^2} \right\}$$

Then, equation (E.5) becomes

$$\langle E_o^{||, \perp} \rangle \approx f_p \frac{2}{\sqrt{\pi}} (-2\pi i)^{\frac{1}{2}} \sqrt{\frac{2\pi}{kL}} \int_0^{\infty} e^{-t} \left\{ 1 - \left(\frac{1}{2} + b_{e,h} \right) C_a^2 \rho^2 \right\} d\rho \quad (\text{E.10})$$

Further, let

$$B = \frac{1 + 2b_{e,h}}{8} \quad (\text{E.11})$$

Thus,

$$\langle E_o^{||, \perp} \rangle \approx \frac{2\sqrt{\pi} f_p}{kLC_a} \left\{ \int_0^{\infty} t^{-\frac{1}{2}} e^{-t} dt + BC_a^2 \left[\frac{4}{ikLC_a^2} \right] \int_0^{\infty} t^{\frac{1}{2}} e^{-t} dt \right\} \quad (\text{E.12})$$

But

$$\int_0^z e^{-t} t^b dt \sim \Gamma(b+1) - z^b e^{-z} \quad (\text{E.13})$$

is the asymptotic expansion of the incomplete gamma function for large $|z|$ and $\arg(z) < 3\pi/2$.

Application of equation (E.13) to (E.12) yields the following expression

for the single object average:

$$\langle E_o \rangle \approx \frac{2\pi f_p}{kLC_a} \left[1 - \frac{2iB}{kL} - \frac{2}{C_a \sqrt{\pi kL}} (1 - BC_a^2) e^{i\frac{1}{4}\pi(1 + \frac{kLC_a^2}{\pi})} \right] \quad (E.14)$$

and hence the coherent field is given by, using equation (D.9),

$$\langle E \rangle = 1 + \frac{D\lambda f}{2a} \frac{1}{p} \left\{ 1 - 2 \left[\frac{iB}{kL} + \frac{1}{C_a \sqrt{\pi kL}} (1 - BC_a^2) e^{i\frac{1}{4}\pi(1 + \frac{kLC_a^2}{\pi})} \right] \right\} \quad (E.15)$$

E.1.2 Incoherent Intensity

For the second statistical moment of the scattered field, under the assumption of a continuous uniform distribution, the single object function is given by

$$\langle E_o^2 \rangle = \int_{-0.5}^{0.5} E(w\rho) E^*(w\rho) d\rho \quad (E.16)$$

Again, from equation (3.21) with $\beta_s = \frac{1}{2}\pi$,

$$\langle E_o^2 \rangle \approx \left| f_p \right|^2 \frac{4\pi}{kL} \int_{-0.5}^{0.5} \left(1 - \frac{1}{2} C_a^2 \rho^2 \right)^2 g(C_a \rho) d\rho$$

For the above integral, it is not sufficient to use the Taylor series expansion for $g(C_a \rho)$ because the method of steepest descents is not applicable. Therefore, the function g must be included in its entirety. Thus,

$$\langle E_o^2 \rangle \approx \left| f_p \right|^2 \frac{2\pi}{kL} \int_0^{\frac{1}{2}} \left(1 - C_a^2 \rho^2 \right) \frac{\sin^2(b C_a \rho)}{(b C_a \rho)^2} d\rho \quad (E.17)$$

$$\langle E_o^2 \rangle_{\perp} \approx \left| f_p \right|^2 \frac{28\pi}{kL} \int_0^{\frac{1}{2}} (1 - c_a^2 \rho^2) \frac{\cos^2(b^{\perp} c_a \rho)}{1 - \frac{4}{\pi^2} (b^{\perp} c_a \rho)^2} d\rho \quad (\text{E.18})$$

where

$$b^{\parallel} = \frac{180}{\theta_e} \quad (\text{E.19})$$

$$b^{\perp} = \frac{270}{\theta_h}$$

Let

$$t = \alpha \rho \quad (\text{E.20})$$

with

$$\alpha = b c_a \quad (\text{E.21})$$

Then,

$$\langle E_o^2 \rangle^{\parallel} = \frac{|f_p|^2 8\pi}{kL\alpha} \int_0^{\frac{1}{2}\alpha} \left(1 - \frac{t^2}{b^2}\right) \frac{\sin^2 t}{t^2} dt \quad (\text{E.22})$$

$$\langle E_o^2 \rangle_{\perp} = \frac{|f_p|^2 28\pi^2}{kL\alpha} \int_0^{\frac{1}{2}\alpha} \left(1 - \frac{t^2}{b^2}\right) \left[\frac{\sin(t+\frac{1}{2}\pi)}{t+\frac{1}{2}\pi} + \frac{\sin(t-\frac{1}{2}\pi)}{t-\frac{1}{2}\pi} \right]^2 dt \quad (\text{E.23})$$

Now let

$$I_1(\alpha) = \int_0^{\frac{1}{2}\alpha} \frac{\sin^2 t}{t^2} dt$$

$$I_2(\alpha) = \int_0^{\frac{1}{2}\alpha} \frac{\sin^2 t}{t} dt \quad (\text{E.24})$$

$$I_3(\alpha) = \int_0^{\frac{1}{2}\alpha} \sin^2 t dt$$

$$I_4(\alpha) = \int_0^{\frac{1}{2}\alpha} t \sin^2 t dt$$

Therefore,

$$\langle E_o^2 \rangle_{\parallel} = \frac{|f_p|^2 8\pi^2}{kL\alpha} \left[I_1(\alpha) - \frac{1}{b^2} I_3(\alpha) \right] \quad (\text{E.25})$$

For the perpendicularly polarized case, substitute

$$u = t \pm \frac{1}{2}\pi \quad (\text{E.26})$$

in the appropriate integrals to obtain after simplification

$$\begin{aligned} \langle E_o^2 \rangle_{\perp} = \frac{|f_p|^2 2\pi^2}{kL\alpha} & \left\{ \left[I_1(\alpha+\pi) + I_1(\alpha-\pi) \right] \left[1 - \frac{\pi^2}{4b^2} \right] + \left[I_2(\alpha+\pi) - I_2(\alpha-\pi) \right] \left[\frac{3\pi}{2b^2} - \frac{2}{\pi} \right] \right. \\ & \left. - \left[I_3(\alpha+\pi) + I_3(\alpha-\pi) \right] \left[\frac{3}{b^2} \right] + \left[I_4(\alpha+\pi) - I_4(\alpha-\pi) \right] \left[\frac{2}{\pi b^2} \right] \right\} \quad (\text{E.27}) \end{aligned}$$

Evaluate the integrals of equations (E.24):

$$\begin{aligned} I_1(\alpha) &= \int_0^{\frac{1}{2}\alpha} \frac{\sin^2 t}{t^2} dt \\ &= -\frac{2}{\alpha} \sin^2 \frac{\alpha}{2} + \int_0^{\frac{1}{2}\alpha} \frac{\sin t}{t} dt \\ &= -\frac{2}{\alpha} \sin^2 \frac{\alpha}{2} + \text{Si}\alpha \end{aligned} \quad (\text{E.28})$$

where $\text{Si}\alpha$ is the well known sine integral function²⁷.

$$\begin{aligned} I_2(\alpha) &= \int_0^{\frac{1}{2}\alpha} \frac{\sin^2 t}{t} dt \\ &= \frac{1}{2} \int_0^{\frac{1}{2}\alpha} \frac{\cos t - 1}{t} dt \\ &= \frac{1}{2} (\gamma + \ln \alpha - \text{Ci}\alpha) \end{aligned} \quad (\text{E.29})$$

Here, $\text{Ci}\alpha$ is the cosine integral function and γ is Euler's constant.

$$\begin{aligned}
 I_3(\alpha) &= \int_0^{\frac{1}{2}\alpha} \sin^2 t dt \\
 &= \frac{1}{4}(\alpha - \sin\alpha)
 \end{aligned}
 \tag{E.30}$$

Finally,

$$\begin{aligned}
 I_4(\alpha) &= \int_0^{\frac{1}{2}\alpha} t \sin^2 t dt \\
 &= \frac{1}{8} \left(\frac{\alpha^2}{2} - \alpha \sin\alpha + 1 - \cos\alpha \right)
 \end{aligned}
 \tag{E.31}$$

It is now possible to simplify (E.28) and (E.29) by using the asymptotic expansions for the sine and cosine integrals. This procedure is valid since $\alpha \ll 1$. In fact,

$$\begin{aligned}
 \alpha &= \frac{bc}{a} \\
 &= 2 \left\{ \begin{matrix} 180 \\ 270 \end{matrix} \right\} \left(\frac{1}{\theta_0} \right) K \tan \theta_0
 \end{aligned}
 \tag{E.32}$$

>10

even for θ_0 as small as 8° . Therefore²⁷,

$$\text{Si}(\alpha) \sim \frac{\pi}{2} - \frac{\cos\alpha}{\alpha} - \frac{\sin\alpha}{\alpha^2} \dots
 \tag{E.33}$$

$$\text{Ci}(\alpha) \sim \frac{\sin\alpha}{\alpha} - \frac{\cos\alpha}{\alpha^2} \dots$$

Thus, the single object incoherent intensity for the parallel polarization becomes

$$\langle E_o^2 \rangle \sim \frac{4\pi^2 |f_p|^2}{kLbC_a} \left\{ 1 - \frac{2}{\pi b C_a} \left[1 + \frac{C_a^2}{4} + \frac{1}{b C_a} \left(1 - \frac{C_a^2}{4} \right) \sin b C_a \right] \right\}
 \tag{E.34}$$

For the perpendicularly polarized case,

$$I_1(\alpha + \pi) + I_1(\alpha - \pi) \sim \pi + \frac{2}{\alpha} \cos \alpha + \frac{2}{\alpha^2} (\pi^2 \cos \alpha + \sin \alpha) \quad (\text{E. 35})$$

$$I_2(\alpha + \pi) - I_2(\alpha - \pi) = \text{ci}(\alpha + \pi) - \text{ci}(\alpha - \pi) + \ln \frac{\frac{\alpha}{\pi} + 1}{\frac{\alpha}{\pi} - 1} \quad (\text{E. 36})$$

but²⁷

$$\ln \frac{\frac{\alpha}{\pi} + 1}{\frac{\alpha}{\pi} - 1} \sim \frac{2\pi}{\alpha}, \quad \frac{\alpha}{\pi} \gg 1 \quad (\text{E. 37})$$

Therefore,

$$I_2(\alpha + \pi) - I_2(\alpha - \pi) \sim \frac{2\pi}{\alpha} \left[\frac{\sin \alpha}{\alpha} - 1 \right] \quad (\text{E. 38})$$

Without approximation,

$$I_3(\alpha + \pi) + I_3(\alpha - \pi) = \frac{1}{2} (\alpha + \sin \alpha) \quad (\text{E. 39})$$

and

$$I_4(\alpha + \pi) - I_4(\alpha - \pi) = \frac{\pi}{4} (\alpha + \sin \alpha) \quad (\text{E. 40})$$

so that the perpendicular component becomes

$$\langle E_o^{2\perp} \rangle \approx \frac{2\pi^3 |f_p|^2}{kLbC_a} \left\{ 1 - \frac{1}{\pi b C_a} \left[\frac{C_a}{b} \left(\frac{\pi^3}{4} + b C_a \right) - \frac{1}{b C_a} (4 - C_a^2) \sin b C_a \right] \right\} \quad (\text{E. 41})$$

Now, from equation (D.10),

$$\langle I^2 \rangle^{\perp} \approx \left(\frac{\Omega}{2a} \right) \frac{kLC_a}{2\pi} \left[\langle E_o^2 \rangle - \left(\frac{\Omega}{2a} \right) \frac{kLC_a}{2\pi} |\langle E_o \rangle|^2 \right] \quad (\text{E. 42})$$

If terms to the order of $\left(\frac{L}{\lambda}\right)^{-\frac{3}{2}}$ or less and $(bC_a)^{-2}$ or less are neglected, the approximate incoherent intensity is given by

$$\langle I^2 \rangle^{\parallel, \perp} \approx \left(\frac{\mathcal{O}\lambda}{2a} \right) |f_p|^2 \left\{ F^{\parallel, \perp} - \left(\frac{\mathcal{O}\lambda}{2a} \right) \left[1 + \frac{2(1-BC_a^2)}{C_a^2 \sqrt{\pi kL}} \cos \frac{1}{4} \pi \left(1 + \frac{kLC_a^2}{\pi} \right) + \frac{4(1-BC_a^2)}{\pi kLC_a^2} \right] \right\} \quad (\text{E.43})$$

where

$$F^{\parallel} = \frac{2\pi}{b} \left\{ 1 - \frac{2}{\pi b C_a} \right\} \quad (\text{E.44})$$

$$F^{\perp} = \frac{\pi^2}{b}$$

E.2 Three Dimensional Problem

E.2.1 Coherent Field

For a continuous uniform distribution on a plane,

$$\begin{aligned} \langle \dot{E}_o \rangle &= \frac{1}{A} \int_A E_o(x, y) dx dy \\ &= \frac{1}{\pi} \left(\frac{W}{2} \right)^2 \int_0^{2\pi \frac{1}{2} W} \int_0^{\frac{1}{2} W} E_o(R, \Phi) R dR d\Phi \\ &= \frac{4}{\pi} \int_0^{2\pi \frac{1}{2}} \int_0^{\frac{1}{2}} E_o(W\rho, \Phi) \rho d\rho d\Phi \end{aligned} \quad (\text{E.45})$$

Consider the angular integral first. Then, it can be immediately seen that the cross polarized components have the following form (see equation (2.133)) for $i \neq j$

$$\begin{aligned} \langle E_{ij} \rangle &= k \int_0^{2\pi} f(\Phi) \sin \Phi \cos \Phi d\Phi \\ &= 0 \end{aligned} \quad (\text{E.46})$$

since f is an even function of Φ . Note, as was mentioned in Chapter 2, the same reasoning may be applied to the z -axis component which has already been neglected. Thus, the cross polarized components are zero to the degree of approximation that has been used. Physically then, one would expect very little depolarization of the backscattered field at normal incidence for any surface which does not exhibit an appreciable amount of multiple scattering. That is, equation (E.17) will be zero for any physical distribution.

The direct components of the coherent field may now be calculated. Again, from equations (2.133),

$$E_{ii_0} = -\frac{ib}{kL} e^{ikLC_a^2 \rho^2} \left\{ \begin{array}{l} g(C_a \rho \sin \Phi, C_a \rho \cos \Phi) \\ g(C_a \rho \cos \Phi, C_a \rho \sin \Phi) \end{array} \right\} (1 - C_a^2 \rho^2) \left[1 - \frac{1}{2} C_a^2 \rho^2 \left\{ \begin{array}{l} \cos^2 \Phi \\ \sin^2 \Phi \end{array} \right\} \right] \quad (E.47)$$

As before, the antenna radiation pattern, g , may be expanded in a Taylor series about $\rho = 0$.

$$g(u, v) \approx 1 - (b_h u^2 + b_e v^2) \quad (E.48)$$

where b_e and b_h are given in equation (E.8). Substitute equations (E.22) and (E.23) into (E.20) and keep only terms to the order of ρ^2 .

$$\langle E_{ii_0} \rangle \approx -\frac{4ib}{\pi kL} \int_0^{\frac{1}{2}} \int_0^{2\pi} e^{ikLC_a^2 \rho^2} \left[1 - C_a^2 \rho^2 \left(1 + \left\{ \begin{array}{l} b_h \sin^2 \Phi + b_e \cos^2 \Phi + \frac{1}{2} \cos^2 \Phi \\ b_e \sin^2 \Phi + b_h \cos^2 \Phi + \frac{1}{2} \sin^2 \Phi \end{array} \right\} \right) \right] d\Phi \rho d\rho \quad (E.49)$$

Carry out the Φ -integration first. Then,

$$\langle E_{11} \rangle = \langle E_{22} \rangle \triangleq \langle E_o \rangle \quad (E.50)$$

and,

$$\langle E_o \rangle \approx -\frac{8ib}{kL} \int_0^{\frac{1}{2}} e^{ikLC_a \rho^2} (1 - BC_a^2 \rho^2) \rho d\rho \quad (E. 51)$$

with

$$B = \frac{2\frac{1}{2} + b_e + b_h}{2} \quad (E. 52)$$

Let

$$t = ikLC_a^2 \rho^2 \quad (E. 53)$$

Then,

$$\begin{aligned} \langle E_o \rangle &= -\left\{ \frac{2}{kLC_a} \right\}^2 b \int_0^{i\frac{1}{4}kLC_a^2} e^t \left(1 + \frac{iBt}{kL} \right) dt \\ &= -\left\{ \frac{2}{kLC_a} \right\}^2 b \left\{ \frac{iB}{kL} + e^{i\frac{1}{4}kLC_a^2} \left(1 - \frac{iB}{kL} - \frac{1}{4}BC_a^2 \right) \right\} \end{aligned} \quad (E. 54)$$

Therefore, the approximate coherent field is given by

$$\langle E \rangle \approx 1 - \rho \left(\frac{\lambda}{2a} \right)^2 \frac{b}{\pi^2} \left\{ \frac{iB}{kL} + e^{i\frac{1}{4}kLC_a^2} \left(1 - \frac{iB}{kL} - \frac{1}{4}BC_a^2 \right) \right\} \quad (E. 55)$$

In this (three dimensional) case, the expression for the average scattered field is not an asymptotic evaluation. In fact, it is to be expected that the results will be accurate only for small surface areas. This implies that (E.55) will only be valid if the product $(L)(C_a)$ remains sufficiently small. In fact, it can be seen that (E.55) becomes proportional to $e^{i\frac{1}{4}kLC_a^2}$ for large L . Clearly, this cannot be valid unless $C_a \rightarrow 0$ simultaneously to remove the indeterminate phase factor $e^{i\frac{1}{4}kLC_a^2}$.

E.2.2 Incoherent Intensity

From equations (2.133)

$$\langle E_d^2 \rangle = \frac{1}{4} \pi \left(\frac{b_0}{kL} \right)^2 \int_0^{2\pi} \int_0^{\frac{1}{2}} (1 - c_a^2 \rho^2)^2 \left[1 - \frac{1}{2} c_a^2 \left(\cos^2 \Phi + \sin^2 \Phi \right) \right] \left\{ \begin{array}{l} g^2(c_a \rho \cos \Phi, c_a \rho \sin \Phi) \\ g^2(c_a \rho \sin \Phi, c_a \rho \cos \Phi) \end{array} \right\} \rho d\rho d\Phi \quad (E.56)$$

Unfortunately, when the form of g has been substituted from equations (2.96), the integrations above become impossible to perform analytically. The problems arise because integrals of the form

$$\int_0^a \int_0^b \frac{\sin^m(a \sin \Phi) \cos^n(b \sin \Phi)}{P_1(a \sin \Phi) P_2(b \sin \Phi)} d\rho d\Phi \quad (E.57)$$

where P_1 and P_2 are polynomials and a and b are functions of ρ are encountered. Whichever integration is performed first is immaterial - the second integration becomes impossible because the asymptotic expansions of the sine and cosine integrals cannot be applied after the first integration alone.

Therefore, the incoherent intensity for the three dimensional case must be calculated by the Monte-Carlo technique in all cases involving the antenna model chosen for this study. An approximate expression could be derived by assuming a square beam (see equation (2.92)), but this is not considered here. The same reasoning is applicable to the cross-polarized components.

REFERENCES

1. Lord Rayleigh. Theory of Sound. Dover, New York, 1945.
2. Rice, S.O. "Reflection of Electromagnetic Waves from Slightly Rough Surfaces", The Theory of Electromagnetic Waves. Dover, New York, 1951.
3. Hoffman, W.C. "Scattering of E.M. Waves from a Random Surface", Quarterly of Applied Mathematics, 13, #3, 1955, p. 291
4. Silver, S. Microwave Antenna Theory and Design. Dover, New York, 1965
5. Peake, W.H. "Theory of Radar Return from Terrain", IRE National Convention Records, 7, Part I, 1959, p. 27.
6. Senior, T.B.A. "Impedance Boundary Conditions for Slightly Rough Surfaces", Applied Scientific Research B (Netherlands), 8, #5-6, 1960, p. 437.
7. Beckmann, P. The Scattering of Electromagnetic Waves from Rough Surfaces. Macmillan, New York, 1963.
8. Middleton, D. "A Statistical Theory of Reverberation and Similar First Order Scattered Fields", IRE Transactions on Information Theory, IT-13, #3, 1967, p. 372.
9. Bass, F.G. et al "Very High Frequency Radiowave Scattering By a Disturbed Sea Surface", IEEE Transactions on Antennas and Propagation, AP-16, #5, 1968, p. 554.
10. Ament, W.S. "Forward and Backscattering from Certain Rough Surfaces", IRE Transactions on Antennas and Propagation, AP-4, #4, 1956, p. 369.
11. Biot, M.A. "Some New Aspects on the Reflection of E.M. Waves on a Rough Surfaces", Journal of Applied Physics, 28, #12, 1957, p. 1455
12. Spetner, L.M. "A Statistical Model for Forward Scattering of Waves off a Rough Surface", IRE Transactions on Antennas and Propagation AP-6, #1, 1958, p. 88.
13. Twersky, V. "Multiple Scattering of Waves by Planar Random Distributions of Parallel Cylinders and Bosses", Research Report #EM-58, New York University Institute of Mathematical Sciences, 1953.
14. Twersky, V. "On the Nonspecular Reflection of Electromagnetic Waves", Journal of Applied Physics, 22, #6, 1951, p. 825.
15. Twersky, V. "On Scattering and Reflection of Sound by Rough Surfaces", Journal of the Acoustical Society of America, 29, #2, 1957, p. 209.

16. Twersky, V. "Scattering by Quasi-Periodic and Quasi-Random Distributions", IRE Transactions on Antennas and Propagation, AP-7, Special Supplement, 1959, p. s307.
17. Twersky, V. "Signals, Scatterers, and Statistics", IRE Transactions on Antennas and Propagation, AP-12, #3, 1964, p. 668.
18. Twersky, V. "Correlated Signals from Uncorrelated Distributions of Scatterers", Electromagnetic Wave Theory, J. Brown (Ed.), Pergamon Press, New York, 1967, p. 963.
19. Katzin, M. "On the Mechanisms of Radar Sea Clutter", Proceedings of the IRE, 45, #1, 1957, p. 44.
20. Clarke, R.H. and G.O. Hendry. "Prediction and Measurement of the Coherent and Incoherent Power Reflected from a Rough Surface", IRE Transactions on Antennas and Propagation, AP-12, #3, 1964, p. 353.
21. Hiatt, R.E., T.B.A. Seniour, and V.H. Weston. "A Study of Surface Roughness and its Effect on the Backscattering Cross Section of Spheres", Proceedings of the IRE, 48, #12, 1960, p. 2008.
22. Parkins, B.E., "The Omnidirectional Scattering of Acoustic Waves From Rough Surfaces with Application to Electromagnetic Scattering", CRES Report # 48-4.
23. Hammerskey, J.M., and D.C. Handscomb. Monte-Carlo Methods, Methuen & Co. Ltd. London, 1964.
24. Jones, D.S. The Theory of Electromagnetism, Macmillan, New York, 1964.
25. Stratton, J. A. Electromagnetic Theory, McGraw Hill, New York, 1941.
26. Morse, P.M. and H. Feshback. Methods of Theoretical Physics, McGraw Hill, New York, 1953.
27. Abramowitz, M. and I.A. Stegun. Handbook of Mathematical Functions, Dover, New York, 1965.
28. Erdelyi, A. et al. Higher Transcendental Functions, McGraw Hill, 1953.
29. Twersky, V. "Multiple Scattering of Radiation by an Arbitrary Configuration of Parallel Cylinders", Journal of the Acoustical Society of America, 24, 1952, p. 42.
30. Faddeeva, V.N. Computational Methods of Linear Algebra, Dover, New York, 1959.
31. Ralston, A. A First Course in Numerical Analysis, McGraw Hill, New York, 1965.
32. Olsen, R.L. "A Study of the Scattering of Electromagnetic Waves from Certain Types of Random Media", Ph.D. Thesis, University of British Columbia, 1970.

33. Van de Hulst, H.C. Light Scattering by Small Particles, Wiley, New York, 1965.
34. Mathew, J. and R.L. Walker. Mathematical Methods of Physics, Benjamin, New York, 1965.
35. Fortuin, L. "Survey of Literature on Reflection and Scattering of Sound Waves at the Sea Surface", Journal of the Acoustical Society of America, May 1970.